# Vibration-Based Damage Detection Using Machine Learning Techniques with Application to Offshore Wind Turbines

By

YULONG ZHANG


Department of Civil Engineering
UNIVERSITY OF BRISTOL

A dissertation submitted to the University of Bristol in accordance with the requirements for award of the degree of
DOCTOR OF PHILOSOPHY
in the Faculty of Engineering.

SEPTEMBER 2021

*This page intentionally left blank*.

# Abstract

Although vibration-based damage detection (VBDD) has seen great advancements since the 1980s, it is still facing several challenges, such as identifying features of vibration measurements that are sensitive to damage, tackling nonlinear structures, and removing environmental and operational variation (EOV) effects. This thesis is devoted to addressing these challenges, with application to offshore wind turbines (OWTs) for which there is demand for VBDD techniques for cost reduction.

A new VBDD method is proposed for linear structures subject to Gaussian white noise loading. It characterises vibration responses with the multivariate probability density function (PDF) of the underlying stochastic process. The change of the PDF, measured by the Kullback-Leibler divergence, is defined as a damage index. From a case study of an OWT with a reduction to the foundation stiffness, it is shown that the proposed method offers significant performance improvements over an autoregressive-based method and an autocorrelation function-based method.

For structures that are nonlinear both before and after damage, the PDFs become non-Gaussian and difficult to estimate. Therefore, the density ratio estimation method, which directly estimates the difference of the PDFs rather than the individual PDFs themselves, is applied to data from the undamaged state and a potentially damaged state. The effectiveness and advantages of the proposed method are demonstrated in two case studies: an experimental nonlinear beam and an OWT with nonlinear pile-soil interaction.

To remove EOV effects, a new approach is proposed and applied to OWTs. It takes advantage of the fact that OWTs are built in groups and thus are subjected to similar EOVs at the same time. When the monitored features are viewed relative to each other, the complex EOV effects are probably cancelled. The method is demonstrated on a wind farm with three OWTs affected by scouring damage, and the results show that the damage is detected and localised to a specific OWT.

*This page intentionally left blank*.

# Dedication and acknowledgements

I would like to express my sincere gratitude to my supervisors, whose continuous support, consideration and encouragement have made this an enjoyable experience for me. I am extremely grateful to Professor John Macdonald for his consistent guidance that has steered me throughout the research, and insightful thoughts that have inspired me to think more deeply and stimulated my passion for research. I would also like to extend my thanks to Dr. Paul Harper, who has continuously provided encouragement and was always willing and enthusiastic to help. I am also grateful to Dr. Song Liu, from the School of Mathematics, who gave me tremendous support and valuable suggestions on machine learning techniques.

I would like to thank my Annual Progress Reviewer, Dr. Nicholas Alexander, for his supportive and cheerful conversations. I would like to thank DNV for providing access to Bladed, and Dr. Armando Alexandre of DNV for his valuable input on wind turbine modelling. I am also thankful to the School of Engineering and all its staff for all the considerate guidance.

During my PhD, I have met so many great friends: Gang, Xiaofang, Jiteng, Gongyu, Bob, Zeo, Xiaoyang, Yanan, Edward, Abhishek, Eva, Anderson and others, who have made my life both in and out of office full of happiness.

Special thanks to my wife, Jing.

*Dedicated to my parents and my wife.*

*This page intentionally left blank*.

# List of publications

This thesis is based on the work listed below:

**Journal papers:**

1. **Zhang Y.**, Macdonald J., Liu S., Harper P. (in press). Damage detection of nonlinear structures using probability density ratio estimation. *Computer-Aided Civil and Infrastructure Engineering*.

2. **Zhang Y.**, Macdonald J., Liu S., Harper P. Structural damage detection by comparing multivariate probability density functions of vibration data. Manuscript submitted for publication.

3. **Zhang Y.**, Macdonald J., Liu S., Harper P. Vibration-based damage detection of offshore wind turbine foundations under environmental and operational variations. Manuscript in preparation.

**Conference papers:**

1. **Zhang Y.**, Macdonald J., Liu S., Harper P. (2021, May 25-28). *Vibration-based damage detection of an offshore wind turbine foundation - a new approach to remove environmental and operational effects*. 3rd Wind Energy Science Conference, Hannover, Germany.

2. **Zhang Y.**,Macdonald J., Harper P., Liu S. (2020). Vibration-based damage localization using the density ratio estimation method. In M. Papadrakakis, M. Fragiadakis, C. Papadimitriou (Eds.), *Proceedings of EURODYN 2020 XI International Conference on Structural Dynamics*, Volume I (pp. 823-832).

Journal Paper 1 and 3 are modified and extended from Conference paper 2 and 1, respectively. Chapter 3, 4, and 5 in this thesis are built on Journal Paper 2, 1, and 3, respectively.

*This page intentionally left blank*.

# Author's declaration

I declare that the work in this dissertation was carried out in accordance with the requirements of the University's *Regulations and Code of Practice for Research Degree Programmes* and that it has not been submitted for any other academic award. Except where indicated by specific reference in the text, the work is the candidate's own work. Work done in collaboration with, or with the assistance of, others, is indicated as such. Any views expressed in the dissertation are those of the author.

SIGNED: YULONG ZHANG DATE:17/09/2021

*This page intentionally left blank*.

# Table of Contents

*This page intentionally left blank*.

# List of Tables

**TABLE** **Page**

*This page intentionally left blank*.

# List of Figures

**FIGURE** **Page**

# Acronyms

**ACF** Autocorrelation function.

**AIC** Akaike Information Criterion.

**ANN** Artificial neural network.

**AR** Autoregressive.

**DI** Damage index.

**DRE** Density ratio estimation.

**EOV** Environmental and operational variation.

**KL** Kullback-Leibler.

**KLIEP** Kullback-Leibler importance estimation procedure.

**LCL** Lower control limit.

**OMA** Operational modal analysis.

**OWT** Offshore wind turbine.

**PCA** Principal component analysis.

**PDF** Probability density function.

**PSD** Power spectral density.

**ROC** Receiver operating characteristics.

**ROC-AUC** Area under the ROC curve.

**SHM** Structural health monitoring.

**SVM** support vector machine.

**UCL** Upper control limit.

**VBDD** Vibration-based damage detection.

*This page intentionally left blank*.

CHAPTER 1

# Introduction

## 1.1 Motivation

Civil structures such as buildings, bridges and railways provide fundamental services to modern societies. The reliable and efficient functioning of these structures is critical to promoting economic growth and supporting social development. Due to harsh environmental and operational conditions, however, deterioration of these structures is inevitable. The deterioration is a serious concern because it decreases the lifespan and reliability of the systems, resulting in unexpected life and economic losses. Therefore, it is critical to make management decisions about maintenance, replacement or repairs, as well as identifying failures. This has motivated the research of structural health monitoring (SHM), which attempts to detect, identify, and assess damage in structural systems.

Current approaches for health monitoring of civil structures are mainly based on periodically visual inspections or non-destructive evaluation methods (e.g., acoustic and ultrasonic techniques) (Farrar and Worden, 2012). The non-destructive evaluation methods focus on specific structural components, and thus are called local methods. Yet, they have several drawbacks when applyed to large civil structures such as bridges, buildings and offshore wind turbines (OWTs) (Avci et al., 2021). Primarily, due to the large size of these structures, the monitoring is both laborious and time-consuming. In addition, it is very likely that the critical structural members are not accessible. For example, buildings are covered by non-structural architectural material, and offshore structure foundations are under water.

Because of the limitations of the local methods, the global methods that attempt to simultaneously detect damage throughout the whole structure has gained widespread interest. These methods examine changes in the structural vibration characteristics extracted from vibration responses, and thus are also called vibration-based SHM. The dependence on vibration signals brings these methods extra advantages such as the

ability to be automated, and mature and reasonably low-cost signal measurement and acquisition technologies (Fassois and Sakellariou, 2007).

An SHM problem consists of different levels of tasks. Based on the four levels suggested by Rytter (1993), Farrar et al. (1999) added a level of classification and proposed five levels of tasks: (i) *damage detection* - to indicate the occurrence of damage; (ii) *damage localisation* - to identify the location of damage; (iii) *damage classification* - to identify the type of damage; (iv) *damage assessment* - to assess the severity of damage; (v) *damage prognosis* - to predict the remaining life of the structure. The first level sub-problem, damage detection, is the foundation of other levels of tasks and thus has received the most attention. When using vibration-based SHM, it is referred to as vibration-based damage detection (VBDD), which is the focus of this thesis.

Over the past three decades, there has been a rapid development in the field of VBDD, ranging from mechanical, aerospace and civil structures. Particularly, VBDD on rotating machinery, also referred to as condition monitoring, has matured and been widely used in actual practice (Farrar and Worden, 2012). In contrast, the studies on aerospace and civil structures are still limited to highly controlled situations such as laboratory conditions and numerical simulations. This is mainly due to environmental and operational variations (Farrar and Worden, 2012; Brownjohn et al., 2011), which can significantly alter the dynamic responses and often mask subtle changes in the vibration signals caused by damage. Therefore, separating changes in the measured vibration caused by damage from those caused by environmental and operational variations is critical for real-world applications of SHM. Apart from that, other challenges also exist, such as identifying features of vibration measurements that are sensitive to damage, and detecting damage of nonlinear structures (Yan et al., 2007; Hou and Xia, 2021; Avci et al., 2021).

Among various civil structures, OWTs are experiencing rapid development worldwide. However, the cost of offshore wind energy generation is in general higher compared to fossil-fuel-based energy sources. For the wind industry to survive in competition with conventional energy resources, it is crucial that the costs are significantly reduced for future projects. Due to the long offshore distance and the harsh ocean environment, one main part of the costs is from the maintenance and operation. To reduce it, SHM techniques can be applied to detect damages for OWTs in the early stage and thus contribute towards optimising maintenance scheduling and eliminating unexpected catastrophic failures. In addition, considering typical OWTs have a 20-year design lifetime, the first generation of OWTs have approached the end of their design life.

Applying SHM techniques to these OWTs becomes even more important and may help to extend the expected lifetime. Various studies on VBDD for OWTs have been conducted in the last decade. They have focused on gearbox faults (Wang et al., 2019; Salameh et al., 2018) and blade damage (Du et al., 2020; Stetco et al., 2019). However, the studies on VBDD for foundations of OWTs are still limited. Hence this thesis concentrates on applying VBDD to OWT foundations, which can also experience a variety of failure modes and are vital in ensuring the safe operation of the turbines.

## 1.2 Research objectives

This work aims to address some of the existing challenges of VBDD, especially for application on OWT foundations. Based on the challenges discussed above, and more details in Section 2.3, the following research objectives are identified:

(1). *To explore new features of vibration response data that can improve the detection of damage.*

In this thesis, a feature is defined as a quantity extracted from vibration response data and then used to indicate the presence of damage. Despite the vast number of existing VBDD features, new features are still desirable to improve the performance of existing damage detection tasks and tackle new damage scenarios. This will be addressed in Chapter 3.

(2). *To improve damage detection of initially nonlinear structures.*

Initially nonlinear structures refer to structures that are nonlinear both before and after damage. For example, an OWT is an initially nonlinear structure when considering the nonlinear soil-pile interaction of foundations and scour damage. Most existing VBDD methods assume that the structure behaves linearly before and after damage, or that the system is linear in the undamaged state and becomes nonlinear in the damaged state. However, VBDD for initially nonlinear structures has rarely been studied. Chapter 4 will tackle this point.

(3). *To develop VBDD technique that can remove the effects of environmental and operational variations.*

Environmental and operational variations can significantly alter the dynamic response features and often mask subtle changes in the vibration signals caused by damage. Therefore, separating changes in features caused by damage from those

caused by environmental and operational variations are critical for real-world applications of VBDD. This applies especially to OWTs, which are subjected to a variety of environmental and operational variations, including wind conditions, sea states, temperature, humidity, operational states, rotational speeds, yaw angles, and so forth. This issue will be addressed in Chapter 5.

## 1.3 Structure of the thesis

This thesis consists of six chapters. In the remaining chapters, Chapter 2 presents the literature review, followed by three chapters (Chapter 3, Chapter 4, and Chapter 5) adapted from three journal paper manuscripts. The last chapter, Chapter 6, draws the entire body of research together to provide conclusions and areas of future work. The contents of these chapters and the links between them are summarised below.

- **Chapter 2**

  This chapter presents a literature review of VBDD and it applications on OWTs. The VBDD techniques are categorised by the features and classifiers used. The advantages and disadvantages of different methods are discussed. After briefly introducing OWT foundations, the applications of VBDD techniques to OWTs are reviewed according to different components, with special focus on OWT foundations.

- **Chapter 3**

  This chapter addresses the first challenge in Section 1.2 by presenting a new feature for VBDD: the multivariate probability density function (PDF) of the stochastic process of vibration responses from a single sensor on a structure. The change between the PDF of the undamaged state and that of a potentially damaged state, measured by the Kullback–Leibler divergence, is defined as a damage index. This study focuses on VBDD for a linear system under excitation and noise; both assumed to be Gaussian white noise. The effectiveness and advantages of the proposed method are demonstrated in a case study of a simplified OWT. The results show the proposed method provides significant performance improvements over an autoregressive-based method and an autocorrelation function-based method, especially when the noise level is high. Although this chapter applies the idea of the multivariate PDF feature in a simplified way (the vibration signals have Gaussian PDFs due to the system is linear and the input is Gaussian white noise),

it paves the way to the next chapter, where a more sophisticated statistical method is investigated for nonlinear systems.

- **Chapter 4**

  The second challenge in Section 1.2 is tackled in this chapter.

  Chapter 3 studies a linear structure under Gaussian white noise loading. This allows the vibration signals to be characterised by Gaussian PDFs and the damage index has a closed-form expression. However, structures may be nonlinear, resulting in non-Gaussian PDFs of the vibration responses. For damage detection, the PDFs have to be estimated, which is known to be a difficult problem. This issue becomes more challenging when considering the structure is nonlinear both before and after damage. To overcome this, the method developed in Chapter 3 is extended by introducing density ratio estimation for damage index calculation.

  This study focuses on VBDD for a structure that has nonlinear behaviour even in the undamaged state. Based on the vibration responses of a single sensor, a non-Gaussian multivariate PDF is developed and used as a feature. The change between the PDF of the undamaged state and that of a potentially damaged state is used to indicate the damage. Since what is of interest is the change of the PDF, instead of estimating the two PDFs separately, the ratio of them is estimated directly using a density ratio estimation method. In addition, principal component analysis is applied to reduce the dimensionality of the PDFs. The effectiveness and advantages of the proposed method are demonstrated in two case studies: an experimental nonlinear beam and simulations of an OWT subjected to nonlinear pile-soil interaction. Compared with the method in Chapter 3, the proposed method shows better damage detection performance due to the integration of higher-order statistical information.

- **Chapter 5** In this chapter, the third challenge in Section 1.2 is addressed.

  In Chapter 3 and Chapter 4, the EOVs were assumed to be similar in the undamaged state and potentially damaged states. Hence, the EOV effects can be simply removed by comparing the features of different states in the similar EOVs. This approach requires the measurement of EOVs, which may be impossible due to the high costs of measurement activities. Therefore, it is desirable to remove the EOV effects without relying on EOV records.

This chapter proposes a new approach to remove the effects of EOVs for OWTs. It takes advantage of the fact that OWTs are built in groups and thus subjected to similar EOVs at the same time. When the monitored features are viewed relative to each other, the complex EOV effects are probably cancelled out. Specifically, the relationships between the features of adjacent OWTs are modelled using Gaussian process regression. The learnt regression models are then used for predictive purposes, and the residuals between the actual features and predicted features are monitored in a control chart for damage detection. The method is demonstrated on a wind farm with three OWTs affected by scour damage, and the results show that it can detect the damage and localise the damage to a specific OWT.

- **Chapter 6**

  This final chapter summarises the work performed on developing damage features, detecting damage for initially nonlinear structures and removing EOV effects when identifying damage. Conclusions are provided concerning the novelty and value of the research conducted in relation to the main objectives. Limitations of the research and important areas of future work are also discussed.

## 1.4 Summary

In this chapter, the backgrounds of VBDD and OWTs have been briefly introduced to justify the main research objectives of the thesis. It was highlighted that although VBDD has become a widespread damage detection technique, it currently faces significant challenges. This thesis aims to address three of them: identifying features of vibration measurements that are sensitive to damage, detecting damage of nonlinear structures, and removing environmental and operational variation effects. The structure of the thesis has also been outlined, with an explanation of the links and dependencies between each chapter. The following chapter will address the literature review on VBDD and its applications to OWTs.

CHAPTER 2

# Literature Review

In Chapter 1, it has been pointed out that this thesis concerns the challenges of VBDD and its application to OWT foundations. Accordingly, the literature review in this chapter is presented in two main parts: a review on VBDD in Section 2.1 and a review on applications to OWTs in Section 2.2. This chapter closes with Section 2.3, where the objectives outlined in Section 1.2 are explained and justified in greater detail.

## 2.1 Vibration-based damage detection

VBDD is an SHM task that relies on vibration responses and addresses the damage detection problem (i.e., to indicate the occurrence of damage), as described in Section 1.1. Over the past few decades, various studies on VBDD have been conducted. Yet, all these studies can be described by a unifying paradigm (Farrar et al., 2001), which consists of the following four steps:

(i). *Operational evaluation*. This step answers questions such as: (1) is it economically justified to perform VBDD on the structure ? (2) what is the damage to be detected ? (3) how are the effects of environmental and operational variations of the structure ?

(ii). *Data acquisition*. This step should determine the data to be acquired from the structure, including sensor types and locations and the corresponding data acquisition/storage/transmittal hardware.

(iii). *Feature extraction*. In this step, a quantity, referred to as a feature, is extracted from the measured data to indicate damage.

(iv). *Feature discrimination (one-class classification)*. Using the extracted features, a statistical model is trained to discriminate the features from the undamaged state and damaged states.

This thesis focuses on feature extraction and feature discrimination.

In the rest of this section, a brief overview of VBDD is presented in Section 2.2.1, followed by a review on feature extraction and a review on feature discrimination (one-class classification) in Section 2.1.1 and Section 2.1.2, respectively. In Section 2.1.3, key challenges linked to further development of VBDD are discussed.

### 2.1.1 Features

For VBDD, a feature is as a quantity extracted from vibration response data and then used to indicate the presence of damage. The ideal features should be sensitive to damage but insensitive to operational and environmental variations.

There has been a large number of features in the literature, and the number is still increasing. According to the principles for the modelling of the vibration response, the features fall into different categories. A distinct category is the so-called physics-based approach, which relies on a model developed from first physical principles; this is typically a finite element model, corresponding to the finite element model updating method (Friswell and Mottershead, 1995). In contrast, the other modelling methods are termed data-driven methods, including classical modal parameter-based methods, time series methods, signal processing methods, machine learning-based methods and others (Hou and Xia, 2021). Among these data-driven methods, modal-parameter based methods are more related to the principle of structural dynamics, while time-series models originate from econometrics, signal processing is an electrical engineering subfield, and machine learning-based methods are from computer science.

Although the methods for feature extraction varies, they all attempt to reconstruct the vibration responses; then, the model coefficients or residuals are used as features. These features are reviewed in the following.

#### 2.1.1.1 Finite element model updating methods

In finite element model updating methods, the vibration response is reconstructed through a finite element model. The model parameters, such as mass, stiffness and damping matrices, are normally used as features. These model parameters are updated to fit the measurement data as closely as possible (Friswell and Mottershead, 1995). Changes in these model parameters can be used to detect, localise and quantify the damage. The measurement data can be the vibration response such as accelerations (Li et al., 2012) and dynamic strains (Li et al., 2015b) directly, but more often, they are the

modal parameters such as frequencies and mode shapes (Yu et al., 2016; Aoyama and Yagawa, 2001; Papadimitriou and Papadioti, 2013).

However, the measurement data usually have significant uncertainties, mainly due to environmental and operational variations and measurement noise. Through the finite element model, these uncertainties propagate to the model parameters. To account for the uncertainties in the model parameters, the Bayesian framework is introduced to model updating by Beck and Katafygiotis (1998) and Sohn and Law (1997), yielding the obtained model parameters in the form of probability distributions rather than deterministic values. One challenge of applying the Bayesian framework is calculating marginal posterior probability distributions, especially for systems with multiple updating parameters (Behmanesh and Moaveni, 2015). A naive way to deal with this is using the maximum a posterior probability estimate of the parameters (Lam et al., 2014; Behmanesh et al., 2017). Though computational efficient, this method losses the parameter distribution information. Another common approach is numerical-based; it generates the samples of the posterior distributions of the model parameters using Markov chain Monte Carlo and then estimates the posterior distributions based on these generated samples (Beck and Au, 2002; Ching et al., 2006; Nguyen and Goulet, 2019).

Finite element model updating methods have been applied to several real-world structures (Teughels and De Roeck, 2004; Reynders et al., 2010; Behmanesh and Moaveni, 2015). However, most of these methods are inherently assuming the structure is linear and time-invariant, making them inapplicable for structures with nonlinear or non-stationary response (Farrar and Worden, 2012).

#### 2.1.1.2 Modal parameters

Modal parameters are the most common and historically important class of features. This may be because most researchers for VBDD are familiar with structural dynamics, making modal parameters become their first choice for features. These features consist of basic modal properties (e.g., modal frequencies (Radzieński et al., 2011), modal damping (Mustafa et al., 2018), and mode shapes (Yoon et al., 2010)) and their derivations (e.g., operating deflection shape (Zhang et al., 2013), modal strain energy (Meruane and Heylen, 2011)). Good review papers are provided by Doebling et al. (1996, 1998).

Although using modal parameters as features is intuitive, its actual application is still challenging. Structural damage typically is a local phenomenon and is characterised by local vibration response. Because the local response is captured by higher modes, whereas the global response is captured by lower modes, it is desirable to use the higher

modes as features as they are more sensitive to damage. However, the higher modes are normally difficult to excite by ambient loading. Even in some cases, it is possible to apply experimental excitation; exciting higher modes requires more energy to produce a measurable response. In addition, frequencies are insensitive to damage (Farrar and Worden, 2012). For example, Farrar et al. (1994) reduced the cross-sectional stiffness at the centre of a main plate girder by 96.4%, resulting in a stiffness reduction of 21% for the overall bridge cross-section, the shifts in the modal frequencies were still not significant.

#### 2.1.1.3 Time-series methods

Time series models fit time series of vibration response with statistical tools, accounting for the internal structure of the time series, such as trend, seasonal variation and autocorrelation. The model coefficients or the residual errors are usually used as features (Fassois and Sakellariou, 2007). Common and basic models include autoregressive model (AR) (Fugate et al., 2001; Gul and Catbas, 2009; Yao and Pakzad, 2012), autoregressive with exogenous input model (Sohn and Farrar, 2001; Gul and Catbas, 2011; Lu and Gao, 2005) and autoregressive with moving average model (Nair et al., 2006; Omenzetter and Brownjohn, 2006; Carden and Brownjohn, 2008).

To tackle more complex scenarios, these basic models have been developed into more advanced models by replacing the model coefficients with various functions. For non-stationary time series, coefficients are replaced with various functions of time (Poulimenos and Fassois, 2006; Spiridonakos and Fassois, 2014). Similarly, uncertainties from environmental and operational variations are addressed by introducing mixture models to the coefficient functions (Avendaño-Valencia and Fassois, 2017a,b; Avendaño-Valencia et al., 2020).

#### 2.1.1.4 Signal processing methods

A fundamental signal processing method is the fast Fourier transform. However, it is not suitable for non-stationary signals (Peng and Chu, 2004). To overcome this, time-frequency methods such as short-time Fourier transform have been proposed. Compared with fast Fourier transform, short-time Fourier transform focuses on a local region of signals by applying a window function; thus, it can provide both frequency and time information of the signals. Unfortunately, short-time Fourier transform uses the same window for the entire signals, leading to a fixed time resolution and thus a fixed frequency resolution. To change the window size adaptively, the wavelet transform can be

applied (Yang and Nagarajaiah, 2014; Taha et al., 2006; Ulriksen et al., 2016). Another signal processing method is the Hilbert–Huang transform (Chen et al., 2007; Bao et al., 2013b), which decomposes a signal through the empirical mode decomposition process. To tackle the mode mixing problem in empirical mode decomposition, the ensemble empirical mode decomposition method has been applied (Aied et al., 2016). In addition, fractal dimension is also used (Amezquita-Sanchez and Adeli, 2015b; Li et al., 2011a).

#### 2.1.1.5 Machine learning-based methods

Machine learning techniques are essentially optimisation problems, aiming to satisfy explicitly defined objective functions using data. All the machine learning methods used for feature extraction are regression models. And again, the model coefficients or residuals are applied as features. Seemingly, there has been a large number of machine learning methods applied in VBDD. These methods are mainly based on two fundamental models: artificial neural network (ANN) and principal component analysis (PCA). It is worth noting that support vector machine, which is also widely seen in VBDD, is viewed as a method for classifying features instead of extracting features; hence it is discussed subsequently in Section 2.1.2.2.

ANN can be viewed as a universal function that can approximate arbitrary relationships between inputs and outputs. It has been applied for damage detection since the 1990s (Kudva et al., 1992; Wu et al., 1992). After that, more advanced ANN models have also been used, such as multilayer ANN (Yuen and Lam, 2006) and ensemble of ANNs (Hakim et al., 2015). However, these conventional ANN methods rely on shallow nets and have limited modelling power. Due to the improvements in computational power, deep neural networks, with more layers, have been developed. One of the biggest advantages of these deep neural network methods is that they can extract optimised features automatically for the problems at hand (Yu et al., 2019; Lin et al., 2017); this makes them attractive for VBDD. But they are black-box models and thus lack interpretability.

PCA is generally known as a dimensionality reduction technique, and it is very common to see it being used for this purpose, such as in Worden et al. (2000) where the dimensionality of the frequency response function data is reduced. More examples can be found in Dackermann et al. (2013) and Bandara et al. (2014). In addition, it is also often to view PCA as a decomposition of the original signals (Bishop, 2006). In these cases, the model residuals of PCA can be applied as features (Yan et al., 2005a,b; Li et al., 2011b). All the studies above employ PCA to variables (i.e., frequency response function data and natural frequencies) extracted from the vibration responses. Apart from that,

PCA has been applied to the vibration response directly. For example, in Mújica et al. (2011), Mújica et al. (2013) and Ruiz et al. (2013), PCA is applied to a matrix consisting of measurements from repeated experiments. Although the conventional linear PCA is widely used, due to the complex nonlinearity of some vibration responses, nonlinear PCA may be more suitable, such as adaptive PCA (Jin et al., 2015), local PCA (Yan et al., 2005b), and kernel PCA (Lim et al., 2011).

### 2.1.2 One-class classification

The previous section has elaborated on different classes of features. Given these features, the next task is discriminating the features from the undamaged state and those form damaged states.

For VBDD, it is common that a large number of data in the undamaged state is available, whereas there are insufficient or even no data for damaged states. For example, vibration responses of a bridge in its undamaged state can be measured on a daily basis, but it is almost impossible to obtain the data in a damaged state. This scenario makes the feature discrimination in VBDD to be a typical novelty detection problem, which identifies the newly observed data that differ from the data that is readily available. Alternative terms for novelty detection are anomaly detection and outlier detection. The different terms is a result of different application domains, and there is no universally accepted definition (Pimentel et al., 2014). Essentially, novelty detection is a one-class classification task in which the class for the undamaged state is separated from all damaged states. Compared with novelty detection, one-class classification is a more generalised term and retains the link to multi-class classification which can be used for higher-level SHM problems such as damage localisation and classification. Hence, this thesis adopts the term of one-class classification instead of feature discrimination or novelty detection.

From a methodological viewpoint, one-class classification methods fall into two categories (Tax, 2001; Mazhelis, 2006): density-based methods and boundary-based methods.

#### 2.1.2.1 Density-based methods

The basic idea of the density-based methods is that the features, such as resonant frequencies, for the undamaged state follow a PDF, and a new observed feature with a low probability is believed to be from a different state (i.e., damaged state) (Worden et al., 2003; Farrar and Worden, 2012). There are two major steps of the method: first,

estimating the PDF; then, determining the threshold, out of which the probability is viewed as low. In this section, the methods for PDF estimating are reviewed, followed by a discussion on the selection of the threshold.

PDF estimation methods generally fall into two categories: parametric methods and non-parametric methods (Wasserman, 2013). A parametric method relies on a pre-specified form of the PDF and can be parameterised by a finite number of parameters; hence it is 'parametric'. For example, a Gaussian distribution model has two parameters, mean and standard deviation. On the other hand, a non-parametric model cannot be parameterised by a finite number of parameters.

When the PDF form is known or assumed, it is easy to estimate the parameters of the PDF expression and hence the PDF. The parametric method is applied here. In the case of a Gaussian PDF, the parameters (mean and standard deviation) can be estimated through the commonly used maximum likelihood estimation. Apart from maximum likelihood estimation, the method of moments can also be used (Wasserman, 2013). It does not provide optimal estimators, but the method of moments is still applied because it is easy to compute. The PDF form is difficult to infer accurately, and thus it is normally unknown beforehand. Under most circumstances, the PDF is simply assumed to be Gaussian (Farrar and Worden, 2012; Yan et al., 2005a; Bao et al., 2013a). One justification of this assumption is based on the central limit theorem, which states that the distribution of the sum of random variables converges to Gaussian as the number of these random variables becomes infinity. For VBDD, a feature can be affected by various factors such as environmental conditions and measurement noise. Each of these factors can be viewed as a random variable, and the feature represents the summation of these random variables. Therefore, the distribution of the feature converges to be Gaussian.

In many cases, the PDF form is unknown and has to be estimated from the data using parametric methods or non-parametric methods. One popular parametric method is based on mixture models such as Gaussian mixture models (Slonski and Słoński, 2017; Nair and Kiremidjian, 2007; Yu, 2011). The commonly used non-parametric method is the kernel density estimation method (Worden et al., 2003; Eltouny and Liang, 2021; Liang et al., 2018a).

Control charts (Montgomery, 2007), anomaly detection techniques for quality control, are essentially density-based methods and have been used for VBDD. It plots a statistic of the process over time, along with two horizontal lines: lower control limit and upper control limit. These control limits are chosen so that if the process is in control, nearly all of the sample points will fall between them. On the other hand, a point that plots

outside of the control limits indicates that the process is out of control, and an alarm will be triggered. Control charts have a well-established framework with various statistics and rigorously derived control limits. In addition, it inherently provides an automatic and online method for structural health monitoring. Due to these reasons, they have been applied in many studies for damage detection of civil infrastructure (Fugate et al., 2001; Kullaa, 2003; Deraemaeker et al., 2008; Mújica et al., 2011; Chandrasekhar et al., 2021) .

#### 2.1.2.2 Boundary-based methods

Boundary-based methods learn the boundary between two classes. A well-known example is support vector machines (SVMs), which are supervised methods and normally used for classification. But it can be adapted for novelty detection, resulting in the one-class SVM (Schölkopf et al., 1999). One-class SVM relies on one-class data (i.e., features from the undamaged state) and learns the boundary (hyper-plane) that maximises the margin between the training data and the origin. For VBDD, if a new feature value is outside of the hyper-plane, it will be said to be from a damaged state, such as in Saari et al. (2019), Long and Büyüköztürk (2017) and Anaissi et al. (2019).

There are other boundary-based methods, such as support vector data description (Tax and Duin, 2004) and Mahalanobis ellipsoidal learning machine (Wei et al., 2007). support vector data description aims to find a hyper-sphere that encloses almost all the training data but with minimum volume. It is equivalent to one-class SVM when Gaussian kernels are used (Tax and Duin, 2004). As for Mahalanobis ellipsoidal learning machine, it is the same as support vector data description except that it uses a hyper-ellipsoid instead of a hyper-sphere. Inspired by this, a convex hull has also been proposed to describe the geometry of the training data, yielding the one-class classification based on the convex hull method (Zeng et al., 2016).

### 2.1.3 Challenges in vibration-based damage detection

Unlike mechanical and aerospace structures, civil structures have seen few practical applications due to the uniqueness of the structures and complex environment and operational conditions. To transfer the VBDD from the laboratory to the field, several challenges need to be addressed. These challenges and the relevant studies are discussed in this section.

#### 2.1.3.1 Damage sensitive features

Feature extraction is a fundamental step for VBDD and plays a crucial role in improving the performance of the damage detection methods. Although different features have been proposed, they have various limitations. For example, modal parameters are insensitive to local damage; finite element model updating is computationally heavy for large structures; many machine learning methods are difficult to interpret. In addition, features may suffer from EOV effects, leading to unreliable damage detection results. Furthermore, new damage detection scenarios emerge, and they may require specifically designed features. All these factors make it necessary to develop new features.

#### 2.1.3.2 Methods for nonlinear structures

Most existing VBDD methods assume that the structure behaves linearly before and after damage. Although nonlinearity has been considered in VBDD, its application is normally limited to the scenario where the system is linear in the undamaged state and becomes nonlinear in the damaged state (Worden et al., 2008). However, many real-world structures will exhibit nonlinear responses even in their undamaged states, especially when the vibration amplitudes are large. VBDD problems for these initially nonlinear systems have rarely been studied. In 2010, Bornn et al. (2010) first addressed the issue and applied an autoregressive support vector machine (AR-SVM) method. However, the AR-SVM method and other alternatives for characterising nonlinearity have been criticised for their lack of generality (Shiki et al., 2017; Villani et al., 2019a). That means it is difficult to obtain a general model that can describe all structures of interest. Therefore, Shiki et al. (2017) proposed to use a Volterra series model, which is a generalisation of the linear convolution representing the linear and nonlinear responses of a dynamical system in a separable way. The Volterra series model has been further studied in relation to uncertainties and experimental data in the last two years (Villani et al., 2019a,b, 2020). However, the Volterra series model relies on input signals, making it impractical for applications on large civil engineering structures, where the input is generally unknown.

#### 2.1.3.3 Removing environmental and operational variations

Environmental and operational variations (EOVs) can significantly alter the dynamic response features and often mask subtle changes in the vibration signals caused by damage (Farrar and Worden, 2012; Brownjohn et al., 2011). In the last two decades,

numerous methods for removing the EOV effects have been proposed. They can be roughly divided into two categories: cause-effect methods and effect-only methods, depending on if the EOV parameters are required.

The cause-effect methods rely on both EOV parameters (cause) and structural vibration features (effect), based on which a regression model is trained for the undamaged state. By substituting new EOV parameters into the model, the residual between the measured features and the predicted features is used to indicate damage. The simplest model in this category is a linear regression. For example, Kim et al. (2007) applied a linear regression model to express the empirical relationship between temperature and the frequency ratio. Considering the temperature distribution is usually non-uniform for large structures, it is more reasonable to measure the temperature at multiple locations, leading to the application of multivariate linear regression models (Sohn et al., 1999; Xia et al., 2011). Furthermore, the relationship between the cause and effect can be complicated and nonlinear. For example, the relationship between the natural frequencies of the Z24 bridge and temperature is bilinear, with the knee situated around 0 °C (Peeters and De Roeck, 2001). These problems can be tackled by nonlinear models such as support vector regression (SVR) (Ni et al., 2005; Kromanis and Kripakaran, 2013), autoregressive with eXogeneous input model (Peeters and De Roeck, 2001; Moser and Moaveni, 2011), ANN (Zhou et al., 2011; Jin et al., 2016), and Gaussian process regression (GPR) (Avendaño-Valencia and Fassois, 2017b; Avendaño-Valencia et al., 2020). The cause-effect methods are straightforward but demand EOV measurements, which may not be available for large structures because of equipment requirements or loss of data.

The second category of methods, effect-only methods, only requires vibration data. Various approaches have been applied in this category. One line of these methods follows the idea that the features can be transformed into a subspace where the effects of EOV are absent, with PCA as one popular method (Yan et al., 2005a; Kromanis and Kripakaran, 2016; Soo Lon Wah et al., 2018). For vibration responses with complex nonlinearity, it is suitable to apply nonlinear PCA such as adaptive PCA (Jin et al., 2015), local PCA (Yan et al., 2005b), and kernel PCA (Lim et al., 2011). Another implementation of the nonlinear PCA is using ANN architecture, resulting in an auto-associative neural network model (Li et al., 2010; Sohn et al., 2002; Zhang et al., 2019; Ye et al., 2020; Hsu and Loh, 2010; Gu et al., 2017). These PCA-based methods are black-box models; that means they do not have an explicit expression for the relationship between input and output; therefore, they are less interpretable than the cause-effect methods. Another line of the effect-only methods separates EOV effects and other load effects on vibration

response by taking advantage of the fact that the EOV effects have distinguishable frequencies. One example is temperature-induced strain has a lower frequency than the vehicle-induced strain as reported in Xia et al. (2017). Hence, the temperature effects can be removed by decomposing the vibration signals and discarding the lower frequencies. The applied decomposition methods include empirical mode decomposition (Xia et al., 2017; Wu et al., 2018; Zhu et al., 2018) and wavelet transform (Ni et al., 2012; Zhao et al., 2019; Xu et al., 2020). Another example is the 1P and 3P loads of wind turbines. Obviously, these methods rely on accurate prior knowledge of the frequencies of EOV effects. In addition, cointegration is another class of effect-only methods. It assumes that the EOV effects can be removed by linearly combining some original processes and has been used to remove temperature fluctuation effects (Cross et al., 2011, 2012; Liang et al., 2018b).

## 2.2 Vibration-based damage detection for offshore wind turbines

Offshore wind power is one of the most promising renewable energy sources and has become a rapidly developing industry worldwide. Despite its remarkable growth, the offshore capacity is much smaller than onshore due to the high costs of offshore projects (Global Wind Energy Council, 2021). To reduce the costs, VBDD has been applied to OWTs to optimise operation and maintenance activities, as discussed in Section 1.1. However, most of the existing studies concern blades or gearboxes of OWTs, whereas foundations are rarely investigated. Therefore, this thesis concentrates on applying VBDD to OWT foundations and provides a review of it in this section. Having said that, Section 2.2.1 presents an overview of OWTs, focusing on foundation types and their structural dynamics. After a brief review of VBDD applications on blades and gearboxes in Section 2.2.2, Section 2.2.3 highlights the research on support structures (including towers, transition pieces and foundations), especially on foundations.

### 2.2.1 Overview of offshore wind turbines

An OWT mainly consists of a rotor-nacelle assembly and a support structure, as shown in Figure 2.1. The figure also illustrates the main parts of support structures; that is, tower, transition piece and foundation. The details of the rotor-nacelle assembly can be

found in Figure 2.2, which shows the main parts of the rotor-nacelle assembly, including blades, a rotor, a gearbox, a generator, bearings, and a yaw system.

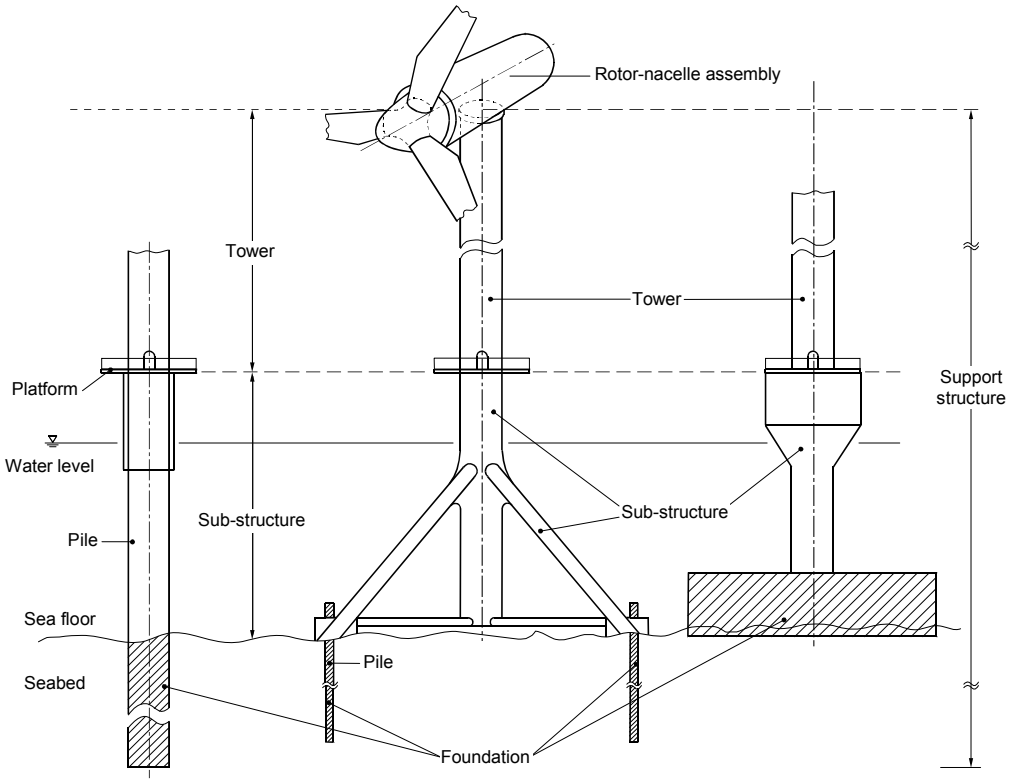


Figure 2.1: Parts of an offshore wind turbine (IEC 61400-3, 2009).

#### 2.2.1.1 Foundation types

OWTs have been installed on various types of foundations, which basically fall into two categories: fixed foundations and floating foundations. Common fixed foundations include gravity base, suction bucket monopile, monopile, tripod and jacket foundation (Wu et al., 2019), as shown in Figure 2.3. Gravity base foundations take advantage of their weight to resist overturning moments of OWTs and keep support structures upright on the seabed. They are normally made of concrete and are usually situated in water depths less than 10m. This type of foundation was widely used in the early stage of offshore wind development. Monopile foundations rely on the signal pile driven into the soil to support OWTs. These structures have a diameter of 3-8 m and are usually located in water depth ranging from 20 to 40 m. A tripod foundation is generally a three-legged

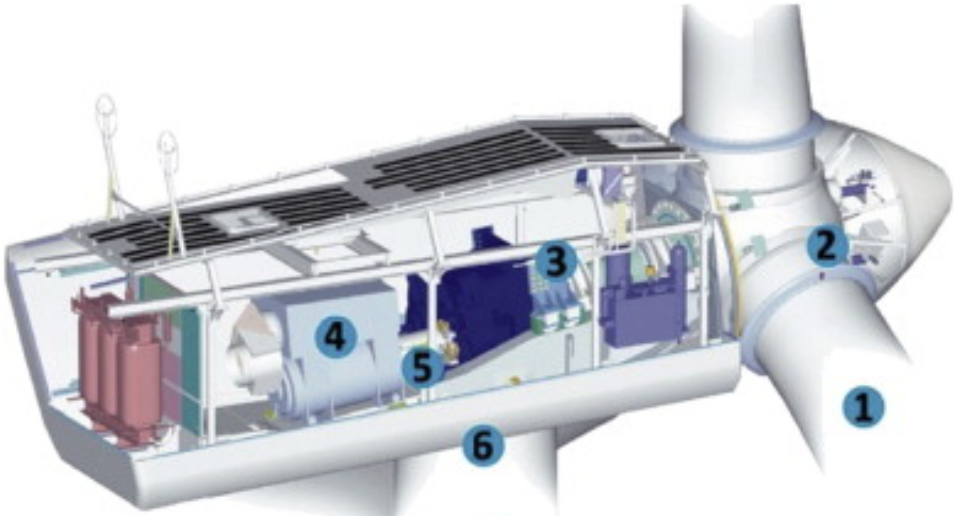


Figure 2.2: Main parts of rotor – nacelle assembly (1) blades, (2) rotor, (3) gearbox, (4) generator, (5) bearings, and (6) yaw system (Márquez et al., 2012).

steel jacket. The forces from the tower are transferred into three piles through a frame. The three piles are driven 10-20 m into the seabed depending on soil conditions. The tripod foundation is suitable for water depths of 10–35 m. As water depth goes deeper ( larger than 50 m), jackets become popular; a jacket is a lattice framework with four legs anchored to the seabed by piles.

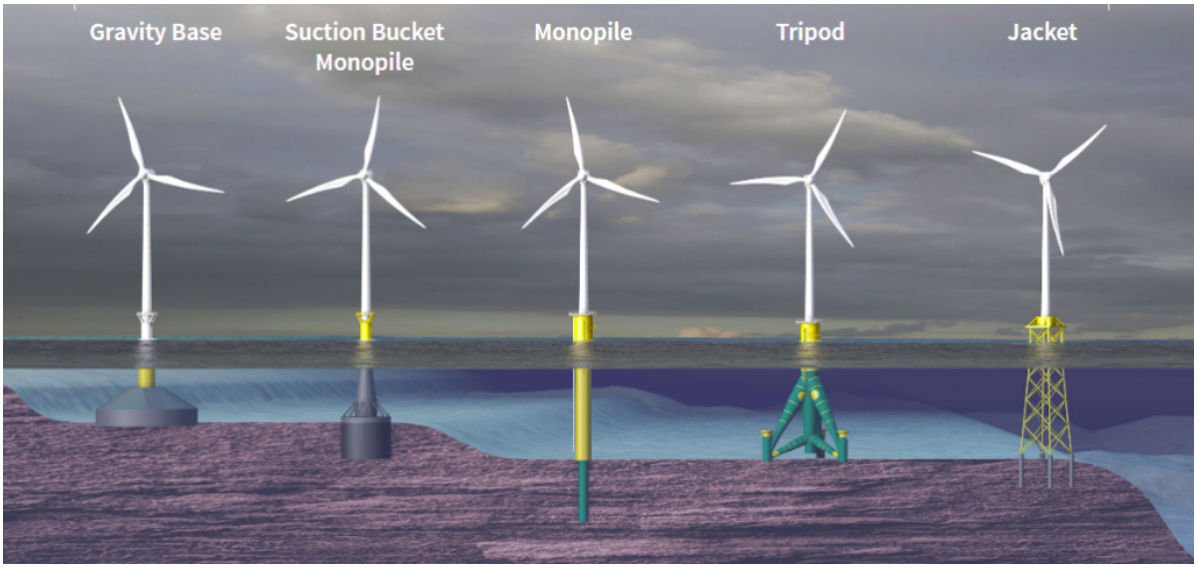


Figure 2.3: Various types of fixed foundations for OWTs (Ferreira, nd)

Due to the cost-effective design, fabrication and installation, monopile foundations have been used in many large-scale offshore wind farm projects (Kallehave et al., 2015).

#### 2.2.1.2 Structural dynamics of support structures

This section presents the structural dynamics of OWTs, with emphasis on foundations. Different loads of OWTs are introduced, followed by a discussion on the structure system and modelling.

OWTs are subjected to harsh environmental conditions and are normally in operation with rotating blades. Support structures are mainly used to counter the overturning thrust load and achieve stability. The main loads for support structures include (DNVGL-ST-0126, 2016; DNVGL-ST-0437, 2016; IEC 61400-3, 2009):

- *Wind loads*. Wind loads are mainly acting on blades and are transferred to the tower top as a trust force. They are affected by mean wind speed, turbulence, rotational speed of the rotor, air density, and so force. For simplification, the wind speed can be divided into a mean wind speed and a turbulence wind speed, corresponding to a mean wind trust and a turbulence wind trust (Arany et al., 2015).

- *Wave loads*. Wave loads are acting on the support structure under mean sea level and its adjacent area as a distributed force. These forces depend on wave height, wave period, water depth, water density and the shape of the structure. One simplified method for the calculation of wave loads is Morison's equation (Morison et al., 1950), which is a prevailing method for OWT foundations (Hallowell et al., 2016; Wei et al., 2017; Arany et al., 2014; Ma et al., 2017).

- *1P load*. This load is caused by the rotating rotor that has mass or aerodynamic imbalances. It arises in each revolution of the rotor; hence it has the same frequency as the rotation of the rotor, explaining the name '1P' (once-per-revolution (Nandi et al., 2017)). It is worth noting that the frequency of 1P load is not a fixed value but a range of values due to the variable-speed design of modern wind turbines.

- *3P load*. This is a force caused by the tower shadow effect, which means the wind speed will reduce in the regions both upwind and downwind of the tower due to the airflow blocking by the tower (Burton et al., 2011). Therefore, whenever a blade passes by the tower, a force will arise due to the wind speed reduction upwind of the tower; hence, it is referred to as a 3P (thrice-per-revolution) load for a popular three-blade wind turbine. In rare cases where a wind turbine has two blades, it is referred to as a 2P load. Similar to the 1P load, the 3P/2P load also has a frequency band.

A typical frequency distribution of the excitation of an OWT is shown in Figure 2.4 (Nikitas et al., 2016). As discussed above, the frequencies of 1P and 3P loads are plotted in bands. The wind and wave loads are modelled by the Frøya spectrum and JONSWAP spectrum, respectively. When designing the support structure, it is clear in Figure 2.4 that the frequency of the whole OWT should keep away from these frequency bands to avoid resonance, and ultimately increased fatigue damage.

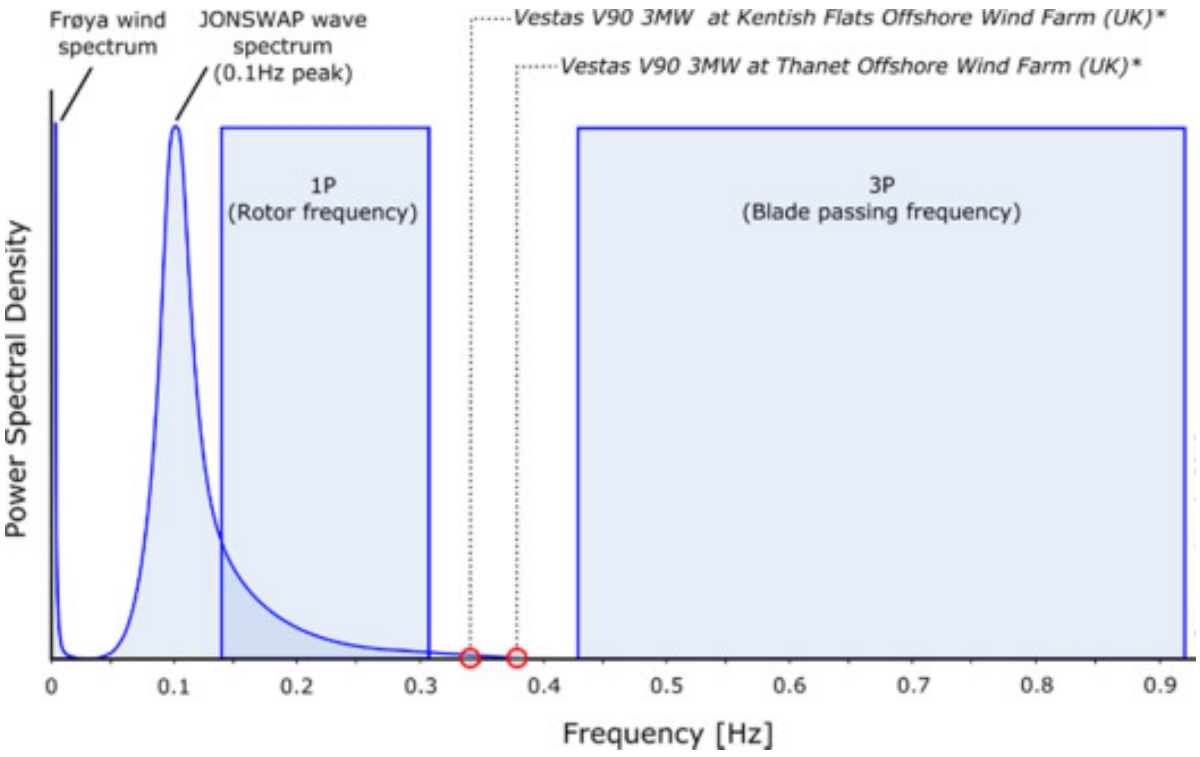


Figure 2.4: Frequencies of excitation of the Vestas V90 3MW OWT (Nikitas et al., 2016)

A design with a frequency below 1P band is almost impossible for a grounded system (Arany et al., 2014). It seems safer to have a system with frequency beyond the 3P band, but this means the support structure is extremely heavy, causing increasing costs for material, manufacture and installation. Hence, almost all existing OWTs are designed to have a frequency in the gap between the 1P and 3P bands (Arany et al., 2014). As this gap is normally narrow, OWTs are sensitive to dynamic loads.

For calculating OWT dynamic loading and response, aero-hydro-servo-elastic modelling is needed. There are several simulation tools available, such as FAST from National Renewable Energy Laboratory (Jonkman and Buhl Jr, 2005), Bladed from DNV (DNV, 2020), and HAWC2 from the Technical University of Denmark (Larsen and Hansen, 2007) to name a few. They can model stochastic wind and wave loading as well as

non-linear control actions in a time-domain simulation. Take Bladed as an example; dynamic analysis is conducted by a multi-body dynamics approach where the structural components are assumed to be either rigid or flexible. Rigid components, such as yaw and blade bearings, are relatively easy to model. The flexible components, such as tower, blades and foundation, are modelled by the multi-member modal approach (DNV, 2020). They are generally assumed as space frames modelled by Timoshenko beam elements in a finite element model. For a support structure, the parts above the seabed, including the tower and a part of the foundation, is modelled with linear beam elements. The part under the seabed, however, is relatively difficult to model because of the soil-pile interaction.

Soil-pile interaction plays a major role in the dynamic response of OWTs with fixed foundations (Løken and Kaynia, 2019). For accuracy, it is preferable to use a finite element model of the soil-pile interaction. However, this approach is very computationally heavy. Therefore, it is typical to model the monopile structure below the mudline with coupled springs (Jonkman et al., 2008a). That means the monopile under the mudline is idealised as a stiffness matrix positioned at the mudline. A more complex model is used when the nonlinear soil-pile interaction is considered. In this model, the pile is supported by a series of non-linear elastic springs (Vieira et al., 2020; Carswell et al., 2015). The springs are described by p–y curves, which define the load–displacement relationship for the interaction between soil and pile (American Petroleum Institute, 2000; Andersen et al., 2012).

### 2.2.2 Vibration-based damage detection for blades and gearboxes

Studies on blades and gearboxes are the majority of VBDD applications on OWTs. Although they are not the focus of this thesis, a brief review of them is helpful to provide a big picture of the VBDD applications on OWTs. In addition, the knowledge and lessons from the blades and gearboxes may throw light upon the work on VBDD for foundations.

#### 2.2.2.1 Blades

Blades are used to gathering power from wind and are key components for wind turbines. Most blades are composed of glass fibre reinforced polymer (Yang et al., 2016) due to its low cost, lightweight and excellent strength to weight ratio (Mishnaevsky et al., 2017; Katnam et al., 2015). Blades may suffer from manufacturing flaws, as well as harsh

environmental conditions. Typical manufacturing flaws include delaminations, adhesive flaws and resin-poor areas (Drewry and Georgiou, 2007). During operation, blades can be damaged by their surrounding environment, such as lightning, uneven ice accumulation, wind gust and so forth (Li et al., 2015a). Overall, common damages on blades can be summarised as icing, delamination and debonding (Garolera et al., 2014; Du et al., 2020; Li et al., 2015a).

A large number of damage detection methods have been employed for blades damage detection. Many of them are based on signals such as acoustic emission (Tang et al., 2016), thermography (Galleguillos et al., 2015), ultrasound (Park et al., 2014) and machine vision (Stokkeland et al., 2015). Due to the advantages such as being non-destructive, easy to implement and able to localise and quantify the damage (Beganovic and Söffker, 2016; Du et al., 2020), vibration-based methods have also been used. A pioneer work is from Ghoshal et al. (2000), which studied a blade in a laboratory using four damage detection methods (transmittance function, resonant comparison, operational deflection shape, and wave propagation methods) and two measurement techniques (piezoceramic sensor patches bonded to the blade, and a scanning laser doppler vibrometer). Also in the laboratory environment, Wang et al. (2014) successfully localised and quantified the blade damage by using a finite element updating method. Field data from a wind turbine park located in Northern Europe were used in Skrimpas et al. (2016) for icing detection. More recently, it is suggested that non-contact and remote non-destructive inspection methods should be used for blades (Yang and Sun, 2013). Accordingly, ground-based radar, which can measured vibration response, has been used for damage detection of blades (Summers et al., 2016; Talbot et al., 2016; Moll et al., 2018).

#### 2.2.2.2 Gearboxes

A gearbox is typically used to increase the low rotational speed of a rotor to match the higher rotational speed of an electrical generator. Among all components, the gearbox accounts for one of the largest parts of downtime for wind turbines (Hahn et al., 2007). For gearboxes, damage detection, or more broadly SHM, is often referred to as condition monitoring, which is a specific and well-developed area for monitoring rotating machinery.

Different techniques have been used for condition monitoring of gearboxes, such as lubrication analysis, acoustic emission, vibration analysis, machine current signature analysis and so forth (Salameh et al., 2018). For vibration-based methods of planetary gearboxes, there are time-domain averaging (McFadden, 1991), time-frequency anal-

ysis (Williams and Zalubas, 2000), statistical analysis (Samuel and Pines, 2005) and cyclostationary analysis (Zimroz and Bartelmus, 2009). These methods have been applied and enriched the knowledge for wind turbine monitoring, but challenges still exist. The main challenges lie in the complicated vibration response due to multiple planet gears and the changing rotational speed and load caused by varying wind conditions (Wang et al., 2019).

However, it should be noted that a wind turbine does not necessarily have a gearbox. To eliminate gearbox failure, direct-drive wind turbines have been developed (Polinder et al., 2006). For these wind turbines, the generator is 'directly' driven by the rotor, resulting in an equivalent rational speed between the generator and the rotor.

### 2.2.3 Vibration-based damage detection for support structures

Compared with blades and gearboxes, support structures of OWTs are rarely studied. This is likely to be because support structures have lower failure rates and need less regular maintenance. However, unlike blades and gearboxes which are relatively easy to replace, support structures cannot be replaced in the same way as blades and gearboxes. Hence, they are critical components and should be monitored. In the remaining of this section, the VBDD applications on the three main components (i.e., tower, transition piece and foundation) of a support structure are discussed, concentrating on foundations.

#### 2.2.3.1 Tower

The tower supports blades and nacelle and lifts them to a taller height for capturing larger wind speed. It is normally made of tubular iron sections that are connected together with flanges. For tower monitoring, strain gauges and acceleration measurement sensors are most commonly used (Wondra et al., 2019).

Rolfes et al. (2007) detected stiffness reduction for two wind turbine towers in northern Germany using the proportional relationship between dynamic stress and dynamic velocity, which were obtained from strain gauges and accelerometer, respectively. A finite element model was also developed for damage localisation and quantification. Bogoevska et al. (2017) considered environmental and operational variations for tower damage detection. In the short term scale, periodic fluctuations caused by 1P and 3P loads are dominated and tackled with a time-varying autoregressive moving average model. In the long term scale, variations such as wind speed change become principal. Hence, the model was combined with a polynomial chaos expansion model, which links the

environmental parameters with the model coefficients. Schröder et al. (2018) studied damage localisation for support structures of a simulated monopile OWT and a lab-scaled tri-pile OWT using a new adapted finite element model updating method. For simplifying installation, saving sensor cables and avoiding electromagnetic interference, wireless sensors have been introduced to monitoring systems of wind turbine towers and have been proved to have an equivalent quality of data acquisition with the traditional wired sensors (Rolfes et al., 2007; Wondra et al., 2019).

#### 2.2.3.2 Transition piece

The transition piece connects the tower and the pile and transfers the shear and bending loads between them. The grout in the transition piece has been viewed as a critical area since 2010, when the grouted connection between turbine structures and their monopile foundations was reported to slip downwards by up to 25 mm in a wind farm (Faulkner et al., 2012). This made a number of wind farm developments embarked upon an SHM system on the transition pieces. James Fisher Strainstall had installed a monitoring system to tackle this (Faulkner et al., 2012). The monitoring system is comprised of an array of strain gauges, displacement sensors and accelerometers, along with bespoke personal computer monitoring equipment. Natural frequencies and the inclination of the tower were monitored.

Due to the concern above, many alternatives to the grouted connection have been proposed. The most popular one is the bolted ring-flange connection, which is very common in China and has been applied in Europe (Weijtjens et al., 2021). This kind of connection gets rid of grout slipping but still needs monitoring of bolts due to fatigue damage.

#### 2.2.3.3 Foundations

OWT foundations can be affected by scour: the erosion of the mudline near the foundation. Unexpected scour damage may be caused by extreme events, strong currents, and scour protection failures. Scouring can reduce the resonance frequencies of the OWT; studies show that the first natural frequency of the OWT with a monopile foundation can be reduced by 5% – 10% (Devriendt et al., 2014; Prendergast et al., 2015). This reduction leads to a critical problem for foundation integrity. This is because the first resonance frequency becomes closer to the frequency range in which the wave and gust energy is concentrated. That means more energy can create resonant behaviour increasing fatigue damage. In addition, the reduced higher resonance frequencies might coincide with

some of the higher-order rotor harmonics such as 3P and 6P. This effect also increases resonant behaviour and thus fatigue damage (Devriendt et al., 2014). Furthermore, scour can increase hydrodynamic loading on the foundation and increase bending stresses on cables, reducing the lifetime of these components (Michalis et al., 2013). Therefore, continuously monitoring the scour and foundation integrity is of great importance for reducing costs and extending the lifetime of OWTs.

Various methods have been proposed for scour monitoring, although mainly for bridges (Prendergast and Gavin, 2014). These methods mostly use underwater instrumentation such as buried devices, radar and sonar, leading to a high installation and maintenance cost (Prendergast and Gavin, 2014). For example, Michalis et al. (2013) proposed to install a probe with several sensors under the seabed for scour monitoring. Each sensor is composed of a pair of stainless steel rings separated by an insulating gap, where the capacitance will change if the sensor is uncovered; hence, the scour progress is monitored. The cost can become even higher for OWTs due to the harsh environment and difficult access to the OWT sites. On the other hand, vibration-based methods, which rely on mature and reasonably low-cost signal measurement and acquisition technologies, have attracted more and more interest for scour monitoring of OWTs (Weijtjens et al., 2016; Samusev et al., 2019).

Weijtjens et al. (2016) provided a scour assessment method by monitoring the resonance frequencies of the OWTs in Belwind wind farm located 46 km outside the Belgian coast. In their work, real-world data were used. It is found that the second-order mode is more sensitive to the scour than the first mode. In addition, the resonance frequency in the side-side direction is preferable as it is not affected by the aerodynamic damping and can be more accurately estimated. Therefore, the second-order resonance frequency in the side-side direction was used as the feature. Although the studied OWTs were not in operation, they are still subjected to environmental variations, such as the tidal level. To compensate for this, a linear regression model between the environmental parameters and the feature was developed. An increasing resonance frequency was observed, pointing in the opposite direction of scouring. This indicates a stiffening of the structure, which was supposed to be caused by the soil stiffness change due to cyclic loading.

In Oliveira et al. (2018), a scour depth of 0.075 times the monopile diameter was considered, corresponding to a decrease of the first tower bending modal frequency of around 0.2%. To obtain the data of the damaged state, the second mode of the support structure of the undamaged state was artificially adapted according to the reported relationship between frequencies and scour depth in the literature. After removing

the EOV effects with a multivariate dynamic regression model, the second natural frequencies were used to indicate the scour damage by $T^2$ control charts.

Based on numerical data, Tang and Zhao (2021) studied scour detection of the monopile OWTs in the Jiangsu Rudong Offshore Demonstration Wind Farm located in the inter-tidal zone (3–7 km offshore). Two features, the growth rates of the mode coefficient and the inclinations, both at the tower bottom, were used to indicate the scour damage. A scour depth of 5m, approximately equal to the pile diameter, was set as the threshold for structural safety warnings. The corresponding values of the features were first obtained from the numerical model and then compared with a new observed feature to decide if the scour depth had exceeded the threshold.

Another common failure for foundations is the development of cracks. Opoka et al. (2016) studied a scaled tripod under hammer impacts in the laboratory environment and proposed to use the root mean square deviation of the frequency spectrum of the measured strain data as the damage index for detection and localisation of simulated crack damages. It should be noted that the localisation here does not mean the exact location but the localisation of structural members such as the upper brace, the lower brace and the pile guide. In a follow-up study (Mieloszyk and Ostachowicz, 2017), where the experiments were performed in a water basin, and artificial wave and blades rotating were simulated, four damage indices based on operational modal analysis and strain energy were used for crack damage detection and localisation. The study was further extended by adding a new damage scenario (i.e., deterioration of the support condition) (Soman et al., 2018). More recently, Luczak et al. (2019) used accelerations under wave excitation, rather than strains in previous studies, for detecting and assessing the simulated cracks using operational modal analysis. These studies have provided valuable knowledge for crack detection of foundations, but they are limited to the laboratory environment.

## 2.3 Summary

This chapter has presented a comprehensive review of vibration-based damage detection and its applications for offshore wind turbines. Based on the challenges identified for VBDD in Section 2.1.3 and the existing studies on OWTs, the following key research needs will be addressed in this thesis:

(1). *Identification of damage-sensitive features from dynamic analysis data.*

Selecting damage-sensitive features is critical for the effectiveness of a damage detection method. Numerous features have been reviewed in this chapter, but new features that are sensitive to damage, insensitive to environmental and operational variations, easy to implement, and interpreted are still desirable. As for OWTs, most features used in the literature are modal parameters. More alternative features, existing or novel, should be explored to improve the VBDD performance on OWTs.

(2). *Improving damage detection in initially non-linear structures.*

Most existing vibration-based damage detection methods studied systems that are linear both before and after damage. Some researchers have also addressed damage detection problems for structures that are linear before damage but nonlinear after damage. However, structures can be nonlinear both before and after damage. For example, both the soil-pile interaction and blades of OWTs can be nonlinear before and after damage. But this scenario has been paid little attention.

(3). *Developing damage detection methods that are robust to changes in environmental and operational conditions.*

Removing the effects of environmental and operational variations is one of the most important issues for the real-world applications of vibration-based damage detection. For structures that are subjected to complex environmental and operational variations, such as OWTs, it becomes more challenging. Although various methods have been proposed to tackle this issue, these methods may require a large number of data or be less explicable.

Addressing these research challenges is the primary focus of Chapter 3, Chapter 4 and Chapter 5, respectively.

CHAPTER 3

# Damage Detection by Comparing Multivariate Probability Density Functions of Vibration Data

In the previous chapter, existing vibration-based damage detection methods have been reviewed. Despite the vast number of these methods, there are no universal techniques that can detect all damage types of different structures. New methods are still emerging to tackle new damage scenarios or improve the damage detection performance. In this chapter, a method based on a novel feature is proposed for linear structures subject to Gaussian white noise loading. When applied to a monopile wind turbine foundation, the proposed method is shown to give improved damage detection performance compared to traditional methods.

---

This chapter is adapted from the manuscript:

Zhang Y., Macdonald J.H.G., Liu S., Harper P. (2021). Structural damage detection by comparing multivariate probability density functions of vibration data. Manuscript submitted for publication.

Part of the introduction has been removed and included in Chapter 2 - Literature Review.

## Authors' contributions

Zhang Y. conceived the idea, performed the numerical simulations, and implemented the method, with supervisory support from Macdonald J.H.G. on the development of the idea. All authors contributed to the preparation of the manuscript.

## 3.1 Introduction

Structural health monitoring (SHM) has been used to automatically detect, identify, and estimate damage in civil infrastructure, allowing cost-effective management of maintenance activities. Within the SHM research community, vibration-based damage detection (VBDD) has gained widespread interest for several reasons, such as its 'global' coverage, ability to automate, and mature and reasonably low-cost signal measurement and acquisition technologies (Fassois and Sakellariou, 2007). The underlying principle of VBDD is that damage will change the physical properties of a structure and, consequently, change the measured vibration response of the structure.

Apart from the existing methods mentioned in Chapter 2, an alternative, yet seldom applied, approach is to use the multivariate probability density function (PDF) of random vibration response. It is worth noting that the multivariate PDF mentioned here is different to most existing PDF-related studies which use PDFs to describe the distributions of features such as transmissibilities (Worden et al., 2003) and cumulative intensity measures (Eltouny and Liang, 2021). The multivariate PDF in this chapter is a description of the stochastic process of random vibration. More precisely, the reading at a time instant from a sensor is treated as a random variable. All the random variables for different time instants compose a stochastic process. For the clarity of the following discussion, it is worth mentioning that the autocorrelation function of the stochastic process is the correlation between two random variables from the same sensor, while the cross-correlation function is between the random variables of different sensors. There have been few studies related to the PDFs of random vibration signals. In Figueiredo et al. (2009), univariate PDFs of vibration signals were used for damage detection. The key idea was that the PDF of the acceleration from the undamaged state of a linear system is Gaussian, while the PDF becomes non-Gaussian if nonlinear damage occurs. As such, the damage was detected by monitoring the Gaussianity of the PDF of the potentially damaged state. Although not mentioned in the original study (Figueiredo et al., 2009), the univariate PDF can be seen as a PDF of a random variable at a single time instant from the stochastic process with the assumption of ergodicity. Mújica et al. (2013) treated the time series from multiple sensors as a realisation of a stochastic process. Multiple realisations from repeated experiments were first processed with principal component analysis; then, the population means of the processed realisations from the undamaged state, and the sample mean of a processed realisation from a potentially damaged state were compared to detect damage. Yang et al. (2007) also used the time

series from multiple sensors and regarded them as realisations of an ergodic stochastic process. The damage was detected by taking advantage of the cross-correlation function of the stochastic process. One major drawback of these studies is that only partial information of the stochastic processes is used; specifically, the autocorrelation information is not considered.

This chapter proposes a new vibration-based, output-only damage detection method. In this approach, the vibration response is treated as a stochastic process and is characterised by the multivariate PDF of the stochastic process. The autocorrelation information is accounted for inherently by the PDF. The change between the multivariate PDF of the undamaged state and that of a potentially damaged state is used to indicate the occurrence of damage. This chapter focuses on a linear system under ambient excitation and noise; both assumed to be Gaussian white noise. The main novelty is the use of the multivariate PDF as a feature for VBDD, which is demonstrated to be superior over an autoregressive-based method and an autocorrelation function-based method in this chapter.

In the remainder of the chapter, the proposed method is explained in Section 3.2 and discussed in Section 3.3. Section 5.4 introduces the numerical simulation of an offshore wind turbine, followed by the case study results of the offshore wind turbine and comparative studies in Section 5.5. Finally, the main conclusions are presented in Section 5.6.

## 3.2 Proposed probability density function-based method

### 3.2.1 PDF characterisation of vibration response

Many excitations in civil engineering, such as seismic ground motions, wind buffeting and wave loading, exhibit an obvious character of randomness; therefore, they are termed stochastic processes (Lutes and Sarkani, 2004). For a structure subjected to these stochastic excitations, its response measurement is also a stochastic process. The process is a set of random variables that are indexed by time and equally spaced in time. It can be denoted as $\{X(t_i), i = 1, 2, \cdots, N\}$, where $i$ represents the time index, $N$ is the total number of time instants, and $X(t_i)$ is a random variable at time $t_i$. In other words, a time series record of the vibration response is viewed as a realisation of a stochastic process. The stochastic process can be completely characterised by an $N$-dimensional PDF (Lutes and

Sarkani, 2004), which contains the correlation information between random variables with different time lags between them (from one sample period to N-1 sample periods). However, the estimation of such a PDF demands an enormous amount of data and a huge computational burden if $N$ is large. To overcome this problem, the $N$-dimensional PDF is truncated to a $k$-dimensional PDF, denoted as $p(\mathbf{x})$, where $1 \leq k \leq N$, neglecting any correlation between random variables with time lags larger than $k$ sample periods. The $\mathbf{x}$ in $p(\mathbf{x})$ represents a sample, $\{x_1, x_2, \cdots, x_k\}$, of the $k$-dimensional random vector $\{X(t_1), X(t_2), \cdots, X(t_k)\}$ at $k$ consecutive time instants. As such, the vibration response is characterised by the $k$-dimensional PDF, $p(\mathbf{x})$, where $k$ is a parameter to be determined.

In this chapter, the excitations and the noise are assumed to be Gaussian white noise, and the system is assumed to be linear. Therefore, the vibration response is also Gaussian white noise, which is a Gaussian process (Lutes and Sarkani, 2004). The truncated PDF of the Gaussian process is

$$p(\mathbf{x}) = \frac{1}{\sqrt{(2\pi)^k |\mathbf{C}|}} \exp\left( -\frac{(\mathbf{x}-\boldsymbol{\mu})\mathbf{C}^{-1}(\mathbf{x}-\boldsymbol{\mu})^{\mathsf{T}}}{2} \right) \tag{3.1}$$

where $\boldsymbol{\mu}$ represents the means of the PDF, $\mathbf{C}$ is the covariance matrix of the PDF, $|\cdot|$ means determinant of the matrix and superscript $\mathsf{T}$ represents the transpose of the matrix.

### 3.2.2 PDF estimation in practice

Given a vibration response from a single sensor,

$$\{x_1, x_2, \cdots, x_N\} \tag{3.2}$$

where $N$ is the total number of time instants, it is first processed to mitigate effects that may have occurred due to different loading conditions (Nair et al., 2006; Sohn and Farrar, 2001; Bao et al., 2013a). Specifically, the record is standardised by subtracting its mean and then dividing by its standard deviation.

As discussed above, the vibration response is characterised by $p(\mathbf{x})$ in equation 3.1. However, it is difficult to estimate the PDF with only one realisation (sample). In practice, the ergodicity assumption is generally introduced (Li and Chen, 2009). That allows using a time average obtained from one time series realisation of a stochastic process as estimate of a mathematical expectation. A practical way to implement this idea is to

rearrange the time series into a Hankel matrix:

$$\begin{bmatrix} x_1 & x_2 & \cdots & x_k \\ x_2 & x_3 & \cdots & x_{k+1} \\ \vdots & \vdots & \ddots & \vdots \\ x_{N-k+1} & x_{N-k+2} & \cdots & x_N \end{bmatrix} \tag{3.3}$$

In the Hankel matrix, each row can be viewed as a sample of $p(\mathbf{x})$. With these samples, the parameters of the Gaussian PDF, $p(\mathbf{x})$, can be easily estimated. Specifically,

$$\boldsymbol{\mu} = \{\mu_i,\, 1 \le i \le k\} = \{\frac{1}{N-k+1} \sum_{i=1}^{N-k+i} x_i,\, 1 \le i \le k\} \tag{3.4}$$

$$\mathbf{C} = \{C[i,j],\, 1 \le i,j \le k\} = \{\frac{1}{N-k} \sum_{h=0}^{N-k} x_{i+h}x_{j+h},\, 1 \le i,j \le k\} \tag{3.5}$$

### 3.2.3 Damage index

After characterising the vibration time series with the PDF, a damage index (DI) is defined to indicate the occurrence of damage. It is a measure of the change between the PDFs of the undamaged state and that of a potentially damaged state. The Kullback-Leibler (KL) divergence is a widely used measure of the difference between two PDFs (Kullback, 1997). For the PDF of the vibration time series in a potentially damaged state, denoted as $p_1(\mathbf{x})$, and the PDF of the $m$th vibration time series in the undamaged state, denoted as $p_{0,m}(\mathbf{x})$, the KL divergence between them is defined as (Bishop, 2006)

$$\mathrm{KL}(p_1(\mathbf{x}) \parallel p_{0,m}(\mathbf{x})) = \int p_1(\mathbf{x}) \ln \frac{p_1(\mathbf{x})}{p_{0,m}(\mathbf{x})}\, \mathrm{d}\mathbf{x} \tag{3.6}$$

where $\mathrm{KL}(\cdot \parallel \cdot)$ represents the KL divergence, and $\int(\cdot)\mathrm{d}\mathbf{x}$ is short for $\iint \cdots \int(\cdot)\mathrm{d}x_1\mathrm{d}x_2\cdots\mathrm{d}x_k$. Since the vibration response is a Gaussian process and can be represented by the Gaussian PDF as shown in equation (3.1), both $p_1(\mathbf{x})$ and $p_{0,m}(\mathbf{x})$ are Gaussian. The Gaussianity allows the KL divergence in equation (4.18) to reduce to a closed-form expression (Hershey and Olsen, 2007),

$$\mathrm{KL}(p_1(\mathbf{x}) \parallel p_{0,m}(\mathbf{x})) = \frac{1}{2}(\mathrm{tr}\left(\mathbf{C}_{0,m}^{-1}\mathbf{C}_1\right) - k + \ln \frac{|\mathbf{C}_{0,m}|}{|\mathbf{C}_1|} + (\boldsymbol{\mu}_1 - \boldsymbol{\mu}_{0,m})\mathbf{C}_{0,m}^{-1}(\boldsymbol{\mu}_1 - \boldsymbol{\mu}_{0,m})^{\mathsf{T}}) \tag{3.7}$$

where $\mathrm{tr}(\cdot)$ represents the trace of the matrix, $\boldsymbol{\mu}_1$ and $\boldsymbol{\mu}_{0,m}$ are the means of $p_1(\mathbf{x})$ and $p_{0,m}(\mathbf{x})$, respectively, and $\mathbf{C}_1$ and $\mathbf{C}_{0,m}$ are the covariance matrices of $p_1(\mathbf{x})$ and $p_{0,m}(\mathbf{x})$, respectively.

Suppose there are $n_r$ vibration time series of the undamaged state and one vibration time series of the potentially damaged state. The DI of the proposed method, denoted as $\mathrm{DI}_{\mathrm{PDF}}$, is defined as the averaged KL divergence

$$\mathrm{DI}_{\mathrm{PDF}} = \frac{1}{n_r} \sum_{m=1}^{n_r} \mathrm{KL}(p_1(\mathbf{x}) \parallel p_{0,m}(\mathbf{x})) \tag{3.8}$$

Substituting equation (3.7) into equation (4.20), $\mathrm{DI}_{\mathrm{PDF}}$ is obtained as,

$$\mathrm{DI}_{\mathrm{PDF}} = \frac{1}{2n_r} \sum_{m=1}^{n_r} (\mathrm{tr}\left(\mathbf{C}_{0,m}^{-1}\mathbf{C}_1\right) - k + \ln\frac{|\mathbf{C}_{0,m}|}{|\mathbf{C}_1|} + (\boldsymbol{\mu}_1 - \boldsymbol{\mu}_{0,m})\mathbf{C}_{0,m}^{-1}(\boldsymbol{\mu}_1 - \boldsymbol{\mu}_{0,m})^{\mathsf{T}}) \tag{3.9}$$

where $\boldsymbol{\mu}_{0,m}$, $\boldsymbol{\mu}_1$, $\mathbf{C}_{0,m}$, and $\mathbf{C}_1$ can be estimated by equation (3.4) and (3.5).

### 3.2.4 Damage detection threshold

To discriminate the DIs from the undamaged state and those from a damaged state, a threshold needs to be determined. A simple way to choose the threshold is to assume the DIs of the undamaged state are normally distributed (Farrar and Worden, 2012; Yan et al., 2005a; Bao et al., 2013a). However, considering that the number of available time series and hence the number of DIs of the undamaged state may be limited, it is more appropriate to use the $t$-distribution. Suppose there are $n_{\mathrm{DI}}$ DIs of the undamaged state. The sample mean and the sample standard deviation of these DIs are denoted as $\mu_{\mathrm{DI}}$ and $\sigma_{\mathrm{DI}}$ respectively. The threshold is defined as the upper one-sided 95% confidence limit of the $t$ distribution with $(n_{\mathrm{DI}} - 1)$ degrees of freedom, and it is expressed as,

$$\xi = \mu_{\mathrm{DI}} + \frac{\sigma_{\mathrm{DI}}}{\sqrt{n_{\mathrm{DI}}}} t_{(1-95\%)}(n_{\mathrm{DI}} - 1) \tag{3.10}$$

Overall, the flowchart of the proposed method, referred to as PDF-based method, is shown in Figure 3.1.

## 3.3 Discussion on the proposed method

### 3.3.1 Relation to autocorrelation function and power spectral density

The autocorrelation function (ACF) of the stochastic process, $\{X(t_i), i = 1, 2, \cdots, N\}$, is defined as,

$$R(j-i) = \mathbb{E}[X(t_i)X(t_j)] \tag{3.11}$$

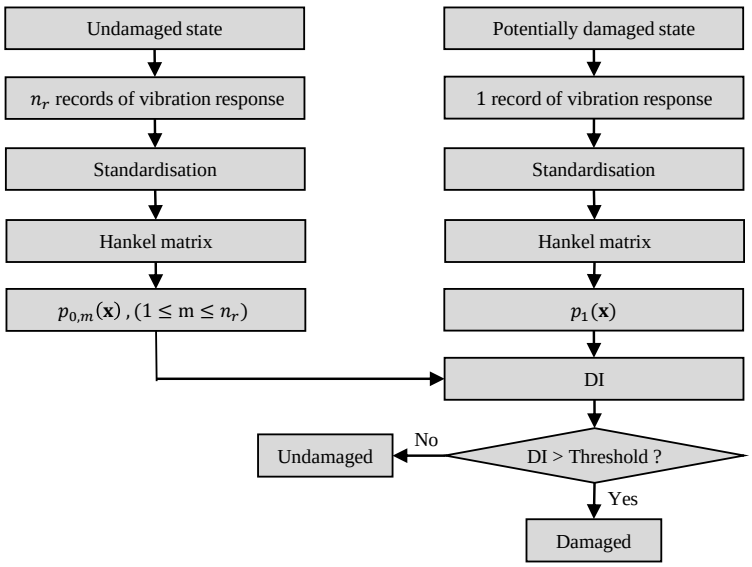


Figure 3.1: Flowchart of the proposed PDF-based method.

where $R(\cdot)$ is the ACF, and $\mathbb{E}[\cdot]$ represents expectation. Observing the entry $C(i,j)$ of $\mathbf{C}$ in equation (3.5), it is obtained

$$\mathbb{E}[X(t_i)X(t_j)] \approx C(i,j) \tag{3.12}$$

Substituting equation (3.12) into equation (3.11),

$$\mathbf{C} \approx \begin{bmatrix} R(0) & R(1) & \cdots & R(k-1) \\ & R(0) & \cdots & R(k-2) \\ & & \ddots & \vdots \\ \text{Symmetric} & & & R(0) \end{bmatrix} \tag{3.13}$$

This shows the ACF values at different lags form the covariance matrix $\mathbf{C}$. In other words, the ACF is closely related to the covariance matrix. Since the covariance matrix contains the main information of the PDF shown in equation (3.1), the ACF is further related to the PDF. In addition, $\mathrm{DI}_{\mathrm{PDF}}$ described in equation (3.9) has clearly shown its relationship with the covariance matrix, therefore $\mathrm{DI}_{\mathrm{PDF}}$ is also related to the ACF. Overall, the ACF is related to the PDF and $\mathrm{DI}_{\mathrm{PDF}}$. Furthermore, since the ACF is related to the power spectral density (PSD) by the celebrated Wiener-Khintchine formula (Li and Chen, 2009), the PDF and $\mathrm{DI}_{\mathrm{PDF}}$ are also linked to the PSD.

### 3.3.2 Effect of noise

In real vibration measurements, noise is inevitable. The measured response can be viewed as a superposition of theoretical response and noise (Roveri and Carcaterra, 2012; Bao et al., 2013a). That is,

$$x = x^* + v = x^* + \mathrm{RMS}\left(x^*\right) \cdot W_{\mathrm{unit}} \cdot N_{\mathrm{level}} \tag{3.14}$$

where $x$ denotes the acceleration with noise, $v$ is the noise, $x^*$ stands for the acceleration without noise, RMS($x^*$) is the root-mean-square value of $x^*$, $N_{\mathrm{level}}$ is the noise level, and $W_{\mathrm{unit}}$ is the randomly generated Gaussian noise with zero mean and unit standard deviation.

Suppose that the stochastic process of the theoretical response, $\{X^*(t_i), i = 1,2,\cdots,N\}$, and the stochastic process of the noise, $\{\Upsilon(t_i), i = 1,2,\cdots,N\}$, are independent. According to equation (3.14), the stochastic process of the measured response, $\{X(t_i), i = 1,2,\cdots,N\}$, can be expressed as:

$$X(t_i) = X^*(t_i) + \Upsilon(t_i) \quad for\ 1 \le i \le N \tag{3.15}$$

The ACF of the stochastic process $\{X(t_i), i = 1,2,\cdots,N\}$ with lag $l$ can be expressed as (Bao et al., 2009; Hui et al., 2017):

$$\begin{aligned} R(l) &= \mathbb{E}[X(t_i)X(t_{i+l})] \\ &= \mathbb{E}[X^*(t_i) + \Upsilon(t_i)][X^*(t_{i+l}) + \Upsilon(t_{i+l})] \\ &= \mathbb{E}[X^*(t_i)X^*(t_{i+l})] + \mathbb{E}[X^*(t_i)\Upsilon(t_{i+l})] \\ &\quad + \mathbb{E}[X^*(t_{i+l})\Upsilon(t_i)] + \mathbb{E}[\Upsilon(t_i)\Upsilon(t_{i+l})] \\ &= \mathbb{E}[X^*(t_i)X^*(t_{i+l})] + \sigma^2\delta(l) \end{aligned} \tag{3.16}$$

where $1 \le i \le (N-l)$, $\sigma$ is the standard deviation of $\Upsilon(t_i)$ for any possible $i$, and $\delta(\cdot)$ is the Dirac delta function. Therefore,

$$\begin{aligned} R(l) &= \mathbb{E}[X^*(t_i)X^*(t_i)] + \sigma^2 \quad for\ l = 0 \\ R(l) &= \mathbb{E}[X^*(t_i)X^*(t_{i+l})] \quad for\ l \ne 0 \end{aligned} \tag{3.17}$$

Hence, for $l \ne 0$, theoretically, the noise effect on the ACF cancels out. This means all the non-diagonal entries in the autocovariance matrix $\mathbf{C}$, as shown in equation (3.13), are not affected by the noise. Although the noise effect on $R(0)$ remains, this only affects the diagonal entries of $\mathbf{C}$. Since the proposed method relies on the $\mathbf{C}$, the effect of noise may be alleviated significantly.

## 3.4 Numerical simulation of a monopile offshore wind turbine

This section introduces the numerical simulation of an offshore wind turbine (OWT), which is used to demonstrate the method. The OWT consists of the National Renewable Energy Laboratory (NREL) 5MW baseline wind turbine (Jonkman et al., 2009) installed on a monopile foundation. The NREL 5MW baseline wind turbine is a conventional three-bladed upwind variable-speed variable-pitch turbine. The monopile profile used in this case study was taken from Jonkman et al. (2008a). An overview of the structural dimensions is given in Figure 3.2, with more specifications summarised in Table 3.1.

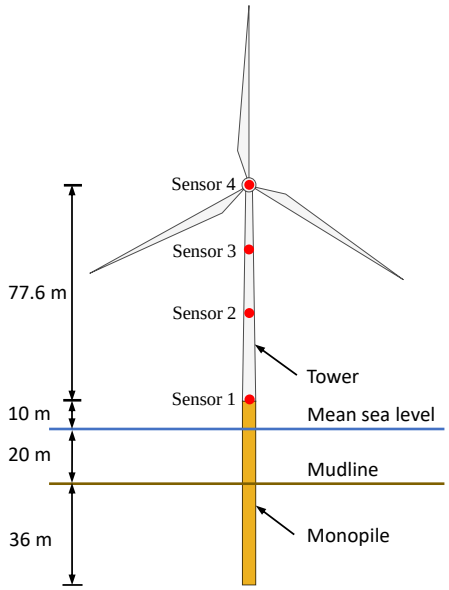


Figure 3.2: OWT and locations of the virtual sensors

### 3.4.1 Simulation

The OWT was simulated in DNV's Bladed software (DNV, 2020), which is an integrated wind turbine design tool for calculating turbine performance and dynamic loading and response. For dynamic analysis, it is common to use finite element representations and modal analysis. In principle, the standard finite element method only considers structures in which the deflection occurs about an initial reference position. However, wind turbines

Table 3.1: Main properties of the tower and the monopile (Jonkman et al., 2009, 2008a)

| Property | Value |
|---|---|
| Tower top diameter, wall thickness | 3.87 m, 0.019 m |
| Tower base diameter, wall thickness | 6.00 m, 0.027 m |
| Foundation diameter, wall thickness | 6.00 m, 0.060 m |
| Density | 8500 kg/m$^3$ |
| Young's modulus | 210 GPa |
| Shear modulus | 80.8 GPa |
| Damping ratio (all modes) | 1% |

consist of rigid components (e.g. yaw bearings) which present rigid body motions with respect to other flexible components (e.g. towers, blades, and foundations). This requires the finite element models to be tailored for wind turbines, leading to the multi-body dynamic approach. In this approach, flexible components are modelled by Timoshenko beam elements, and their motions are modelled by rigid body motions combined with relative motions due to the deformation. Since monopiles are axisymmetric, the beam elements are two-dimensional. It is worth noting that the monopile below the mudline is modelled differently. This part of the monopile is subject to complicated soil-pile-interaction; to reduce computational burden, it is typically modelled by coupled springs (Jonkman et al., 2008a). That means the monopile under the mudline is idealised as a stiffness matrix positioned at the mudline. The stiffness matrix was given by (Passon, 2006) as:

$$\mathbf{K}_{\text{mudline}} = \begin{bmatrix} k_{xx} & 0 & 0 & k_{x\beta} \\ & k_{yy} & k_{y\alpha} & 0 \\ & & k_{\alpha\alpha} & 0 \\ \text{Symmetric} & & & k_{\beta\beta} \end{bmatrix} \tag{3.18}$$

where the horizontal stiffness coefficients $k_{xx} = k_{yy} = 2.57 \times 10^9$ N/m, the rotational stiffness coefficients $k_{\alpha\alpha} = k_{\beta\beta} = 2.63 \times 10^{11}$ N·m/rad, and the coupled stiffness coefficients $k_{x\beta} = -k_{y\alpha} = -2.25 \times 10^{10}$ N/rad. It is meaningful to show the finite element representation of the support structure, which is the focus of this study. The finite element representation is shown in Figure 3.3, where the numbers are the element indices. The tower (also see Figure 3.2) is divided evenly into 10 elements (from Element 1 to Element 10), corresponding to an element size of 7.76 m, as used in the benchmark model in Jonkman et al. (2009). The element size for the monopile above the mudline is 10 m, as shown by Element 11, Element 12 and Element 13. The nacelle and rotor are modelled

as lumped masses located at the nacelle centre of gravity and rotor hub, respectively (DNV-GL, 2016); The lumped masses are linked with a rigid element. This finite element representation is used for the calculation of the support structure modes.

As an initial study, some simplifications were made for the OWT. First, the wind turbine was set as parked (the rotor was in a standstill condition). Also, the blades are rigid for the purposes of the overall coupled dynamic analysis. Furthermore, the loading was assumed to be Gaussian white noise and applied as a point load to the tower top along the nacelle (i.e., fore-aft direction). The Gaussian white noise was generated by Matlab function *wgn()* with a sampling frequency of 20 Hz, corresponding to a flat spectrum with a frequency range from 0 to 10 Hz. The frequency was limited to 10 Hz since normally only the first few vibration modes are excited significantly. This frequency range covers the first 5 modes of the example wind turbine. The amplitude of the loading was arbitrary since the system was linear, and the method did not consider the amplitudes of the responses. No additional wind or wave forces were considered.

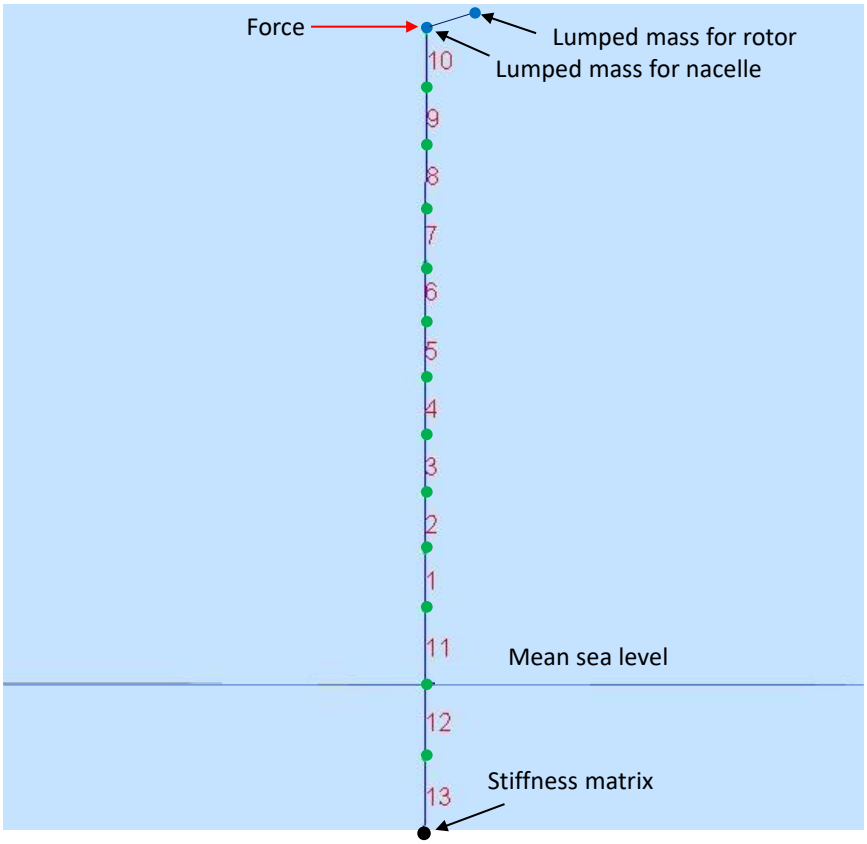


Figure 3.3: Finite element representation of the support structure in Bladed.

### 3.4.2 Damage levels and noise levels

OWTs' foundations can be affected by scour, that is, erosion of the mudline near the foundation. In the particular case of monopile foundations, scouring can reduce the first natural frequency of the support structure by 5% – 10% (Devriendt et al., 2014; Prendergast et al., 2015). In this chapter, the damage caused by scouring was simulated by reducing $\mathbf{K}_{\text{mudline}}$. Two different damage levels were studied, with 2% and 4% reduction of all entries of $\mathbf{K}_{\text{mudline}}$, respectively. They result in 0.68% and 0.81% reduction of the first natural frequency respectively.

The output of the Bladed simulation is a theoretical result without noise. Noise was added to the Bladed output to obtain the measured response as expressed in equation (3.14). Three noise levels were considered: $N_{level} = 15\%$, $N_{level} = 30\%$ and $N_{level} = 45\%$, corresponding to 16.5 dB, 10.5 dB and 6.95 dB signal-to-noise ratio, respectively. For consistency, the state without noise is also denoted as $N_{level} = 0\%$.

### 3.4.3 Sensors and Accelerations

In this study, only one accelerometer was used at a time for analysis, for simplicity of the monitoring system, but four sensor locations were considered to evaluate the most appropriate single location to use. They were assumed to be located at each internal tower platform, as depicted in Figure 5.3, for ease of access for installation and maintenance. The distances from the accelerometers to the mudline are 30.0 m, 61.0 m, 84.3 m, and 107.6 m, respectively.

The accelerations in the fore-aft direction were obtained from Bladed from the virtual accelerometers for further analysis, with a sampling frequency of 20 Hz and a length of 20 minutes for each record. Typical acceleration time series without noise from Sensor 1 are plotted in Figure 3.4. Figure 3.4 (a) shows a typical 20-minute acceleration record for the undamaged state; Figure 3.4 (b) presents a similar record under the excitation of the same magnitude but different time series for the damaged state with 4% stiffness reduction; Figure 3.4 (c,d) show zoomed views of typical 10 s corresponding to Figure 3.4 (a,b), respectively. For further understanding of the signals and to show the challenges of detecting the damage, Figure 3.5 shows the Welch PSDs estimated from the noise-free acceleration time series from Sensor 1 in the undamaged state and the damaged state with 4% stiffness reduction. For each state, 25 PSDs were estimated (via Matlab function $pwelch$) from different 20-minute time series (each time series is 24000 samples long), using a Hamming window of 1024 samples and 50% overlap. The middle curves in Figure

3.5 are the mean of the PSDs, and the boundary lines represent plus and minus three standard deviations of the PSDs. It can be seen that it is challenging to differentiate between the undamaged state and the damaged state.

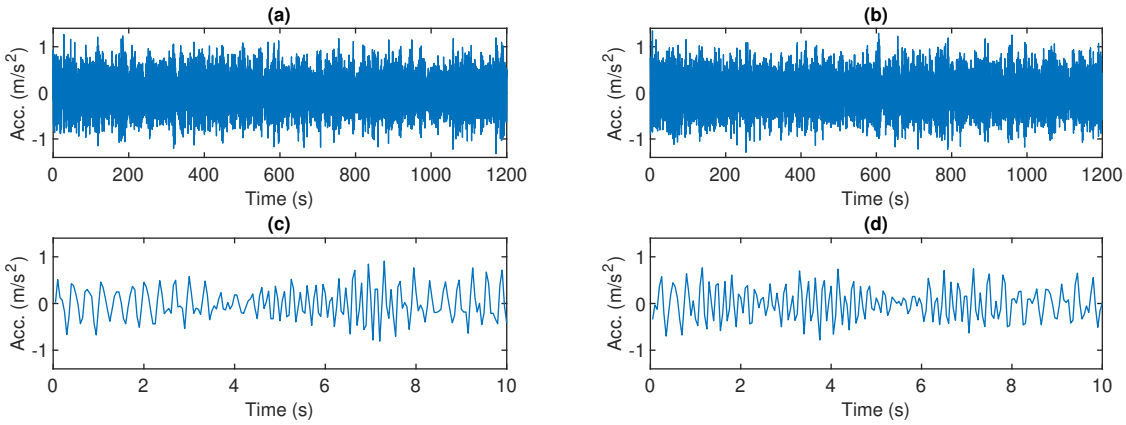


Figure 3.4: Typical acceleration time series from Sensor 1. (a) shows a 1200 s acceleration record without noise in the undamaged state; (b) presents a similar record for the 4% damaged state; (c,d) are zoomed views of typical 10 s corresponding to (a,b), respectively.

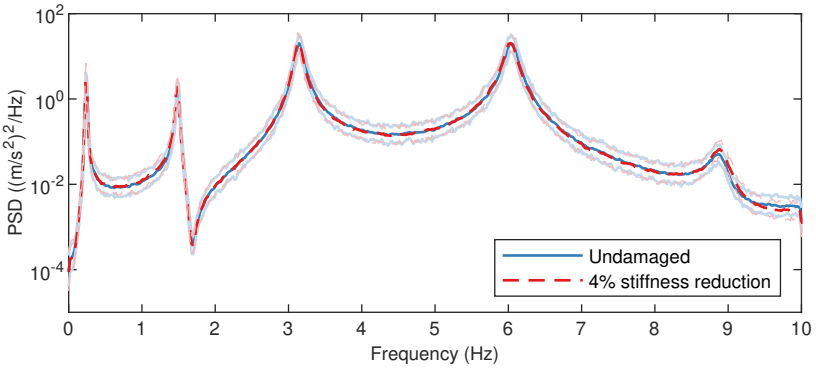


Figure 3.5: Welch PSDs for Sensor 1 for the undamaged state and 4% damaged state. For each state the middle line represents the average and the upper and lower lines show plus and minus three standard deviations.

Based on the built-in modal analysis in Bladed, the first five fore-aft modes can be identified, as shown in Table 3.2. It should be noted that these modes are coupled modes of the rigid blades, rotor and support structure. The coupled mode shapes are not available directly in Bladed, but Bladed provides the descriptions of these modes, indicating the contributions of uncoupled modes. Based on these descriptions, the dominant uncoupled mode of each coupled mode is selected and summarised in Table 3.2. It can be seen that the tower modes are the dominant contributors to the coupled modes. Therefore, the

coupled modes can be roughly represented by the tower modes (For the calculation of the tower modes, nacelle and rotor are modelled as lumped mass at tower top), which are shown in Figure 3.6. The red points represent sensors. The figure shows that Sensor 1, Sensor 2 and Sensor 3 are away from the points where the mode shapes are zeros. However, Sensor 4 is at the points where the mode shapes are zeros for all the modes except the first one, indicating its location may not be suitable for damage detection.

Table 3.2: Mode shape descriptions

| Coupled mode | Natural frequencies (Hz) | Dominant uncoupled mode |
|---|---|---|
| 1st | 0.2473 | Tower first fore-aft mode |
| 2nd | 1.5115 | Tower third fore-aft mode |
| 3rd | 3.1572 | Tower third fore-aft mode |
| 4th | 6.0531 | Tower fourth side-side mode |
| 5th | 9.2063 | Tower first vertical mode |

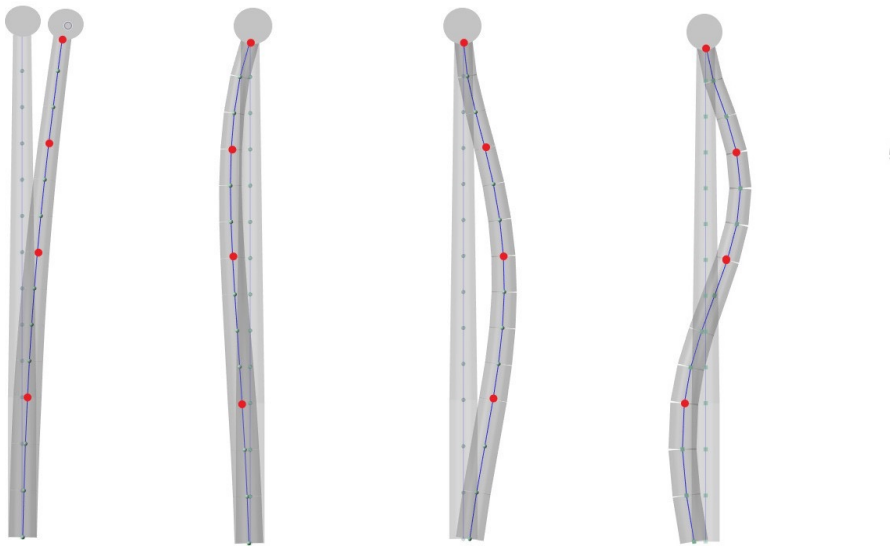

Figure 3.6: Uncoupled tower mode shapes. The first, second, third, and fourth fore-aft mode shapes are shown from left to right respectively. The red points represent Sensor 1, Sensor 2, Sensor 3, Sensor 4, from bottom to top.

## 3.5 Results and comparative studies

The damage detection results of the proposed method and the comparisons with other methods are presented in this section. First, the dimensionality of the multivariate PDF is tuned to ensure the PDF-based method achieves the best performance. Damage detection results of the PDF-based method are then presented. Finally, an AR-based method and an ACF-based method are evaluated and compared with the PDF-based method.

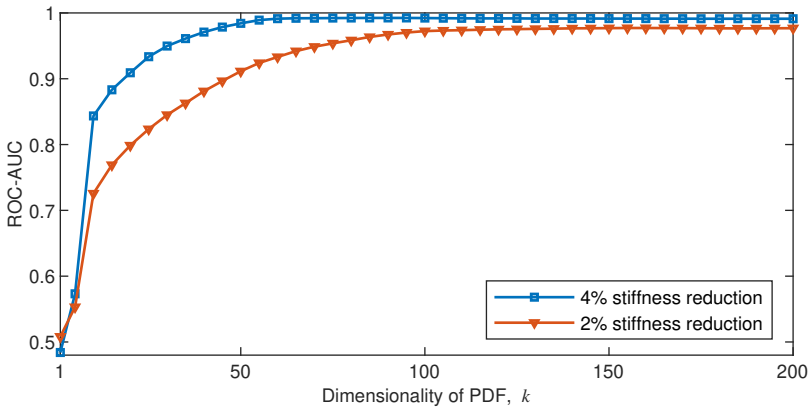


Figure 3.7: ROC-AUC obtained for increasing PDF dimensionality $k$.

### 3.5.1 Dimensionality of the probability density function

The dimensionality of the PDF, $k$, was tuned to yield the best model performance, which was measured by a receiver operating characteristics (ROC) curve (Fawcett, 2006). The ROC curve plots the true positive rate against the false positive rate of damage detection at various threshold values. The area under the ROC curve, referred to as ROC-AUC, represents the degree of separability between the DIs of the undamaged state and those of a potentially damaged state. If the value of ROC-AUC is 1, the DIs of the potentially damaged state are perfectly separated from those of the undamaged state. If the ROC-AUC is 0.5, the detection is by chance only.

In this chapter, the dataset used to obtain each ROC-AUC included 25 reference time series of the undamaged state (i.e., $n_r = 25$ in equation (4.20)) and 200 testing time series (100 of the testing time series were from the undamaged state, and the other 100 were from a damaged state). Accordingly, 200 DIs were calculated. Then, the ROC-AUC value was obtained based on these DIs.

In the study of dimensionality $k$, all time series were from Sensor 1 and without noise. By increasing $k$ from 1 to 200 ($k = 1, 5, 10, 15, \cdots, 200$), the corresponding ROC-AUC values for different damage levels (2% and 4% stiffness reduction) were obtained and plotted in Figure 3.7. Both lines in Figure 3.7 have shown similar phenomena. At the starting point where $k = 1$, the ROC-AUC values are around 0.5. This suggests that merely comparing the univariate PDFs, as in Figueiredo et al. (2009), is inefficient for detecting linear damage and the correlation information should be exploited. As $k$ increases, the ROC-AUC values become larger, reaching plateaus for $k > 100$. Ultimately, the selected dimensionality was $k = 150$. This dimensionality allows the PDF sample to cover a period of 7.50 s, i.e., 1.83 times the fundamental natural period. Although the data from damaged states were used in this case study, it should be noted that these data are normally unavailable in practice. Therefore, it is desirable to determine the PDF dimensionality without the data from damaged states. As discussed in Section 3.3.1, the PDF dimensionality is related to the lags of ACF and eventually the PSD, hence it is natural to try to relate the PDF dimensionality to the fundamental natural period. Once the relationship is known, even empirically, the PDF dimensionality can be determined based on the fundamental natural period, which is normally easy to approximate. This approach is valuable in practice when the data from damage states are unavailable.

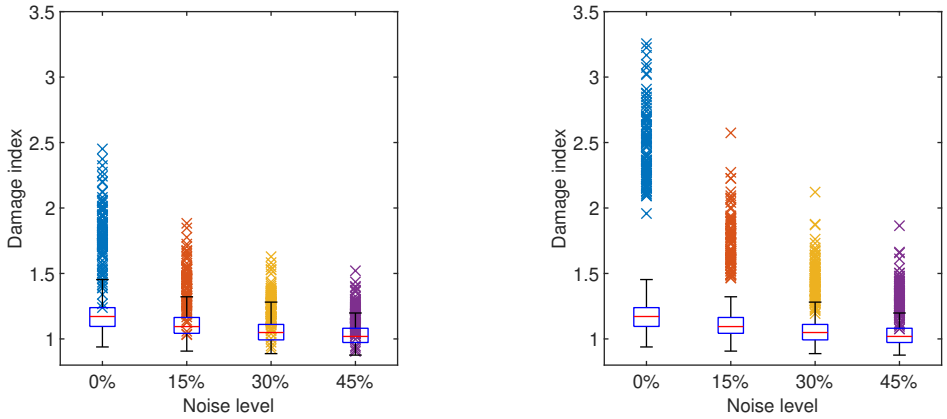


Figure 3.8: Distributions of the DIs for Sensor 1 for different noise levels by the PDF-based method: (a) for the state with 2% stiffness reduction and (b) for the state with 4% stiffness reduction. The box plot is generated by the DIs from the undamaged state; the central line indicates the median, the bottom and top edges of the box represent the 25th and 75th percentiles, and the extended bars show the most extreme data points. The crosses denote the DIs from the damaged state.

### 3.5.2 Damage detection results

With the selected dimensionality, the performance of the PDF-based method for different damage levels, noise levels, and sensors is now presented. Again, each ROC-AUC value is based on 200 DIs, which are obtained from 25 reference time series and 200 testing time series (100 of the testing time series are from the undamaged state, and the other 100 are from a damaged state). But the data used here are different from the data used for the parameter selection. As an example of the results, the DIs of Sensor 1 are shown in Figure 3.8. In this figure, the box plot is generated by the DIs from the undamaged state, while the distributed crosses represent the DIs from the damaged state. The less overlap between the box and the crosses, the more easily the damaged state can be separated from the undamaged state, and a better damage detection performance can be achieved.

The following findings can be drawn from Figure 3.8. In Figure 3.8 (a), the amount of overlap between the DIs for the damaged and undamaged states increases as the noise level increases. This implies that the performance has a trend to decrease as the noise level increases, as may be expected. This can also be seen in Figure 3.8 (b). When comparing Figure 3.8 (a) and Figure 3.8 (b), for each noise level, the overlap for the damaged state with 4% stiffness reduction is much smaller than that for the damaged state with 2% stiffness reduction. This indicates that the performance becomes better when the structure is more severely damaged. Furthermore, the crosses for the damaged state with 4% stiffness reduction are generally higher than those for the damaged state with 2% stiffness reduction. This demonstrates that the DIs increase when the structure is more severely damaged.

Table 3.3: Probability of detection by the PDF-based method.

| Damage level | Noise level | Probability of detection (%) | | | |
|---|---|---|---|---|---|
| | | Sensor 1 | Sensor 2 | Sensor 3 | Sensor 4 |
| 2% | 0% | 91 | 91 | 72 | 11 |
| | 15% | 63 | 61 | 68 | 11 |
| | 30% | 40 | 50 | 68 | 11 |
| | 45% | 36 | 45 | 56 | 13 |
| 4% | 0% | 100 | 100 | 100 | 12 |
| | 15% | 100 | 99 | 100 | 11 |
| | 30% | 92 | 98 | 99 | 11 |
| | 45% | 84 | 91 | 95 | 13 |

#### 3.5.2.1 Probability of detection

Probability of detection is a commonly used measure of the performance of a damage detection method (Straub, 2004). It is defined as the probability that a damaged state is correctly identified as damaged, and is equivalent to the true positive rate for the ROC curve. Given a threshold, the time series with a DI larger than the threshold is classified to be from a damaged state. The ratio between the number of these time series and the number of the time series from the real damaged state is the probability of detection. The results of the probability of detection are summarised in Table 3.3, which support the findings for Figure 3.8. It can be seen that the values of probability of detection for Sensor 4 are extremely small, implying the acceleration at Sensor 4 is insensitive to the change of the structural properties. This can be explained by observing the mode shapes in Figure 3.6 and the PSDs in Figure 3.5. Specifically, in Figure 3.6, the mode shapes at Sensor 4 are around zero for all the modes except the first one. By further observing Figure 3.5, it can be seen that the third and forth modes (rather than the first mode) dominate the acceleration components in the frequency domain. Hence it is reasonable to expect that Sensor 4 is insensitive to the change of the structural properties and, consequently, the change the damage.

#### 3.5.2.2 ROC-AUC

Although the probability of detection is intuitive in engineering, it relies on a pre-determined threshold, which is chosen by the user depending on the relative importance to them of the true and false positive rates in a real-world project. In contrast, ROC-AUC summarises the performance of all possible thresholds and provides an overall measure of the performance of the method. In other words, ROC-AUC measures the capability of a method to distinguish between two states, without relying on the threshold. This makes ROC-AUC especially useful for the comparison of methods, which is shown in the next section, when the threshold is not yet defined. Therefore, the performance is further quantified using the ROC-AUC values based on the DIs. As an example, the ROC curves of Sensor 1 are illustrated in Figure 3.9, which supports the findings already discussed for Figure 3.8. The ROC-AUC values of all sensors are summarised in Table 3.4, where the results of two other methods are also shown and will be discussed subsequently. Similar to the results of probability of detection in Table 3.3, the ROC-AUC values of Sensor 4 are around 0.5 across all the three methods, indicating Sensor 4 is insensitive to the damage. This is expected as ROC-AUC is just another performance measure of

the damage detection method. The reason is the same as that in Section 3.5.2.1.

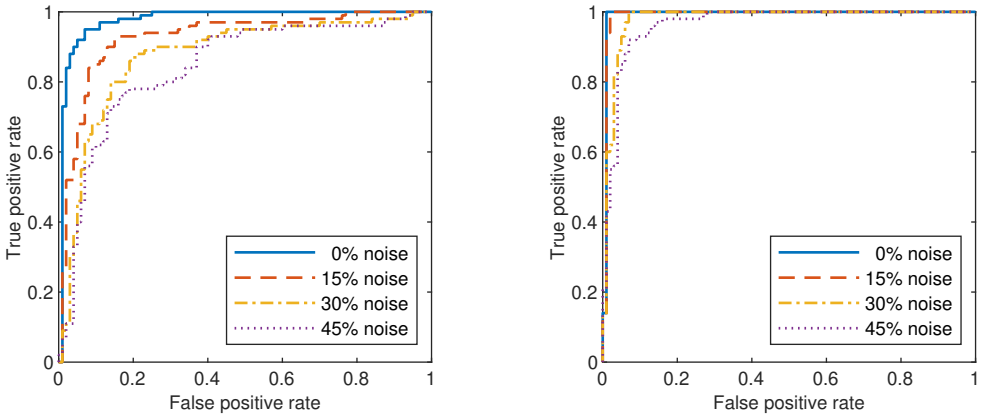


(a) (b)

Figure 3.9: ROC curves for Sensor 1 for (a) the state with 2% stiffness reduction and (b) the state with 4% stiffness reduction at different noise levels by the PDF-based method.

Table 3.4: Comparison results for PDF-based, AR-based and ACF-based methods. For each method, the largest ROC-AUC in all sensors is emphasised in bold.

| Method | Sensor | ROC-AUC | | | | | | | |
|---|---|---|---|---|---|---|---|---|---|
| | | Damage level | | | | | | | |
| | | 2% | | | | 4% | | | |
| | | Noise level | | | | Noise level | | | |
| | | 0% | 15% | 30% | 45% | 0% | 15% | 30% | 45% |
| PDF-based | 1 | 0.977 | 0.927 | 0.875 | 0.842 | 0.991 | 0.991 | 0.980 | 0.966 |
| | 2 | **0.978** | **0.940** | 0.896 | 0.844 | 0.998 | 0.993 | 0.988 | 0.978 |
| | 3 | 0.964 | 0.933 | **0.904** | **0.873** | **1.000** | **0.998** | **0.991** | **0.981** |
| | 4 | 0.574 | 0.581 | 0.592 | 0.604 | 0.647 | 0.653 | 0.663 | 0.674 |
| AR-based | 1 | **0.980** | 0.820 | 0.691 | 0.635 | **1.000** | 0.933 | 0.787 | 0.708 |
| | 2 | 0.881 | 0.838 | **0.789** | 0.723 | 0.988 | 0.949 | 0.898 | 0.826 |
| | 3 | 0.887 | **0.847** | 0.789 | **0.740** | 0.983 | **0.967** | **0.920** | **0.874** |
| | 4 | 0.659 | 0.634 | 0.580 | 0.539 | 0.713 | 0.715 | 0.669 | 0.639 |
| ACF-based | 1 | **0.874** | **0.873** | 0.870 | **0.879** | **0.973** | **0.973** | **0.971** | **0.969** |
| | 2 | 0.870 | 0.873 | **0.874** | 0.873 | 0.960 | 0.960 | 0.961 | 0.955 |
| | 3 | 0.847 | 0.844 | 0.846 | 0.850 | 0.959 | 0.958 | 0.960 | 0.946 |
| | 4 | 0.537 | 0.538 | 0.540 | 0.543 | 0.571 | 0.571 | 0.570 | 0.567 |

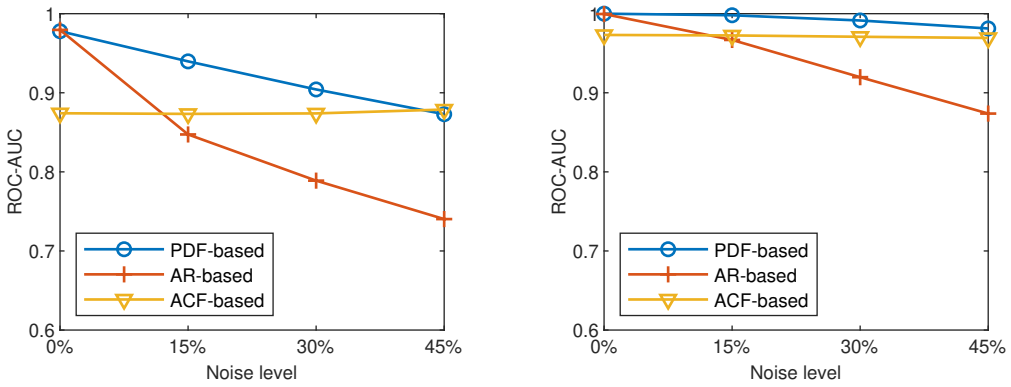


Figure 3.10: Comparison of the maximum ROC-AUCs in all sensors for (a) the state with 2% stiffness reduction and (b) the state with 4% stiffness reduction for different methods at different noise levels.

### 3.5.3 Comparative study

The performance of the proposed PDF-based method is compared with that of an AR-based method and an ACF-based method. The AR-based method is selected because it is widely used for VBDD (Spanos et al., 2020; Yao and Pakzad, 2012; Nair et al., 2006; Bao et al., 2013a). The ACF-based method is chosen because it is closely related to the proposed PDF-based method. The two methods are briefly summarised in Appendix A.1 and A.2, respectively.

To make a fair comparison, the model parameters of both the AR-based method and the ACF-based method were optimised by maximising the ROC-AUC. ROC-AUC values were calculated for each method, damage level, noise level, and sensor. The results are summarised in Table 3.4. For each method, the largest ROC-AUC in a column is emphasised in bold. To facilitate the comparison of the different methods, the results in bold are plotted in Figure 3.10, distributed per damage level and noise level.

Compared with the AR-based method, the PDF-based method has better performance, especially for the higher noise levels. Similarly, the PDF-based method is superior to the ACF-based method in all cases except for the case of 2% stiffness reduction and 45% noise level, although these two methods are closely related. The superiority of the PDF-based method may be attributed to the application of the multivariate PDF and the KL divergence. Regarding the effect of noise, both the ACF-based method and the PDF-based method are less sensitive to the noise than the AR-based method. This can be explained by the reason stated in Section 3.3.2. Specifically, if the theoretical response (i.e., the signal without noise) and the noise (assumed to be Gaussian white noise) is

independent, the ACF values of the signal is not affected by noise except the ACF value at lag zero. This explains why the ACF-based method is less sensitive to the noise than the AR-based method. Similarly, the covariance matrix of the same signal is free of the noise effects except matrix entries at the diagonal (corresponding to the ACF values at lag zero); hence the proposed PDF-based method that relies on the covariance matrix becomes less sensitive to the noise than AR-based method.

## 3.6 Conclusion

This chapter has presented the multivariate PDF as a novel feature for VBDD, with the KL divergence between the PDF of the undamaged state and that of a potentially damaged state used as the damage index. The effectiveness and advantages of the proposed method have been demonstrated on a simplified offshore wind turbine. The proposed PDF-based method shows significant performance improvements over an ACF-based method and an AR-based method.

Although the proposed method has shown its superiority, it is worth noting that the study in this chapter has assumed a linear system under Gaussian white noise. Accordingly, the offshore wind turbine in the case study is largely simplified, while in the real world these structures are complex systems that may be nonlinear and subjected to environmental and operational variations. In addition, the proposed method only considers signals from one sensor, which is useful for structures with limited sensors, but enhanced methods for multiple sensors are also valuable as they may improve damage detection performance and allow damage localisation.

Nevertheless, this work has shown a new approach for VBDD; this is comparing the multivariate PDFs of the underlying stochastic processes of vibration signals. Following this approach, more complex structures may be tackled with more sophisticated statistical methods. For example, damage detection for nonlinear structures can be dealt with using non-parametric PDF estimation methods.

*This page intentionally left blank*.

CHAPTER 4

# Damage Detection of Nonlinear Structures Using Probability Density Ratio Estimation

The previous chapter studied a linear structure under Gaussian white noise. It demonstrated that the vibration signals can be characterised by Gaussian PDFs and the damage index has a closed-form solution. However, structures may be nonlinear, resulting in non-Gaussian PDFs of the vibration responses. For damage detection, the PDFs have to be estimated, which is very difficult to achieve accurately. This issue becomes more challenging if the structure is nonlinear both before and after damage. As a solution, this chapter extends the method in the previous chapter by introducing density ratio estimation for damage index calculation.

---

This chapter is adapted from the manuscript:

Zhang Y., Macdonald J.H.G., Liu S., Harper P. (in press). Damage detection of nonlinear structures using probability density ratio estimation. Computer-Aided Civil and Infrastructure Engineering.

Part of the introduction has been removed and included in Chapter 2 - Literature Review.

## Authors' contributions

Zhang Y. conceived the idea, performed the numerical simulations, and implemented the method, with supervisory support from Macdonald J.H.G. on the development of the idea and discussion of the results, and input from Liu S. on the density ratio estimation method. All authors contributed to the preparation of the manuscript.

## 4.1 Introduction

Structural systems play a crucial role in modern societies. It is important to monitor the health state of these structures to avoid unexpected life and economic losses, especially when they are approaching the end of their design life. As an example, offshore wind turbines (OWTs), which provide a promising renewable energy source, have had rapid growth in the last two decades (Lee and Zhao, 2021). Considering typical OWTs have a 20-year design lifetime, the first generation of OWTs has come to the end of its design life. This motivates the research of structural health monitoring (SHM), which automatically detects, identifies, and estimates damage in infrastructure. Within the SHM research community, vibration-based damage detection has gained widespread interest for several reasons, such as its 'global' coverage (compared with other 'local' methods like acoustic emission and ultrasound), its ability to be automated, and mature and reasonably low-cost signal measurement and acquisition technology (Fassois and Sakellariou, 2007).

Numerous vibration-based damage detection methods have been proposed. The most common and historically important class of methods is modal parameter-based methods, which apply both basic modal properties (e.g., modal frequencies, modal damping, and mode shapes) and their derivations (e.g., mode shape curvature, modal strain energy, and modal flexibility). Apart from the modal parameters, mass, stiffness, and damping matrices have also been used, corresponding to finite element model updating methods. A detailed review of these two classes of methods has been reported by Doebling et al. (1998). Another important category is time series methods, which do not rely on physical or finite element models and can inherently account for uncertainty (Fassois and Sakellariou, 2007). These methods are usually based on an autoregressive/autoregressive with exogenous input/ autoregressive with moving average model; then, the model coefficients or the residual errors are used as features (Yao and Pakzad, 2012; Figueiredo et al., 2011a). In addition, signal processing techniques, such as wavelet transformation, Hilbert–Huang transform, and fractal dimension have been developed to improve damage sensitivity (Huang et al., 2020; Amezquita-Sanchez and Adeli, 2015b; Perez-Ramirez et al., 2016; Amezquita-Sanchez et al., 2017; Amezquita-Sanchez and Adeli, 2015a). More recently, machine learning-based methods have drawn increasing interest, such as artificial neural networks (Adeli and Yeh, 1989; Xu et al., 2012), support vector machines (Ghiasi et al., 2016) and Gaussian process regression (Okazaki et al., 2020). Conventional artificial neural networks rely on shallow nets consisting of only three layers. Due to the improvements in computational power, deep neural networks, with more layers, have

been developed. Most deep neural networks can extract optimised features automatically for the problems at hand (Sajedi and Liang, 2020; Lin et al., 2017). This makes them attractive for vibration-based damage detection. It is worth mentioning a very active research area where deep neural networks are used to examine images for damage detection (Athanasiou et al., 2020; Deng et al., 2020; Guo et al., 2020; Pan and Yang, 2020). Further reviews can be found in (Qarib and Adeli, 2014; Hou and Xia, 2021).

Most existing vibration-based damage detection methods assume that the structure behaves linearly before and after damage. Although nonlinearity has been considered in vibration-based damage detection, its application has normally been limited to the scenario that the system is linear in the undamaged state and becomes nonlinear in the damaged state (Worden et al., 2008). However, many real-world structures will exhibit nonlinear responses in their undamaged state, especially when the vibration amplitudes are large. Vibration-based damage detection problems where the system is initially nonlinear have rarely been studied. In 2010, Bornn et al. (2010) first addressed the issue and applied an autoregressive support vector machine method. However, the method and other alternatives for characterising nonlinearity have been criticised for their lack of generality (Shiki et al., 2017; Villani et al., 2019a). That means it is difficult to obtain a general model that can describe all structures of interest. Therefore, Shiki et al. (2017) proposed to use a Volterra series model, which is a generalisation of the linear convolution representing the linear and nonlinear responses of a dynamical system in a separable way. The Volterra series model has been further studied in relation to uncertainties and experimental data in the last two years (Villani et al., 2019a,b, 2020). However, the Volterra series model relies on input signals, making it impractical for applications on large civil engineering structures, where the input is generally unknown.

Statistics of signals have been used for vibration-based damage detection. The second-order statistics such as variance and autocorrelation are important to stationary, zero-mean, Gaussian stochastic processes since such processes are completely determined by their second-order statistics. However, for a nonlinear system, the stochastic process of the vibration response becomes non-Gaussian, and its higher-order moments become informative. Accordingly, higher-order moments have been proposed for nonlinear damage detection, although their frequency-domain counterparts, such as bispectrum and trispectrum, are often used in practice (White, 2009; Courtney et al., 2010; Rivola and White, 1998; Sinha, 2007). However, these statistics are often used individually, representing partial information of the stochastic process, and may only address one specific damage class. To improve the generality of damage detection methods, it is desirable use

a feature that completely characterise a stochastic process. Therefore, using the multivariate probability density function (PDF) which completely characterises the stochastic process, may be more promising.

PDFs can be estimated by two approaches: parametric methods and non-parametric methods. For systems that are nonlinear before and after damage, the corresponding PDFs are non-Gaussian and unknown. Therefore, non-parametric methods are superior. Non-parametric methods have been used in damage detection, mainly for describing the distribution of features (Worden et al., 2003; Eltouny and Liang, 2021; Liang et al., 2018a). By estimating the PDF of the feature for the undamaged state, damage can be detected by examining if a new value of feature from a potentially damaged state exceeds a pre-defined threshold (Worden et al., 2003; Farrar and Worden, 2012). However, for damage detection, what of interest is the change between the PDF of the undamaged state and the PDF of a potentially damaged state, rather than the PDFs themselves. Optimal model for the PDF of the undamaged state is not necessarily the best choice for PDF change estimation (Sugiyama et al., 2012). Furthermore, non-parametric density estimation is known to be a hard problem (Härdle et al., 2004). Therefore, density ratio estimation methods (Sugiyama et al., 2008), which estimate the PDF change directly, have been proposed. It has been used for respiration and speech monitoring (Kawahara and Sugiyama, 2012). In a previous study of the authors, density ratio estimation method is applied for damage detection and localisation of a linear structure (Zhang et al., 2020).

The main contribution of this study is on proposing a general and output-only method for damage detection of initially nonlinear systems. The method monitors the multivariate PDFs of the vibration response and thus can detect different damages. Furthermore, the method does not rely on specific input signals such as chirp signals in (Shiki et al., 2017; Villani et al., 2019b,a, 2020). Hence, it is more practical for civil engineering structures. To overcome the challenges of PDF estimation, a density ratio estimation method (Sugiyama et al., 2008) is applied to directly estimate the change between the PDF of the undamaged state and the PDF of a potentially damaged state. In addition, principal component analysis is used to reduce the dimensionality of the PDFs (Worden et al., 2003; Tibaduiza et al., 2016; Eltouny and Liang, 2021).

In the remainder of the chapter, a theoretical background is introduced in Section 4.2, followed by an explanation of the proposed method in Section 4.3. Then, two case studies are presented in Section 4.4 and Section 4.5 respectively, followed by a comparative study in Section 4.6. Finally, the main conclusions are presented in Section 4.7.

## 4.2 Theoretical background

Principal components analysis and density ratio estimation are introduced in this section. They will be used to facilitate the damage detection method in Section 4.3.

### 4.2.1 Principal component analysis

Principal component analysis (PCA) is a technique to reduce the dimensionality of a dataset while preserving as much information (i.e., variability) as possible (Jolliffe and Cadima, 2016). It is closely related to the Karhunen-Loeve decomposition and singular value decomposition (Liang et al., 2002). In this chapter, PCA will be employed to reduce the dimensionality of a multivariate PDF.

Mathematically, PCA projects the data onto a lower-dimensional linear space, such that the variance of the projected data is maximised (Bishop, 2006). Given a matrix $\mathbf{Y} \in \mathbb{R}^{n \times d}$, where $n$ is the number of rows and $d$ is the number of columns, its projection in PCA is

$$\mathbf{X} = \mathbf{YV} \tag{4.1}$$

where $\mathbf{X} \in \mathbb{R}^{n \times d}$ is the projected data, and $\mathbf{V} \in \mathbb{R}^{d \times d}$ is the projection matrix. Each column of $\mathbf{V}$ is a eigenvector of the covariance matrix of $\mathbf{Y}$, denoted as $\mathbf{C} \in \mathbb{R}^{d \times d}$. That means $\mathbf{V}$ is obtained by solving the eigendecomposition problem (Bishop, 2006):

$$\mathbf{C} = \mathbf{V}\mathbf{\Lambda}\mathbf{V}^{\top} \tag{4.2}$$

where $\mathbf{\Lambda} \in \mathbb{R}^{d \times d}$ is a diagonal matrix whose diagonal elements are the eigenvalues.

Using only the first $k$ eigenvectors (corresponding to the first $k$ largest eigenvalues), Equation (4.1) becomes the truncated transformation

$$\mathbf{X}_k = \mathbf{YV}_k \tag{4.3}$$

where $\mathbf{V}_k \in \mathbb{R}^{d \times k}$ is a matrix of the first $k$ columns from $\mathbf{V}$, and $1 \leq k \leq d$. Each column of $\mathbf{X}_k$ represents a principal component (PC), and each row of $\mathbf{X}_k$ gives the coordinates (scores) of a data point in the principal subspace. For simplicity, the subscript $k$ is dropped hereafter as it is fixed to $\mathbf{X}$.

It is important to select an appropriate number of retained PCs, $k$. There are several rules to determine it. Two popular ones are (Jolliffe, 2002):

1 Cumulative percentage of total variance: the cumulative percentage is the ratio between the total variance of the first few PCs over the total variance of all PCs.

If the cumulative percentage exceeds a pre-chosen percentage, the corresponding PC number, $k$, will be selected. In Jolliffe (2002), the pre-chosen percentage is suggested to be between 70% and 90%.

2 Scree graph: The graph plots PC variances against PC number and links the points with lines. The selected number of retained PCs is where the slope of line is 'steep' to the left and 'not steep' to the right.

### 4.2.2 Density ratio estimation

The Density ratio estimation (DRE) method is briefly introduced in this section. For statistical approaches, the most fundamental task is to estimate the underlying PDF from samples. However, non-parametric PDF estimation is known to be a hard problem (Härdle et al., 2004). In many cases, what is of interest is the change of PDFs rather than the PDFs themselves, such as detecting damage by monitoring the change of PDFs of signals. Therefore, DRE methods that directly estimate the change (in the form of the ratio of two PDFs) without going through density estimation itself have been proposed (Sugiyama et al., 2012), e.g., the Kullback-Leibler importance estimation procedure (KLIEP) (Sugiyama et al., 2008).

Suppose there is a system which has different states and generates $k$-dimensional samples in the domain of $\mathbb{R}^k$, denoted as $\mathscr{D}$. In a state denoted as State 0, there are $n_0$ $k$-dimensional samples $\{\mathbf{x}_0[i], 1 \leq i \leq n_0\}$ from a distribution with density $p_0(\mathbf{x})$; In another state denoted as State 1, there are $n_1$ $k$-dimensional samples $\{\mathbf{x}_1[j], 1 \leq j \leq n_1\}$ from a distribution with density $p_1(\mathbf{x})$. DRE aims to estimate the density ratio

$$r(\mathbf{x}) := p_1(\mathbf{x})/p_0(\mathbf{x}) \tag{4.4}$$

First, the density ratio is modelled as

$$\hat{r}(\mathbf{x}) = \sum_{l=1}^{b} \alpha_l K_\sigma(\mathbf{x}; \mathbf{x}_1[l], h) \tag{4.5}$$

where $\hat{r}(\mathbf{x})$ is an estimate of $r(\mathbf{x})$, $\{\mathbf{x}_1[l]\}_{l=1}^{b}$ are $b$ samples randomly drawn from $\{\mathbf{x}_1[j]\}_{j=1}^{n_1}$ and are used as the centres of $K_\sigma$, $\{\alpha_l\}_{l=1}^{b}$ are parameters to be learned from the data samples, and $K_\sigma(\mathbf{x}; \mathbf{x}_1[l])$ is a kernel function with a free parameter $h$, called bandwidth, which controls the amount of smoothing (Wasserman, 2013). There are a number of kernel functions available (Murphy, 2012), and the optimal one can be selected by cross-validation (Sugiyama et al., 2008). However, for kernel regression methods, the choice of kernel function is not crucial whereas the choice of bandwidth is important (Wasserman,

2013). In this chapter, the Gaussian kernel is used, as in the original paper of the DRE method (Kawahara and Sugiyama, 2012). That is,

$$K_\sigma(\mathbf{x};\mathbf{x}_1[l]) = \exp(-\frac{\|\mathbf{x}-\mathbf{x}_1[l]\|^2}{2\sigma^2}) \tag{4.6}$$

where $\mathbf{x}_1[l]$ is the mean, $\sigma$ is the bandwidth, and $\|\cdot\|^2$ represents the Euclidean distance. The bandwidth is determined using likelihood cross-validation as described by Kawahara and Sugiyama (2012). It is worth noting that $\{\mathbf{x}_1[l]\}_{l=1}^{b}$ is a subset of $\{\mathbf{x}_1[j]\}_{j=1}^{n_1}$ and therefore $b \leq n_1$. Using $b$ samples instead of the whole $n_1$ samples for the centres is for the sake of reducing computational burden when $n_1$ is very large (Sugiyama et al., 2008). The value of $b$ can be selected by varying its value and find the value where model performance becomes stable or computational time increases significantly. A more practical way that sets $b = \min(100, n_1)$ is suggested by Kanamori et al. (2009).

Now that the density ratio has been modelled, the next step is to estimate its parameters. Using the definition of $r(\mathbf{x})$ in Equation (4.5), $p_1(\mathbf{x})$ can be approximated by

$$\hat{p}_1(\mathbf{x}) = \hat{r}(\mathbf{x})p_0(\mathbf{x}) \tag{4.7}$$

To estimate $r(\mathbf{x})$, the KLIEP method fits $\hat{p}_1(\mathbf{x})$ to the true $p_1(\mathbf{x})$ by tuning the parameters $\{\alpha_l\}_{l=1}^{b}$. Using the Kullback-Leibler (KL) divergence as a goodness of fit measure (Sugiyama et al., 2008), the objective in tuning $\alpha_l$ is to minimise

$$\begin{aligned}
\mathrm{KL}(p_1(\mathbf{x}) \,\|\, \hat{p}_1(\mathbf{x})) &= \mathrm{KL}(p_1(\mathbf{x}) \,\|\, \hat{r}(\mathbf{x})p_0(\mathbf{x})) \\
&= \int_{\mathscr{D}} p_1(\mathbf{x}) \ln \frac{p_1(\mathbf{x})}{\hat{r}(\mathbf{x})p_0(\mathbf{x})} \mathrm{d}\mathbf{x} \\
&= \int_{\mathscr{D}} p_1(\mathbf{x}) \ln \frac{p_1(\mathbf{x})}{p_0(\mathbf{x})} \mathrm{d}\mathbf{x} - \int_{\mathscr{D}} p_1(\mathbf{x}) \ln \hat{r}(\mathbf{x}) \mathrm{d}\mathbf{x}
\end{aligned} \tag{4.8}$$

where $\mathrm{KL}(\cdot \,\|\, \cdot)$ denotes the KL divergence between the two PDFs before and after the $\|$ symbol, and $\int_{\mathscr{D}}(\cdot)\mathrm{d}\mathbf{x}$ represents a multiple integral over $\mathbf{x} \in \mathscr{D}$ (i.e., $\int_{\mathscr{D}}(\cdot)\mathrm{d}\mathbf{x}$ is short for $\int_{-\infty}^{\infty}\int_{-\infty}^{\infty}\cdots\int_{-\infty}^{\infty}(\cdot)\mathrm{d}x(1)\mathrm{d}x(2)\cdots\mathrm{d}x(k)$). The first term on the last line of Equation (4.8) does not depend on $\alpha_l$ and thus can be omitted. The objective becomes to maximise

$$\begin{aligned}
&\int_{\mathscr{D}} p_1(\mathbf{x}) \ln \hat{r}(\mathbf{x}) \mathrm{d}\mathbf{x} \\
&= \mathbb{E}[\ln \hat{r}(\mathbf{x}_1)] \\
&\approx \frac{1}{n_1} \sum_{j=1}^{n_1} \ln \hat{r}(\mathbf{x}_1[j]) \\
&= \frac{1}{n_1} \sum_{j=1}^{n_1} \ln(\sum_{l=1}^{b} \alpha_l K_\sigma(\mathbf{x}_1[j];\mathbf{x}_1[l]))
\end{aligned} \tag{4.9}$$

where $\mathbb{E}[\cdot]$ represents expectation. The step from the first line to the second line in Equation (4.9) can be understood by seeing $\ln \hat{r}(\mathbf{x})$ as a random variable. Then the first line is the definition of the expected value of the random variable (Ross, 2014). The third line is an empirical approximation of the expectation based on the samples $\{\mathbf{x}_1[j]\}_{j=1}^{n_1}$.

Meanwhile, an additional constraint is introduced, since $\hat{p}_1(\mathbf{x}) = \hat{r}(\mathbf{x})p_0(\mathbf{x})$ must be a valid PDF and as such should satisfy,

$$\begin{aligned} 1 = \int_{\mathscr{D}} \hat{p}_1(\mathbf{x})\mathrm{d}\mathbf{x} &= \int_{\mathscr{D}} \hat{r}(\mathbf{x})p_0(\mathbf{x})\mathrm{d}\mathbf{x} \\ &= \mathbb{E}[\hat{r}(\mathbf{x}_0)] \\ &\approx \frac{1}{n_0}\sum_{i=1}^{n_0} \hat{r}(\mathbf{x}_0[i]) \\ &= \frac{1}{n_0}\sum_{i=1}^{n_0}\sum_{l=1}^{b} \alpha_l K_\sigma(\mathbf{x}_0[i];\mathbf{x}_1[l]) \end{aligned} \tag{4.10}$$

where the approximation is because of the empirical approximation of the expectation as in Equation (4.9).

In addition, since $r(\mathbf{x})$ is non-negative by definition, its estimate $\hat{r}(\mathbf{x})$ is naturally imposed to be non-negative for all $\mathbf{x} \in \mathscr{D}$, which can be achieved by restricting

$$\alpha_l \geq 0 \quad \text{for } l = 1, 2, \ldots, b. \tag{4.11}$$

Now the optimization problem is summarized as

$$\begin{cases} \max\limits_{\{\alpha_l\}_{l=1}^b} & \dfrac{1}{n_1}\sum\limits_{j=1}^{n_1} \ln(\sum\limits_{l=1}^{b} \alpha_l K_\sigma(\mathbf{x}_1[j];\mathbf{x}_1[l])), \\ \text{s.t.} & \dfrac{1}{n_0}\sum\limits_{i=1}^{n_0}\sum\limits_{l=1}^{b} \alpha_l K_\sigma(\mathbf{x}_0[i];\mathbf{x}_1[l]) = 1, \\ & \text{and } \ \alpha_1, \ldots, \alpha_b \geq 0. \end{cases} \tag{4.12}$$

This is a convex optimization problem, and the global solution can be obtained. More details can be found in Kawahara and Sugiyama (2012).

## 4.3 Proposed damage detection method

In this section, the damage detection method is proposed. The key idea is to detect damage by monitoring the change of the PDF of signals, which would typically be acceleration time histories. Accordingly, there are essentially two steps: (i) define the multivariate PDF based on the signals; (ii) estimate the change between the PDFs using DRE and use it as a damage indicator.

### 4.3.1 Sequence samples and the multivariate probability density function

Let $\{y(1), y(2), \cdots, y(N)\}$ represent a vibration response time series from a single sensor, with equal time steps and a total number of time steps $N$. This part aims to characterize the response with a multivariate PDF. The PDF is assumed to be non-Gaussian and unknown, although the proposed method also works for Gaussian PDFs.

Intuitively, a univariate PDF of the vibration response time series may be considered as in Figueiredo et al. (2009). In their work, the acceleration signals in one time series are assumed to be drawn from a univariate PDF. They detected the damage by comparing univariate PDFs of accelerations from the undamaged state and a potentially damaged state. Their key idea was that the PDF of the acceleration from the undamaged state is Gaussian, while the PDF becomes non-Gaussian if nonlinear damage occurs. However, Figueiredo et al. (2009)'s work does not fit the scenario of this chapter, where the structure is nonlinear both before and after damage. More importantly, seeing the time series data as a univariate PDF loses the information of temporal correlation. To overcome this problem, sequences of the signals were used in Kawahara and Sugiyama (2012) for applications on respiration and speech monitoring. The sequences are generated by a sliding window that traverses the entire time series. A compact expression of these sequences is with a Hankel matrix,

$$\mathbf{Y} = \begin{bmatrix} y(1) & y(2) & \cdots & y(d) \\ y(2) & y(3) & \cdots & y(d+1) \\ \vdots & \vdots & \ddots & \vdots \\ y(n) & y(n+1) & \cdots & y(N) \end{bmatrix} \tag{4.13}$$

where $n = N - d + 1$ is the number of rows, and each row is a sequence generated by a sliding window of width $d$. Each row is called a sequence sample. $n$ is the number of sequence samples, and $d$ is the sequence length or dimension.

The $d$-dimensional sequence samples in Equation (4.13), i.e., rows of $\mathbf{Y}$, are assumed to be sampled from a multivariate random variable $\mathscr{Y}$ following a PDF $p(\mathbf{y})$. That is

$$\mathscr{Y} \sim p(\mathbf{y}) \tag{4.14}$$

From the standpoint of a stochastic process, $\mathscr{Y}$ can be viewed as a stochastic process with a sample time series, $\{y(1), y(2), \cdots, y(d)\}$, and a PDF, $p(\mathbf{y})$. The Hankel matrix arrangement is equivalent to assuming the underlying stochastic process of the vibration

response is ergodic, which is a generally applied assumption in common practice (Lutes and Sarkani, 2004).

Before addressing the estimation of $p(\mathbf{y})$, the sequence samples are preprocessed by PCA and standardisation. PCA is used to reduce the dimensionality $d$. Although larger $d$ is desirable as it means more correlation information is involved in the PDF, it also leads to the estimation of a high dimensional PDF, which is a hard problem (Härdle et al., 2004). To reduce dimensionality while retaining as much information as possible, PCA is applied to $\mathbf{Y}$. Specifically, $\mathbf{Y} \in \mathbb{R}^{n \times d}$ is transformed to a lower-dimensional matrix $\mathbf{X} \in \mathbb{R}^{n \times k}$ through Equation (4.3). It is worth noting that PCA is only applied to the data from the undamaged state, i.e.,

$$\mathbf{X}_0 = \mathbf{Y}_0 \mathbf{V}_0 \tag{4.15}$$

where the subscript 0 represents the data corresponding to the undamaged state. For the data from a potentially damaged state, $\mathbf{V}_0$ is reused, i.e.,

$$\mathbf{X}_1 = \mathbf{Y}_1 \mathbf{V}_0 \tag{4.16}$$

where the subscript 1 represents the data corresponding to a potentially damaged state.

When applying PCA in Equation (4.15), it is important to select an appropriate number of retained PCs, $k$. In this chapter, a practical two-stage approach is employed, based on the rules described in Section 4.2.1. (i) First, the rule of cumulative percentage of total variance is applied to select a range of PC numbers that correspond to cumulative percentages between 70% and 90%. (ii) Within the selected range, a single PC number is determined using the scree graph rule. This is used to define the number of retained PCs.

After PCA, $\mathbf{X}$ is standardised to avoid numerical instabilities that may occur in optimisation. Specifically, each column in $\mathbf{X}$ is standardised separately by subtracting the mean and then dividing by its standard deviation.

Similar to Equation 4.14, the sequence samples in $\mathbf{X}_0$, which are from the undamaged state, are assumed to be sampled from a multivariate random variable $\mathscr{X}_0$ following a PDF $p_0(\mathbf{x})$. Likewise, the sequence samples in $\mathbf{X}_1$, which are from a potentially damaged state, are assumed to be sampled from a multivariate random variable $\mathscr{X}_1$ following a PDF $p_1(\mathbf{x})$. That is

$$\begin{aligned} \mathscr{X}_0 &\sim p_0(\mathbf{x}) \\ \mathscr{X}_1 &\sim p_1(\mathbf{x}) \end{aligned} \tag{4.17}$$

It is worth noting that the samples in Equation 4.17 are not independent. However, consistent estimations can still be obtained as it does not rely on independency (van der Vaart and van der Vaart, 1998), although the convergence rate of the subsequent estimations may be slower.

### 4.3.2 Damage index and density ratio estimation

After characterising the vibration time series with PDFs, a damage index (DI) is defined to measure the changes between the PDF of the undamaged state and that of a potentially damaged state to indicate damage.

The KL divergence is a widely used measure of the difference between two PDFs (Kullback, 1997). For the PDF of vibration time series in the undamaged state, $p_0(\mathbf{x})$, and the PDF of a vibration time series in a potentially damaged state, $p_1(\mathbf{x})$, the KL divergence between them is

$$\mathrm{KL}(p_1(\mathbf{x}) \parallel p_0(\mathbf{x})) = \int_{\mathscr{D}} p_1(\mathbf{x}) \ln \frac{p_1(\mathbf{x})}{p_0(\mathbf{x})} \mathrm{d}\mathbf{x} \tag{4.18}$$

The DI is simply defined as the averaged KL divergence. Specifically, suppose we have $n_r$ vibration time series of the undamaged state, the DI of the proposed method, denoted as $\mathrm{DI}_{\mathrm{DRE}}$, is defined as

$$\mathrm{DI}_{\mathrm{DRE}} = \frac{1}{n_r} \sum_{m=1}^{n_r} \mathrm{KL}(p_1(\mathbf{x}) \parallel p_{0,m}(\mathbf{x})) \tag{4.19}$$

where $p_{0,m}(\mathbf{x})$ is the PDF of the $m$th vibration time series in the undamaged state. Substituting Equation (4.18) into Equation (4.19) gives

$$\begin{aligned} \mathrm{DI}_{\mathrm{DRE}} &= \frac{1}{n_r} \sum_{m=1}^{n_r} \int_{\mathscr{D}} p_1(\mathbf{x}) \ln \frac{p_1(\mathbf{x})}{p_{0,m}(\mathbf{x})} \mathrm{d}\mathbf{x} \\ &= \frac{1}{n_r} \sum_{m=1}^{n_r} \mathbb{E}[\ln \frac{p_1(\mathbf{x})}{p_{0,m}(\mathbf{x})}] \\ &\approx \frac{1}{n_r} \sum_{m=1}^{n_r} \frac{1}{n_1} \sum_{j=1}^{n_1} \ln(r_m(\mathbf{x}_1[j])) \end{aligned} \tag{4.20}$$

where the steps from the first line to the third line are similar to the equivalent steps in Equation (4.9), and $r_m(\mathbf{x}_1[j])$ is the output value of the density ratio function

$$r_m(\mathbf{x}) = p_1(\mathbf{x}) / p_{0,m}(\mathbf{x}) \tag{4.21}$$

for an input sample $\{\mathbf{x}_1[j]\}$, where $1 \le j \le n_1$.

To estimate $r_m(\mathbf{x})$, the DRE method described in Section 4.2.2 is used. Specifically, $r_m(\mathbf{x})$ is modelled by Equation (4.5) and estimated by solving the optimisation problem in Equation (4.12). The value of $b$ is determined by $b = \min(100, n_1)$ as in (Kanamori et al., 2009).

### 4.3.3 Damage detection threshold

After DIs are obtained, the state of the structure can be diagnosed. Specifically, if a DI is larger than a predetermined threshold, the corresponding state will be believed to be damaged. Otherwise, the state is believed to be undamaged. To determine the threshold, a simple way is to assume the DIs of the undamaged state are normally distributed and choose the confidence limit of a certain confidence level as the threshold (Farrar and Worden, 2012; Yan et al., 2005a; Bao et al., 2013a). However, considering that the number of available time series and hence the number of DIs of the undamaged state may be limited, it is more appropriate to use the $t$-distribution. Suppose there are $n_{\mathrm{DI}}$ DIs of the undamaged state. The sample mean and the sample standard deviation of these DIs are denoted as $\mu_{\mathrm{DI}}$ and $\sigma_{\mathrm{DI}}$ respectively. The threshold is defined as the upper one-sided 95% confidence limit of the $t$ distribution with $(n_{\mathrm{DI}} - 1)$ degrees of freedom, and it is expressed as,

$$\xi = \mu_{\mathrm{DI}} + \frac{\sigma_{\mathrm{DI}}}{\sqrt{n_{\mathrm{DI}}}} t_{(1-95\%)}(n_{\mathrm{DI}} - 1) \tag{4.22}$$

The overall steps of the proposed method are illustrated in Figure 4.1.

## 4.4 Application 1: experimental nonlinear beam

The damage detection method is demonstrated using experimental data of a beam with initial nonlinearity. The testing was performed at the Structural Health Monitoring Lab of São Paulo State University (UNESP)/Ilha Solteira, and the data are available online (Structural Health Monitoring Lab - São Paulo State University/Ilha Solteira, 2021). This benchmark is referred to as UNESP-MAGNOLIA and has been used in Villani et al. (2019b); Shiki et al. (2017); Tahara (2019) and Shiki (2016). Section 4.4.1 presents a description of the experimental nonlinear beam and signals, followed by the model parameter selection in Section 4.4.2 and its discussion in Section 4.4.3. Finally, the damage detection results are presented in Section 4.4.4.

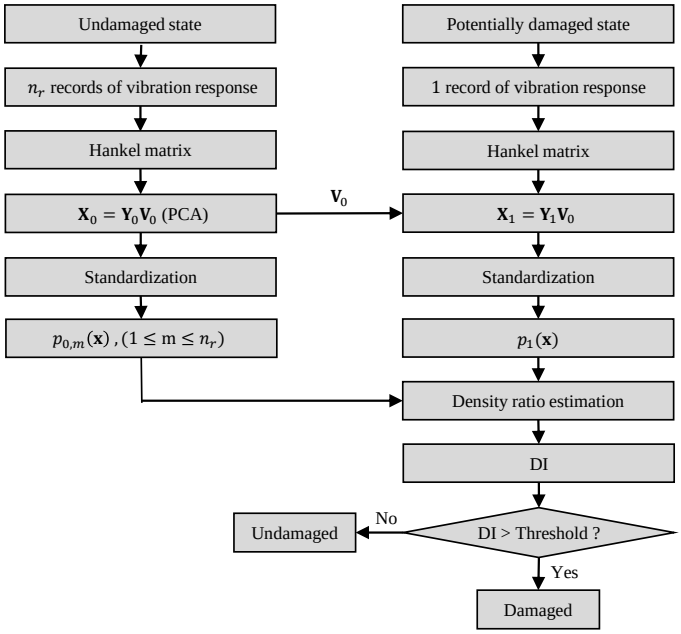


Figure 4.1: Flowchart of the proposed method

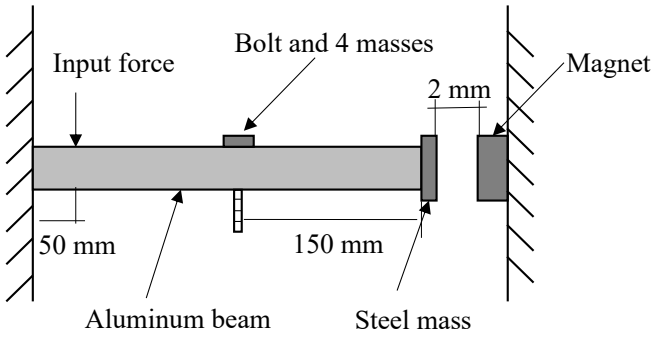


Figure 4.2: Schematic diagram of the experiment setup (Adapted from Figure 1 in Shiki et al. (2017) ).

### 4.4.1 Experimental setup

The schematic diagram of the experiment setup is shown in Figure 4.2. It consists of a cantilever aluminium beam with dimensions of 300 mm × 19 mm × 3.2 mm. A steel mass is fixed at the free end of the beam and is attracted by a magnet placed 2mm beyond the end of the beam, giving a nonlinear force. A bolted connection is placed 150 mm from the free end with four nuts of 1 g each. Three damage levels were simulated by sequentially removing nuts. The beam was excited by an electrodynamic shaker which is 50 mm from

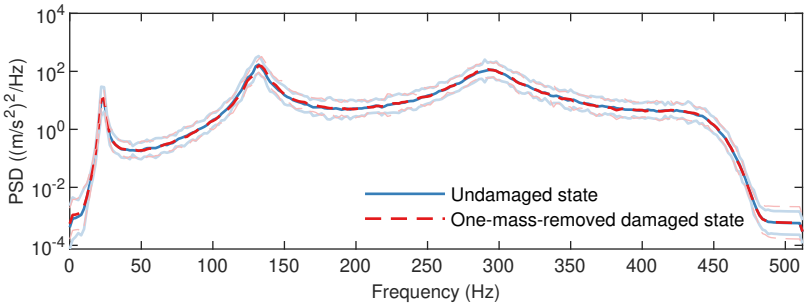


Figure 4.3: Comparison of the Welch PSDs of the experimental nonlinear beam in the undamaged state and the state with one mass removed. For each state, 25 PSDs are estimated from different time series, with their mean and plus and minus three standard deviations presented by the middle line and the boundary lines respectively.

its clamped end. The excitation was random noise input with a frequency range of 10 to 420 Hz. The acceleration time series at the free end of the beam was recorded at a sampling frequency of 1024 Hz. Each record has a period of 4 s.

Figure 4.3 shows the Welch Power Spectral Densitites (PSDs) estimated from the accelerations in the undamaged state and the state with one mass removed, using a Hamming window of 512 samples with 50% overlaps. For each state, 25 PSDs were estimated from different time series, with their mean and plus and minus three standard deviations presented by the middle line and the boundary lines, respectively. From Figure 4.3, it can be seen that it is challenging to differentiate between the two states in the PSDs. Although the PDFs in this example are multi-dimensional, and the PDFs themselves are not used in the analysis, but rather only their ratios, for the sake of visualisation Figure 4.4 shows the marginal PDFs for the first and second PCs of the undamaged state and the state with one mass removed.

### 4.4.2 Model parameter selection

The proposed model requires selection of the sequence length, $d$, and the number of PCs retained, $k$. It is worth noting that given a value of $d$, the appropriate value of $k$ can be easily determined using the practical approach described in Section 4.3.1. To select an appropriate value of $d$, the performance of the proposed method was estimated with $d = \{40, 45, \cdots, 110\}$ and the value of $d$ that had the best performance was selected. The performance is measured with a receiver operating characteristics (ROC) curve (Fawcett, 2006). The ROC is obtained by incrementally varying the damage threshold from a minimum to a maximum and plotting its corresponding true positive rate and false-

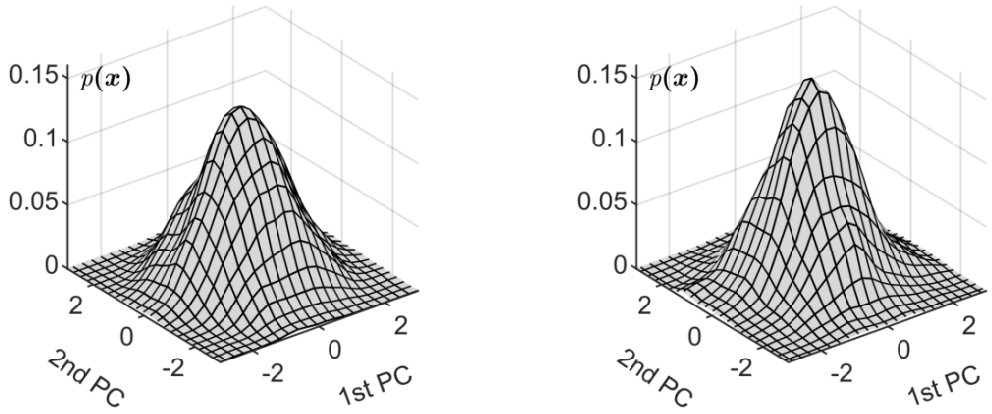


(a) (b)

Figure 4.4: Marginal distributions of the first and second PCs for: (a) the undamaged beam and (b) the beam with one mass removed. The PCs have been standardized separately.

positive rate. The area under the curve (AUC) of the ROC, referred to as ROC-AUC, is used to measure the damage detection performance.

The original experimental data were split equally into two subsets: one for parameter selection in this section and the other one for model performance testing in Section 4.4.4. The parameter selection procedure used 25 reference time series of the undamaged state and 50 testing time series (25 each of the undamaged state and the state with one mass removed). Figure 4.5a shows the obtained ROC-AUC for the selection of $d$, where for each value of $d$ an appropriate value of $k$ was determined using the practical approach described in Section 4.3.1. The ROC-AUC is not very sensitive to $d$, but $d = 45$, where the ROC-AUC is a maximum, was selected as the optimal sequence length. The underlying determination procedure of $k$ for $d = 45$ is also illustrated, in Figure 4.5b. Specifically, the boundaries of 70% and 90% cumulative percentage of total variance are first identified to be at $k = 9$ and $k = 19$, as represented by the vertical lines in Figure 4.5b. Then, within these boundaries, $k = 13$, marked with a circle, is selected according to the scree graph rule (the slope of the lines are 'steep' to the left and 'not steep' to the right).

### 4.4.3 Discussion on parameter selection

To check the performance of the proposed selection method for $k$, the values of ROC-AUC were obtained over the parameter values $d = \{40, 45, \cdots, 110\}$ and $k = \{9, 10, \cdots, 25\}$, as shown in Figure 4.6. The line in the figure illustrates the values of parameters obtained

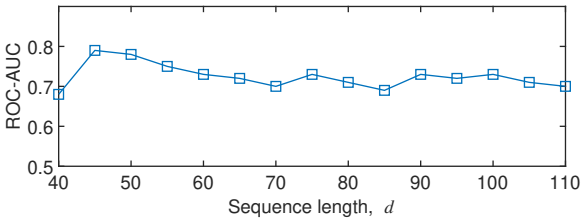


(a)

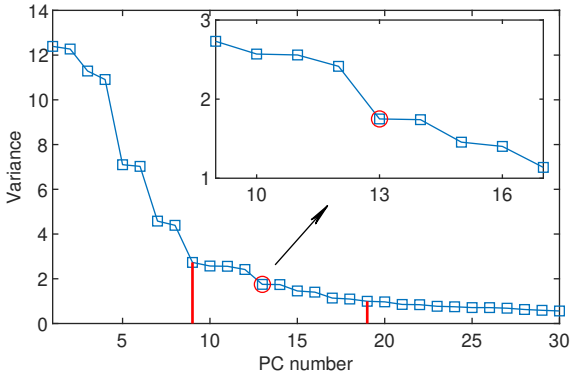


(b)

Figure 4.5: Selection of parameters for the experimental nonlinear beam: (a) ROC-AUC for the selection of $d$ and (b) the underlying determination procedure of $k$ for the optimum $d = 45$.

by the proposed parameter selection method. It can be seen that the line approximately follows the minimum value of $k$ to achieve a ROC-AUC of at least 0.70. A higher value of ROC-AUC is desirable, but limiting $k$ is helpful to reduce the computational burden. Hence this indicates that the proposed method for the selection of $k$ is effective.

The selection of $k$ only requires data for the undamaged state. The optimal selection of $d$ also requires data from a damaged state, but in real-world applications data from a known damaged state are unlikely to be available. Therefore, it is desirable to select $d$ without damaged condition data. In this example, the optimal value $d = 45$ means the period of the sequence samples is approximately equal to the natural period of the first mode of the beam (23Hz (Villani et al., 2019b)), considering the sampling frequency is 1024 Hz. As a larger $d$ means more information can be extracted by the PDF from the time series while a smaller $d$ improves the estimation accuracy of the DRE model, this finding may suggest a good trade-off and could be used as a practical rule to select $d$ when damaged data are unavailable. That is, the value of $d$ should allow the sequence sample to cover the natural period of the first mode of the structure (but see also Section 4.5.2). It should also be noted that the heatmap in Figure 4.6 shows that the performance of the proposed method is sensitive to $k$ but relatively insensitive to $d$. This indicates

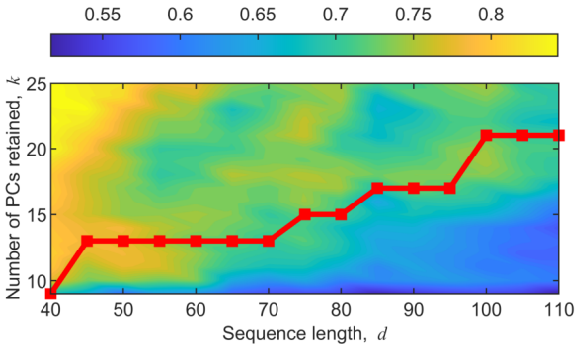


Figure 4.6: Heatmap of the ROC-AUC for the experimental nonlinear beam over the parameter values $d = \{40, 45, \cdots, 110\}$ and $k = \{9, 10, \cdots, 25\}$. The line indicates the parameters obtained by the proposed selection method for $k$.

that appropriate selection of $k$ is important, while the choice of $d$ is less significant, hence justifying the usage of the proposed practical rule for the selection of $d$.

### 4.4.4 Results

With the selected parameters, $d = 45$ and $k = 13$, the performance of the proposed method for different damage levels is presented. Figure 4.7 shows the distribution of the DIs for 50 testing time series (25 each of the undamaged state and a 'damaged' state) based on 25 reference time series of the undamaged state. In Figure 4.7, the box plot is generated by the 25 DIs for the undamaged state, while the distributed circles represent the 25 DIs for each damaged state. The circles for the damaged state generally become higher as the damage level increases, which means that the DIs increase when the structure is more severely damaged. Although the absolute difference between the minimum (around 0.0365) and maximum (around 0.0380) is small, how well the DIs of the undamaged state and the DIs of the damaged state can be separated is more important, as this reflects the performance of the damage detection method. The less the overlap between the box and the circles, the more easily the damaged state and the undamaged state can be separated, and better damage detection performance can be achieved. The amount of overlap between the DIs for the damaged and undamaged states decreases as the damage level increases. This implies that the performance improves as the damage level increases, as may be expected.

Based on the DIs in Figure 4.7 and the threshold determined by the method in Section 4.3.3, the damage detection performance is evaluated with different metrics:

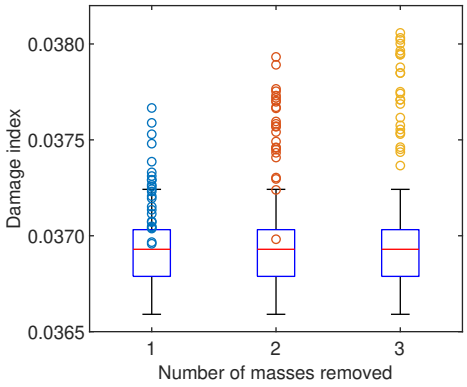


Figure 4.7: Distribution of the DIs for different damage levels of the nonlinear beam. The box plot is generated by the DIs from the undamaged state; the central line indicates the median, the bottom and top edges of the box represent the 25th and 75th percentiles, and the extended bars show the most extreme data points. The circles denote the DIs from the damaged states.

Table 4.1: Damage detection performance metrics of the experimental nonlinear beam

| Method | Masses removed | Accuracy | Recall | F1 | mIoU | ROC-AUC |
|---|---|---|---|---|---|---|
| PCA-DRE | 1 | 0.720 | 0.520 | 0.650 | 0.552 | 0.907 |
| | 2 | 0.940 | 0.960 | 0.941 | 0.887 | 0.986 |
| | 3 | 0.960 | 1.000 | 0.962 | 0.923 | 1.000 |
| Gaussian-PDF | 1 | 0.560 | 0.160 | 0.267 | 0.338 | 0.592 |
| | 2 | 0.900 | 0.960 | 0.906 | 0.818 | 0.955 |
| | 3 | 0.920 | 1.000 | 0.926 | 0.851 | 1.000 |

accuracy, recall, F1-score, mean intersection over union (mIoU), and the ROC-AUC. More details of the first four metrics can be found in Eltouny and Liang (2021). The results are shown in table 4.1, along with the results of a Gaussian-PDF-based method which will be introduced in Section 4.6. These results will be discussed in Section 4.6.

## 4.5 Application 2: offshore wind turbine structure

This section demonstrates the performance of the damage detection method on an offshore wind turbine with nonlinear soil-pile interaction, subjected to scouring damage. The OWT and the signals are briefly described in Section,4.5.1. Then, the model parameter selection and its discussion are presented in Section 4.5.2 and Section 4.5.3, respectively. Finally, the results are shown in Section 4.5.4.

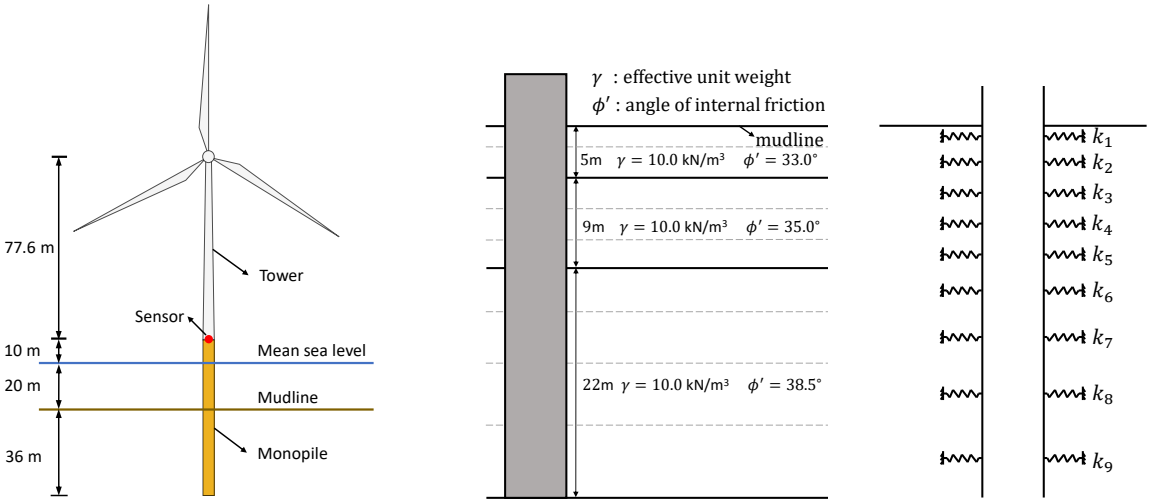


(a) (b) (c)

Figure 4.8: Modelling of the offshore wind turbine and foundation: (a) Offshore wind turbine; (b) Soil properties; (c) Equivalent point springs.

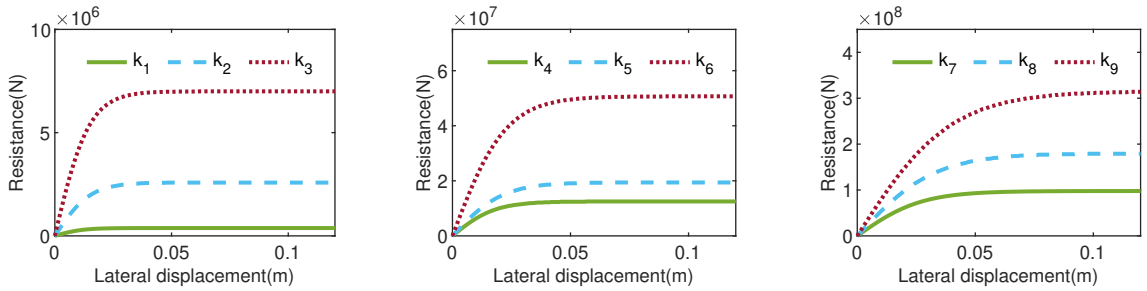


(a) (b) (c)

Figure 4.9: Lateral displacement vs resistance curves for the equivalent point springs in the undamaged state.

### 4.5.1 Offshore wind turbine and signals

The OWT consists of the National Renewable Energy Laboratory (NREL) 5MW baseline wind turbine (Jonkman et al., 2009) and a monopile foundation (Jonkman et al., 2008a), as shown in Figure 4.8a. The NREL 5MW baseline wind turbine is a conventional three-bladed upwind variable-speed variable-pitch turbine. The soil profile and properties are taken from Jonkman et al. (2008a) and are illustrated in Figure 4.8b, where $\gamma$ is effective unit weight and $\phi'$ is angle of internal friction. More specifications of the structural properties are summarised in Table 4.2.

The OWT was simulated in DNV-GL's Bladed software (DNV, 2020), an integrated wind turbine design tool for calculating turbine performance and dynamic loading and

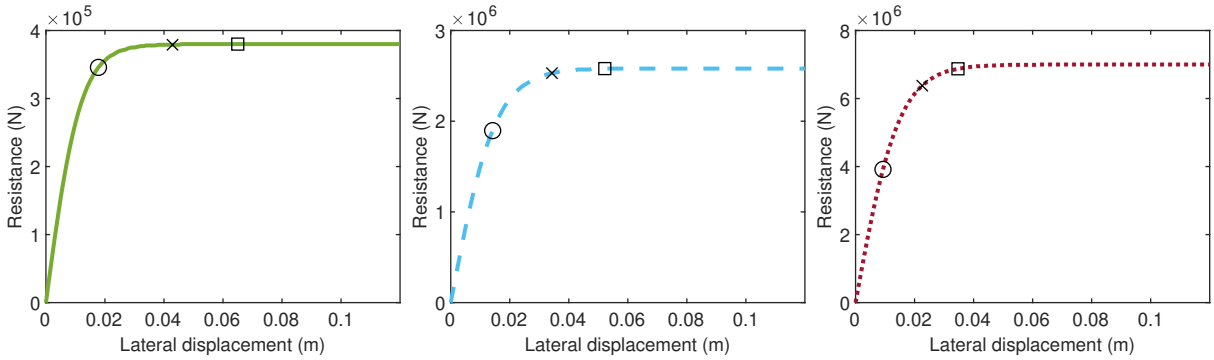


(a) $k_1$ (b) $k_2$ (c) $k_3$

Figure 4.10: Deflection ranges at equivalent point springs $k_1$, $k_2$, and $k_3$. Each line is the lateral displacement vs resistance curve for an equivalent point spring (as shown in Figure 4.9 (a)). There are three points on each line. The circle point represents the mean value of the deflection, the cross point represents the mean plus two times the standard deviation of the deflection, and the square point represents the maximum value of the deflection.

response. For simplicity, the OWT was set as parked (the rotor is in a standstill condition), and all the excitations were simplified to be band-limited Gaussian white noise with a frequency range of $0-10$ Hz and a power spectral density of $1\times10^{11}\text{N}^2/\text{Hz}$, applied at the nacelle in the fore-aft direction. The OWT is initially nonlinear because of the nonlinear soil-pile interaction, which is commonly treated using p-y curves in industry (American Petroleum Institute, 2000; Andersen et al., 2012). In Bladed, the p-y curves were modelled via 'equivalent point springs' (DNV, 2020). Accordingly, the three layers of soil in Figure 4.8b were further divided into nine sub-layers with thicknesses of 2 m, 3 m, 3 m, 3 m, 3 m, 4 m, 5 m, 6 m and 7 m from the top sub-layer to the bottom. Each of these sub-layers was represented by a spring, as shown in Figure 4.8c. The spring stiffness curve of each sub-layer was obtained according to the American Petroleum Institute

Table 4.2: Main properties of the tower and monopile (Jonkman et al., 2009, 2008a)

| Property | Value |
|---|---|
| Tower top diameter, wall thickness | 3.87 m, 0.019 m |
| Tower base diameter, wall thickness | 6.0 m, 0.027 m |
| Foundation diameter, wall thickness | 6.0 m, 0.06 m |
| Density | 8500 kg/m$^3$ |
| Young's modulus | 210 GPa |
| Shear modulus | 80.8 GPa |
| Damping ratio (all modes) | 1% |

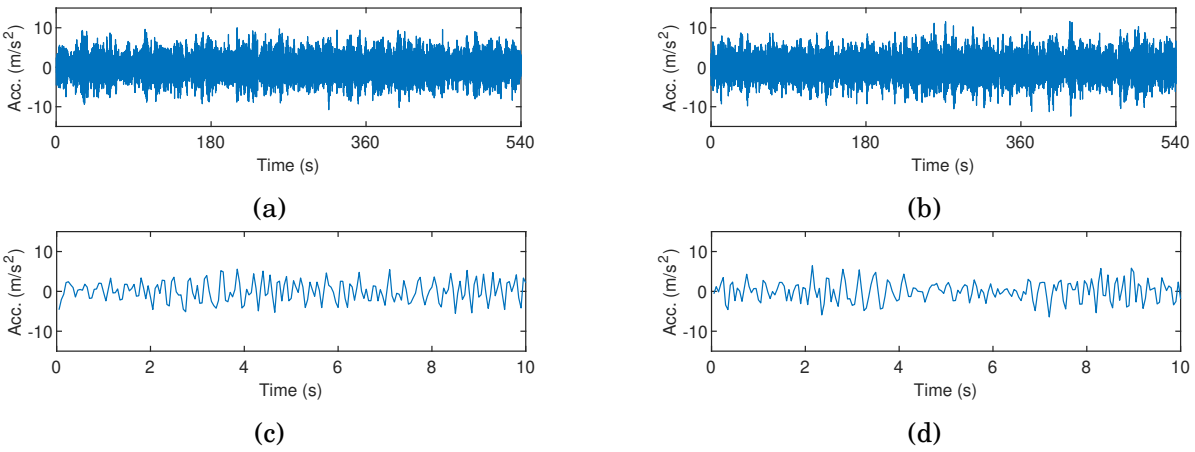


Figure 4.11: Typical acceleration time series from the top of the monopile of the OWT: (a) 540 s time series in the undamaged state; (b) 540 s time series in the 0.36 m damaged state. (c) and (d) are zoomed views of the first 10s in (a) and (b), respectively.

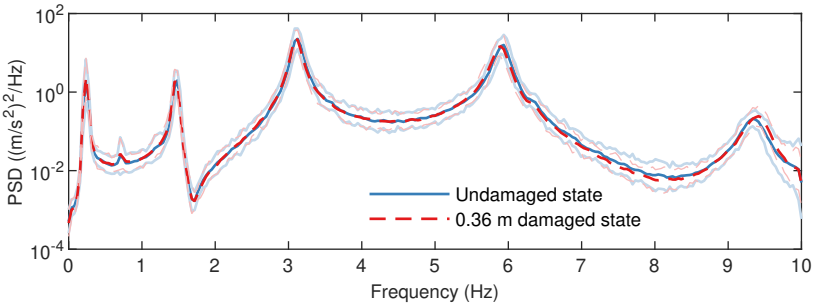


Figure 4.12: Comparison of the Welch PSDs in the undamaged state and the 0.36 m damaged state of the OWT. For each state, 20 PSDs are estimated from different time series, with their mean and plus and minus three standard deviations presented by the middle line and the boundary lines respectively.

(API) p-y method (American Petroleum Institute, 2000) using the soil properties (i.e., $\gamma$, $\phi'$ and soil depth). Figure 4.9 shows the spring stiffness curves for the undamaged state. In other words, the pile is supported by a series of non-linear elastic springs, which simulate soil reactions, and the unloading occurs along the same loading curve (Vieira et al., 2020; Carswell et al., 2015). The considered damage was scouring (Devriendt et al., 2014; Prendergast et al., 2015), i.e., erosion of the mudline near the foundation. Three different damage levels were simulated by removing 0.24 m, 0.36 m, and 0.48 m of the top layer soil. After the removal of soil, the depth of each sub-layer was recalculated and the spring stiffness of each sub-layer was updated accordingly. To demonstrate the nonlinear effects caused by the soil-pile interaction, the deflection ranges at the top three equivalent point spring $k_1$, $k_2$, and $k_3$ are illustrated in Figure 4.10. The

deflection ranges were calculated based on a typical simulation. Each line is the lateral displacement vs resistance curve for an equivalent point spring (as shown in Figure 4.9 (a)). There are three points on each line. The circle point represents the mean value of the deflection during the simulation, the cross point represents the mean plus two times the standard deviation of the deflection, and the square point represents the maximum value of the deflection. It can be seen that the nonlinear effects were triggered for $k_1$, $k_2$, and $k_3$. The deflection ranges of other springs are not shown as they are too small.

The accelerations in the fore-aft direction from the virtual sensor at the top of the monopile (see Figure 4.8a) were obtained from Bladed. The simulated period was 600 s, and the accelerations were sampled at 20 Hz. For each simulation, the first 60 s were discarded to eliminate transient response, and only the last 540 s were used for further analysis. Gaussian white noise was added to the simulated accelerations from Bladed to consider vibration measurement noise, with a signal-to-noise ratio of 30 dB.

Typical acceleration time series are plotted in Figure 4.11. Figure 4.11a shows an acceleration time series for the undamaged state; Figure 4.11b presents a time series for the 0.36 m damaged state; Figure 4.11c and Figure 4.11d show zoomed views of the first 10 s signals in Figure 4.11a and Figure 4.11b, respectively. Figure 4.12 displays the Welch PSDs estimated from the acceleration time series for the undamaged state and the 0.36 m damaged state, using a Hamming window of 2048 samples and 50% overlaps. For each state, 20 PSDs were estimated from different time series. The middle curves in Figure 4.12 are the mean PSDs, and the boundary lines represent plus and minus three standard deviations. It can be seen that it is challenging to differentiate between the undamaged state and the damaged state in the PSDs. Similarly to that in Section 4.4.1, the marginal PDFs for the first and second PCs of the undamaged state and the 0.36 m damaged state are illustrated, in Figure 4.13.

### 4.5.2 Model parameter selection

As in Section 4.4.2, the original data were split equally into two subsets; the first subset was used in this section to select the sequence length, $d$, and the number of the retained principal components, $k$. The procedure used 20 reference time series of the undamaged state and 40 testing time series (20 each of the undamaged state and the 0.36 m damaged state). The obtained ROC-AUC for selecting $d$ is displayed in Figure 4.14a, with the corresponding determination of $k$ in Figure 4.14b. Though the ROC-AUC in Figure 4.14a becomes stable for $d > 120$, $d = 130$, where the ROC-AUC is a maximum, is selected as the optimal sequence length. The underlying determination procedure of $k$ is illustrated

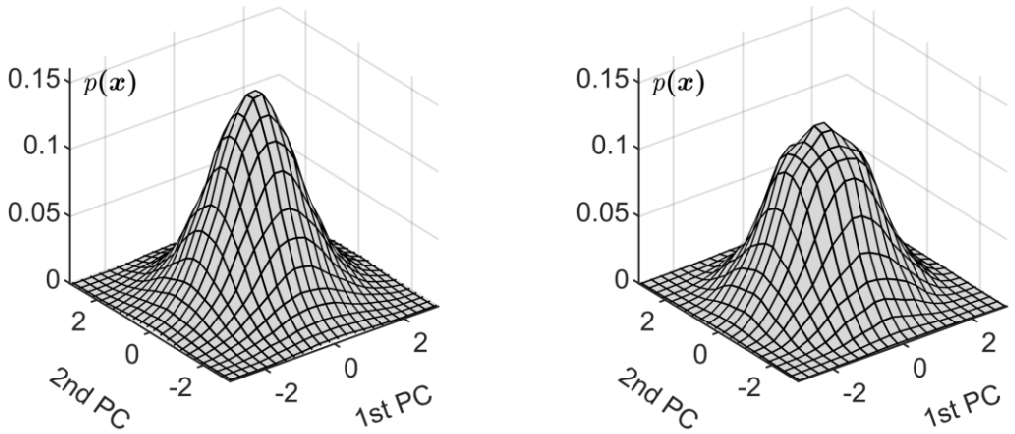


(a) (b)

Figure 4.13: Marginal distributions of the first and second PCs for: (a) the undamaged OWT and (b) the 0.36 m damaged OWT. The PCs have been standardized separately.

in Figure 4.14b. Specifically, the boundaries of 70% and 90% cumulative percentage of total variance were first identified to be at $k = 9$ and $k = 26$, as represented by the vertical lines in Figure 4.14b. Then, within the boundaries, $k = 13$, marked in a circle, was selected according to the scree graph rule.

### 4.5.3 Discussion on parameter selection

Similarly to as in Section 4.4.2, the proposed method for selection of $k$ is verified. Figure 4.15 shows the heatmap of the ROC-AUC over the parameter values $d = \{40, 50, \cdots, 200\}$ and $k = \{5, 6, \cdots, 25\}$, and the line of the parameters obtained by the proposed parameter selection method. It can be seen that the line is consistent with the area of higher ROC-AUC values. Again the proposed method for selection of $k$ is shown to be effective.

As in Section 4.4.3, the selection of $d$ in the cases where damaged data are not available is discussed. In this example, the optimum $d = 130$ suggests the value of $d$ should allow the sequence sample to cover approximately 1.6 times the first natural period of the structure. This finding is broadly similar with that in Section 4.4.3, where 1 times the first period was suggested. In addition, the line in Figure 4.15 shows that the performance of the proposed method is sensitive to $k$ but relatively insensitive to $d$, indicating that the selection of $d$ is less important than the selection of $k$. Again, this justifies the usage of the practical rule for the selection of $d$.

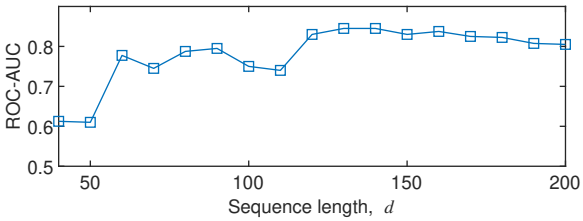


(a)

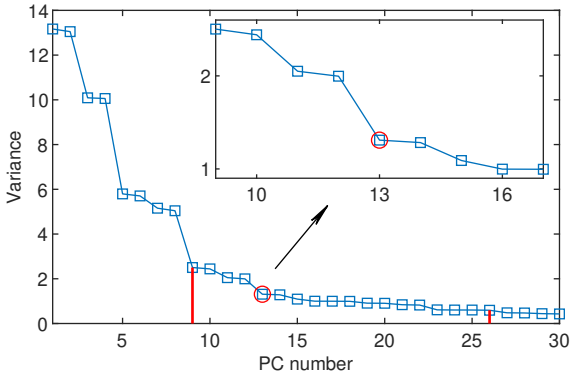


(b)

Figure 4.14: Selection of parameters for the OWT: (a) ROC-AUC for the selection of $d$ and (b) the underlying determination procedure of $k$ for the optimum $d = 130$.

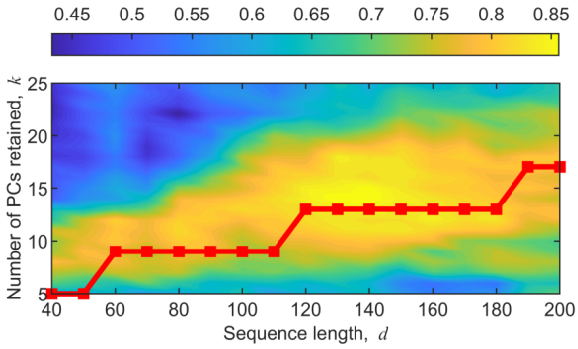


Figure 4.15: Heatmap of the ROC-AUC for the OWT over the parameter values $d = \{40, 50, \cdots, 200\}$ and $k = \{5, 6, \cdots, 25\}$. The line indicates the parameters obtained by the proposed selection method.

### 4.5.4 Results

With the selected parameters, $d = 130$ and $k = 13$, the performance of the proposed method for different scour depths is presented. Figure 4.16 shows the distribution of the DIs for the OWT. It is obtained similarly to Figure 4.7 and demonstrates similar findings: the DIs increase when the structure is more severely damaged, and the performance

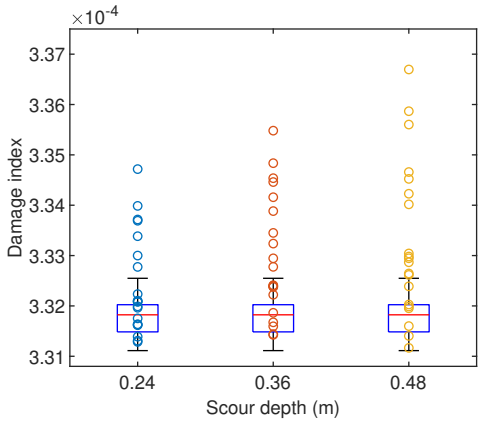


Figure 4.16: Distribution of the DIs for different scour depths of the OWT. The box plot is generated by the DIs from the undamaged state; the central line indicates the median, the bottom and top edges of the box represent the 25th and 75th percentiles, and the extended bars show the most extreme data points. The circles denote the DIs from the damaged states.

becomes better as the damage level increases. Again, the data used here are different from the data used for the parameter selection.

The damage detection performance is evaluated with different metrics: accuracy, recall, F1-score, mean intersection over union (mIoU), and the ROC-AUC. More details of the first four metrics can be found in Eltouny and Liang (2021). The results are shown in table 4.1, along with the results of a Gaussian-PDF-based method which will be introduced in Section 4.6. These results will be discussed in Section 4.6.

Table 4.3: Damage detection performance metrics of the experimental nonlinear beam

| Method | Scour depth (m) | Accuracy | Recall | F1 | mIoU | ROC-AUC |
|---|---|---|---|---|---|---|
| PCA-DRE | 0.24 | 0.583 | 0.230 | 0.342 | 0.374 | 0.638 |
| | 0.36 | 0.663 | 0.370 | 0.506 | 0.474 | 0.751 |
| | 0.48 | 0.733 | 0.530 | 0.660 | 0.568 | 0.823 |
| Gaussian-PDF | 0.24 | 0.520 | 0.125 | 0.194 | 0.302 | 0.599 |
| | 0.36 | 0.553 | 0.190 | 0.278 | 0.341 | 0.725 |
| | 0.48 | 0.620 | 0.325 | 0.439 | 0.426 | 0.819 |

## 4.6 Comparative study

As the proposed method (denoted as the PCA-DRE-based method hereafter) takes advantage of higher-order statistics, embedded in the PDFs, it is interesting to compare it with a Gaussian-PDF-based method, which only considers the second-order statistical information.

Gaussian-PDF-based methods assume the multivariate PDFs of the signals for the undamaged and damaged states are Gaussian. If $p_1(\mathbf{x})$ and $p_{0,m}(\mathbf{x})$ are Gaussian and standardised to be zero-mean, the KL divergence between them is reduced to a closed-form expression (Hershey and Olsen, 2007),

$$\begin{aligned} &\mathrm{KL}_{\mathrm{Gaussian}}(p_1(\mathbf{x}) \parallel p_{0,m}(\mathbf{x})) = \\ &\qquad \frac{1}{2}\left(\ln \frac{\det(\mathbf{C}_{0,m})}{\det(\mathbf{C}_1)} - d + \mathrm{tr}\left(\mathbf{C}_{0,m}^{-1}\mathbf{C}_1\right)\right) \end{aligned} \tag{4.23}$$

where $d$ is the dimensionality of the PDFs, and $\mathbf{C}_1$ and $\mathbf{C}_{0,m}$ are the covariance matrices of $p_1(\mathbf{x})$ and $p_{0,m}(\mathbf{x})$ respectively.

The Gaussian-PDF-based method used in the comparison adopts the same DI definition in Equation (4.19) as the PCA-DRE-based method. Substituting Equation (4.23) into Equation (4.19), the DI of the Gaussian-PDF-based method, denoted as $\mathrm{DI}_{\mathrm{Gaussian}}$, becomes

$$\mathrm{DI}_{\mathrm{Gaussian}} = \frac{1}{2n_r}\sum_{m=1}^{n_r}\left(\ln \frac{\det(\mathbf{C}_{0,m})}{\det(\mathbf{C}_1)} - d + \mathrm{tr}\left(\mathbf{C}_{0,m}^{-1}\mathbf{C}_1\right)\right) \tag{4.24}$$

To make a fair comparison, the parameter of the Gaussian-PDF-based method, $d$, is optimized by maximizing the ROC-AUC. For the experimental nonlinear beam, $d = \{10, 15, \cdots, 120\}$ were studied and $d = 100$ was selected. For the OWT, the optimum $d = 160$ was chosen from $d = \{10, 20, \cdots, 300\}$. The optimal values of $d$ were then used for damage detection. The obtained ROC-AUC values are compared with the PCA-DRE-based method with different metrics, as shown in table 4.1 for the experimental nonlinear beam and table 4.3 for the OWT. The ROC-AUC comparisons are also plotted in Figure 4.17. It can be seen that the PCA-DRE-based method has consistently better performance than the Gaussian-PDF-based method in both examples, demonstrating the effectiveness of the PCA-DRE-based method.

## 4.7 Conclusion

In this chapter, a damage detection method for an initially nonlinear system is proposed. The vibration response from a signal sensor is characterised by the multivariate PDF.

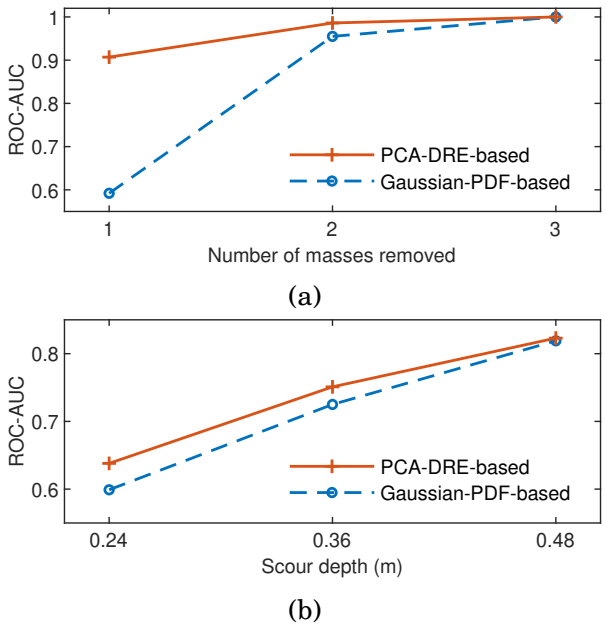


Figure 4.17: Comparison of the ROC-AUCs obtained with the proposed PCA-DRE-based method and the Gaussian-PDF-based method, for different damage levels: (a) for the experimental nonlinear beam and (b) for the OWT.

The damage is detected by monitoring the difference, measured by the KL divergence, between the PDF of the undamaged state and that of a potentially damaged state. The density ratio estimation method, which directly estimates the difference of the PDFs, is applied, along with PCA, which reduces the dimensionality of the PDF. The number of PCs retained is proposed to be determined by using the cumulative percentage of total variance rule and the scree graph rule sequentially, while the sequence length used is suggested to correspond to around 1 to 1.6 times the first natural period of the structure. The effectiveness of the proposed method is demonstrated using two case studies: an experimental nonlinear beam and an offshore wind turbine with scour. In both cases, the proposed method has successfully detected the damage even though the PSDs of the undamaged and damaged states are very similar. Compared with the Gaussian-PDF-based method, which only considers the second-order statistical information, the proposed method performs consistently better due to involving higher-order statistical information, which is relevant to nonlinear structures. Therefore, the proposed method appears to be promising for the output-only vibration-based damage detection problem of initially nonlinear structures.

Although the results are promising, further studies are needed to improve the performance of the model. In this study, environmental and operational conditions were

assumed to be similar for the undamaged state and a potentially damaged state. In future work, a more realistic scenario with environmental and operational variations should be considered. In addition, testing the performance of the optimised parameters on slightly different structures and different damages will be an interesting topic.

CHAPTER 5

# A New Approach to Remove Environmental and Operational Variations

One of the biggest challenges for vibration-based damage detection is ensuring that methods are robust to environmental and operational variations (EOVs). These EOVs can significantly alter the dynamic response features and often mask subtle changes in the vibration signals caused by damage. In the Chapter 3 and Chapter 4, the EOVs were assumed to be similar for the undamaged state and a potentially damaged state. This requires a record of the vibration responses of all possible EOVs, resulting in a heavy data storage burden. The recording can even be impossible for complex systems, such as offshore wind turbines, or extreme EOVs. Therefore, this chapter proposes a method to remove the effects of EOVs.

---

This chapter is adapted from the manuscript:

Zhang Y., Macdonald J.H.G., Liu S., Harper P. (2021). Vibration-based damage detection of offshore wind turbine foundations - a new approach to remove environmental and operational variations. Manuscript in preparation.

Part of the introduction has been removed and included in Chapter 2 - Literature Review.

## Authors' contributions

Zhang Y. conceived the idea, performed the numerical simulations, and implemented the method, with supervisory support from Macdonald J.H.G. on the development of the idea, and input from Liu S. on the mathematical model. All authors contributed to the preparation of the manuscript.

## 5.1 Introduction

Offshore wind power, as one of the most promising renewable energy sources, has become a rapidly developing industry worldwide. However, the cost of offshore wind energy generation is in general higher compared to fossil-fuel-based energy sources. For the wind industry to survive in competition with conventional energy resources, it is crucial that the costs are significantly reduced for future projects. Detecting damage of offshore wind turbines (OWTs) in the early stage can contribute significantly towards reducing the costs, by optimising maintenance scheduling and eliminating unexpected catastrophic failures.

One major damage type for OWT foundations is scour. Unexpected scour damage may be caused by extreme events, strong currents as well as failures of scour protection. Scouring can reduce the natural frequencies of the OWT; studies have shown that the first natural frequency of an OWT with a monopile foundation can be reduced by $5\% - 10\%$ (Devriendt et al., 2014; Prendergast et al., 2015). This reduction leads to a critical problem for foundation integrity. This is because the reduced first natural frequency becomes closer to the wave and gust spectrum peaks, resulting in more resonant effects. In addition, the reduced higher natural frequencies might coincide with some of the higher-order rotor harmonics such as 3P and 6P. Both effects increase resonant behaviour and thus fatigue damage (Devriendt et al., 2014). Therefore, continuously monitoring the scour and foundation integrity is of great importance for reducing costs and extending the lifetime of OWTs.

Various methods have been proposed for scour monitoring, although mainly for bridges (Prendergast and Gavin, 2014). These methods mostly use underwater instrumentation such as buried devices, radar and sonar, leading to a high installation and maintenance cost (Prendergast and Gavin, 2014). The cost can become even higher for OWTs, as a result of the harsh environment and difficult access to the OWT sites. On the other hand, vibration-based methods, which rely on mature and reasonably low-cost signal measurement and acquisition technologies, have attracted more and more interest for scour monitoring of OWTs (Weijtjens et al., 2016; Samusev et al., 2019). The underlying idea of vibration-based damage detection methods is that damage will change the physical properties of the structure and, consequently, change the measured vibration response of the structure.

One of the biggest challenges for vibration-based damage detection is tackling environmental and operational variations (EOVs) (Sohn, 2007). These EOVs can significantly

alter the dynamic response features and often mask subtle changes in the vibration signals caused by damage. For example, the first three modal frequencies of the Alamosa Canyon Bridge in southern New Mexico were reported to vary with temperature by approximately 4.7%, 6.6% and 5.0% over a 24-hour period (Cornwell et al., 1999). Similarly, the Ting Kau Bridge in Hong Kong experienced 6.7% and 1.7% of the 1st and 8th natural frequency changes, respectively, when the temperature varies from 3 °C to 53 °C through a year (Zhou et al., 2010). These effects may mask the vibration response change caused by structural damage, and therefore must be removed before inferring damage.

Numerous methods for removing the EOV effects have been proposed, as discussed in Section 2.1.3. These methods have also been applied to wind turbines, especially for blades of onshore wind turbines. Hu et al. (2015) removed temperature effects on modal frequencies of blades and towers of an onshore wind turbine using numerical data. Movsessian et al. (2021) studied experimental data from a real-world wind turbine and applied ANN to remove the EOV effects on the vibration response of the blades, although the rotation speed is fixed. Based on the same wind turbine but considering more operational conditions, Avendaño-Valencia et al. (2020) applied a cause-effect method to remove the EOV effects from wind speed, turbulence intensity and ambient temperature. The key idea is replacing the autoregressive model coefficients with a function of the EOV parameters. A more realistic study was conducted by Chandrasekhar et al. (2021), where the data is from operational wind turbines. More importantly, they proposed to remove the EOV effects by viewing the natural frequencies of the blades relative to each other because the blades are subjected to the EOVs simultaneously. To the best of the authors' knowledge, only the work from Weijtjens et al. (2016) concerned about the removal of EOV effects on OWT foundations. In their work, the operational states of OWTs were first divided into eight cases according to the pitch angles and rotational speeds. For each case, a nonlinear regression model was developed with wave height, yaw angle sea water temperature, and tidal level as inputs and a selected modal frequency as output. The yaw angle, and many other parameters like pitch angle, revolutions per minute and output power, can be provided by the supervisory control and data acquisition (SCADA), which is normally available for wind turbines throughout their lifetime. However, the other parameters related to sea states have to be measured with extra equipment which may not be available or expensive to maintain. Therefore, it is desirable to apply effect-only methods for OWT foundations.

In this chapter, a new effect-only approach to remove the EOV effects is proposed. This approach takes advantage of the fact that OWTs are built in groups and thus subjected to

similar EOVs at the same time. When the monitored features are viewed relative to each other, the complex EOV effects are probably cancelled out. Specifically, the relationships between the features of adjacent OWTs are modelled using Gaussian process regression (GPR) (Bishop, 2006). The regression models are then used for predictive purposes, and the residuals between the actual features and predicted features are monitored in X-bar control charts for damage detection. It should be noted that these OWTs are not necessarily identical; their water depths, soil conditions and foundation stiffness may be different to each other.

In the remainder of the chapter, the problem setting and the key ideas are presented in Section 5.2, followed by the introduction of the methodology in Section 5.3. The OWTs and signals are described in Section 5.4. The results are shown in Section 5.5. Finally, the main conclusions are presented in Section 5.6.

## 5.2 Brief description of the Problem setting and key ideas

Consider an offshore wind farm with dozens of monopile OWTs, where the monopiles are of different sizes due to variations in the water depth and soil condition. The OWTs are subjected to various EOVs, but the measurements of the EOVs are not fully available because of lack of sensors, sensor failure or missing data. Acceleration signals at the tower top are available, which can be used to extract features. As scouring can reduce OWT lifetime as described in Section 5.1, the aim is to detect scour damage under the EOV effects.

The key idea of the proposed method is removing the EOV effects by studying the relationship between features from adjacent structures, rather than the relationship between the feature of a structure and the EOVs as in the traditional way. As illustrated in Figure 5.1, the wind farm is represented by a graph consisting of nodes and links, where the nodes represent OWTs and the links represent the relationships between the features from two adjacent OWTs. The change of the link (i.e., relationship) will indicate property change in one or both of the corresponding nodes (i.e., OWTs). It is worth noting that the method can be extended to study the relationship between the features of an OWT and the features of multiple OWTs to enhance the damage detection performance.

There are mainly three steps for the damage detection method:

1. Feature extraction: extract features from acceleration time-series by automated

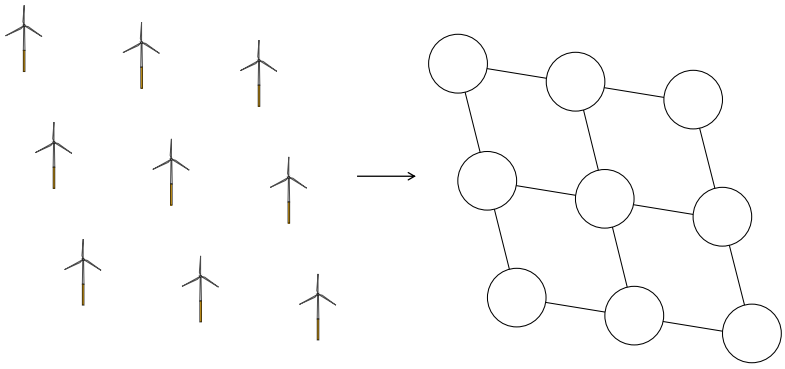

Figure 5.1: Wind farm (left) and its representation (right). In the representation, each node represents an OWT and each link represents the relationship between the features from two adjacent OWTs.

operational modal analysis (OMA) for each OWT in the wind farm;

2. Model development: train GPR model based on the features of two adjacent OWTs and obtain the prediction residuals;

3. Damage diagnosis: plot X-bar control charts of the GRP prediction residuals for damage detection.

The theories underlying these steps are introduced in Section 5.3.

## 5.3 Theories

As mentioned above, the proposed method consists of an automated OMA, GPR model and X-bar control chart. These techniques will be described in this section.

### 5.3.1 Automated operational modal analysis

Automated OMA is used to extract features from the acceleration time series of OWTs. Identification of modal parameters for OWTs is challenging. Traditional experimental modal analysis methods are not applicable because the input loads due to wind and waves are immeasurable. Therefore, a method which estimates the modal parameters just based on the output responses, i.e. OMA, has to be used.

OMA works under the assumption that the system is linear time-invariant during the analysed time interval. For structural analysis of OWT towers and foundations, the main source of nonlinearity is the soil stiffness. However, due to the OWT is parked

and thus has limited response magnitudes, the soil stiffness can be seen as linear. Also, the parked condition means the pitch angle does not change and the system is time-invariant (Devriendt et al., 2013). Hence, the linear time-invariant assumption is satisfied and OMA is applicable.

Various OMA methods are available in the literature (Rainieri and Fabbrocino, 2014). Among these methods, the poly-reference least squares complex frequency-domain estimator (p-LSCF) method is popular as it provides very clear stabilisation charts (Guillaume et al., 2003). A stabilisation chart plots the poles obtained for different model orders. It is used to separate spurious poles from the physical poles by comparing the results of models with different order. Specifically, the spurious mathematical poles tend to be scattered and typically not stable, while the physical poles are more stable. By observing the stabilisation of the poles for increasing model orders, the physical modes can be identified from alignments of stable poles (Rainieri and Fabbrocino, 2014).

Normally, the poles in the stabilisation chart are manually selected according to the user's expertise. However, SHM is used to automatically monitor the state of structures. It inherently requires the OMA to be automated. Several studies have addressed this problem (Verboven et al., 2002; Magalhaes et al., 2009). In this paper, a clustering method based on Devriendt et al. (2014) is used. Specifically, the method clusters the stable poles according to two criteria: (1) a new pole is added to an initiated cluster if it is within the 1% interval of the mean frequency of the cluster. (2) a cluster is withdrawn if it has a less than 25% identification success rate, which is calculated by dividing the number of poles in each cluster by the maximum number of poles a cluster can contain. After the clustering, the mean of the poles in each cluster is used as the modal frequencies.

The feature is selected to be natural frequencies of the second side-side mode (SS2) as in Devriendt et al. (2014) and Weijtjens et al. (2016). The frequencies of SS2 of monopile-supported OWT are more sensitive to scour because the SS2 have a larger relative motion at the seabed in comparison with the first bending modes (Devriendt et al., 2014).

### 5.3.2 Gaussian process regression

GPR is a non-parametric Bayesian approach (Rasmussen, 2003) which can capture a wide variety of relations between inputs and outputs, and has been used in many SHM applications (Teimouri et al., 2017; Avendaño-Valencia et al., 2020; Chandrasekhar et al., 2021).

Given a training dataset consisting of $N$ pairs of observations:

$$\mathscr{D}_{\text{train}} = (\mathbf{X}, \mathbf{y}) = \{\mathbf{x}_i, y_i\}_{i=1}^{N},\ \mathbf{x}_i \in \mathbb{R}^d,\ y_i \in \mathbb{R} \tag{5.1}$$

where $d$ is the dimensionality of $\mathbf{x}_i$, and a testing dataset of $N^*$ points:

$$\mathscr{D}_{\text{test}} = \mathbf{X}^* = \{\mathbf{x}_{i^*}^*\}_{i^*=1}^{N^*},\ \mathbf{x}_{i^*}^* \in \mathbb{R}^d \tag{5.2}$$

GPR is used to learn the relationship, denoted as $g(\cdot)$, between $\mathbf{x}_i$ and $y_i$ based on the training dataset, and then predict the target, denoted as $y_{i^*}^*$ at a testing point $\mathbf{x}_{i^*}^*$ via $g(\cdot)$.

In the context of this chapter, $\mathbf{x}_i$ can be the natural frequencies of multiple orders from one OWT and $y_i$ can be the natural frequency of one order from another OWT in the same wind farm. This will be further illustrated in Section 5.5.2, where $\mathbf{x}_i$ is reduced to a scale as only one natural frequency is used.

#### 5.3.2.1 Gaussian process regression modelling

The GPR model is expressed as

$$y_i = g(\mathbf{x}_i) + \epsilon_i \tag{5.3}$$

where $\epsilon_i$ is the noise representing uncertainty due to factors external to $\mathbf{x}_i$, such as measurement noise. It is assumed that $\epsilon_i \sim \mathscr{N}(0, \sigma_n^2)$, where $\sigma_n^2$ is the variance of the noise, and $\epsilon_i$ is independent to $g(\mathbf{x}_i)$.

The function $g(\cdot)$ has a prior which is assumed to follow a Gaussian process (GP)

$$g(\mathbf{x}) \sim \mathscr{GP}(m(\mathbf{x}), k(\mathbf{x}, \mathbf{x}')) \tag{5.4}$$

where $\mathbf{x}$ and $\mathbf{x}'$ are two arbitrary points in $\mathbb{R}^d$, $m(\mathbf{x})$ is the mean function, and $k(\mathbf{x}, \mathbf{x}')$ is the covariance function, i.e.,

$$\begin{aligned} m(\mathbf{x}) &= \mathbb{E}[g(\mathbf{x})] \\ k(\mathbf{x}, \mathbf{x}') &= \mathbb{E}[(g(\mathbf{x}) - m(\mathbf{x}))(g(\mathbf{x}') - m(\mathbf{x}'))] \end{aligned} \tag{5.5}$$

where $\mathbb{E}[\cdot]$ represents expectation.

Therefore, the random variables $\{g(\mathbf{x}_i)\}_{i=1}^{N}$, denoted as $\mathbf{g}$ for convenience, at the training data $\mathbf{X} = \{\mathbf{x}_i\}_{i=1}^{N}$, have a joint Gaussian prior distribution,

$$p(\mathbf{g}|\mathbf{X}) = \mathscr{N}(\mu, \mathbf{K}) \tag{5.6}$$

where the mean $\mu = [m(\mathbf{x}_1), m(\mathbf{x}_2), \ldots, m(\mathbf{x}_N)]^\top \in \mathbb{R}^{N\times d}$ (the superscript $\top$ denotes transpose), the covariance matrix $\mathbf{K} \in \mathbb{R}^{N\times N}$ consists of the $i$-$j$th entry $\mathbf{K}_{ij} = k(\mathbf{x}_i, \mathbf{x}_j)$, and $1 \leq i, j \leq N$.

The mean function $m(\mathbf{x})$ of the prior GP is normally assumed to be zero for simplicity; hence, $\mu = \mathbf{0}$. However, this does not imply that the mean function of the posterior is zero, because it will be updated according to the training data using Bayes' theorem (Chandrasekhar et al., 2021). That will be evidenced in Equation (5.14).

There are various covariance functions. This chapter applies one of the most commonly used functions, the squared exponential covariance function,

$$k_{\mathrm{SE}}(\mathbf{x}_i, \mathbf{x}_j) = \sigma_g^2 \exp\left(-\frac{(\mathbf{x}_i - \mathbf{x}_j)^\top (\mathbf{x}_i - \mathbf{x}_j)}{2\lambda^2}\right) \tag{5.7}$$

where $\sigma_g^2$ is a signal variance and controls the vertical scale of the function, and $\lambda$ is a length-scale and reflects how smooth the function appears. Along with the noise variance $\sigma_n^2$ from Equation (5.3), the three hyper-parameters $\{\sigma_g, \lambda, \sigma_n\}$ are grouped together as a vector $\theta$, which will be estimated using $\mathscr{D}_{\mathrm{train}}$ with the method discussed in Section 5.3.2.2.

#### 5.3.2.2 Hyper-parameter estimation

In statistics, parameters can usually be estimated by maximising a likelihood function (i.e., maximum likelihood estimation). Following this line, one possible likelihood function in GPR is $p(\mathbf{y}|\mathbf{g}) = \mathcal{N}(\mathbf{g}, \sigma_n^2 \mathbf{I})$, where $\mathbf{I} \in \mathbb{R}^{N\times N}$ is an identity matrix. However, it contains unknown $\mathbf{g}$, making the estimation of the hyper-parameter $\theta$ impossible. Therefore, the marginal likelihood

$$p(\mathbf{y}|\mathbf{X}) = \int p(\mathbf{y}|\mathbf{g}) p(\mathbf{g}) \, \mathrm{d}\mathbf{g} \tag{5.8}$$

which marginalises the likelihood $p(\mathbf{y}|\mathbf{g})$ over $\mathbf{g}$ to eliminate $\mathbf{g}$, is used for the hyper-parameter estimation.

Considering $p(\mathbf{g}|\mathbf{X}) = \mathcal{N}(\mathbf{0}, \mathbf{K})$ as indicated by Equation (5.6), the marginal likelihood yields (Rasmussen, 2003)

$$p(\mathbf{y}|\mathbf{X}) = \mathcal{N}(\mathbf{0}, \mathbf{K}_y) \tag{5.9}$$

where $\mathbf{K}_y = \mathbf{K} + \sigma_n^2 \mathbf{I}$. For computational convenience, the natural logarithm of $p(\mathbf{y}|\mathbf{X})$ is used, resulting in the log-marginal likelihood function

$$\begin{aligned} \mathscr{L}(\theta) &= \log p(\mathbf{y}|\mathbf{X}) \\ &= \log\left[(2\pi)^{-\frac{N}{2}} |\mathbf{K}_y|^{-\frac{1}{2}} \exp\left(-\frac{1}{2}\mathbf{y}^\top \mathbf{K}_y^{-1}\mathbf{y}\right)\right] \\ &= -\frac{1}{2}\mathbf{y}^\top \mathbf{K}_y^{-1}\mathbf{y} - \frac{1}{2}\log|\mathbf{K}_y| - \frac{N}{2}\log(2\pi) \end{aligned} \tag{5.10}$$

The three terms in the bottom line of Equation (5.10) have readily interpretable roles (Rasmussen, 2003): $-\mathbf{y}^\top \mathbf{K}_y^{-1}\mathbf{y}/2$ is the data-fit term, $-\log|\mathbf{K}_y|/2$ is the model complexity penalty term, and $-N\log(2\pi)/2$ is the normalisation constant.

The hyper-parameter vector $\theta$ is estimated by maximising $\mathscr{L}(\theta)$. The maximisation is achieved by gradient descend, which relies on the partial derivatives

$$\frac{\partial \mathscr{L}(\theta)}{\partial \theta_l} = \frac{1}{2}\mathbf{y}^\top (\mathbf{K}_y)^{-1} \frac{\partial \mathbf{K}_y}{\partial \theta_l} \mathbf{K}_y^{-1}\mathbf{y} - \mathrm{tr}\left(\mathbf{K}_y^{-1}\frac{\partial \mathbf{K}_y}{\partial \theta_l}\right) \tag{5.11}$$

where $\theta_l$ represents an element in $\theta$.

#### 5.3.2.3 Prediction with Gaussian process regression

Once that $\theta$ is known, the GPR model can be used to predict the targets $\{y_{i^*}^*\}_{i^*=1}^{N^*}$, denoted as $\mathbf{y}^*$, at the testing points $\mathbf{X}^* = \{\mathbf{x}_{i^*}^*\}_{i^*=1}^{N^*}$.

Similar to Equation (5.6), the random variables $\{g(\mathbf{x}_{i^*}^*)\}_{i^*=1}^{N^*}$, denoted as $\mathbf{g}^*$, have a joint Gaussian distribution,

$$p(\mathbf{g}^*|\mathbf{X}^*) = \mathscr{N}(\mathbf{0}, \mathbf{K}^{**}) \tag{5.12}$$

where the covariance matrix $\mathbf{K}^{**}$ consists of the $i^*$-$j^*$th entry $\mathbf{K}_{i^*j^*}^{**} = k(\mathbf{x}_{i^*}^*, \mathbf{x}_{j^*}^*)$, and $1 \le i^*, j^* \le N^*$. Based on Equation (5.9) and (5.12), the joint distribution of $\mathbf{y}$ and $\mathbf{g}^*$ is given by

$$\begin{bmatrix} \mathbf{y} \\ \mathbf{g}^* \end{bmatrix} \sim \mathscr{N}\left(\mathbf{0}, \begin{bmatrix} \mathbf{K}_y & \mathbf{K}^* \\ (\mathbf{K}^*)^\top & \mathbf{K}^{**} \end{bmatrix}\right) \tag{5.13}$$

where the covariance matrix $\mathbf{K}^* \in \mathbb{R}^{N \times N^*}$ consists of the $i$-$i^*$th entry $\mathbf{K}_{ii^*}^* = k(\mathbf{x}_i, \mathbf{x}_{i^*}^*)$. By the standard rules for conditioning Gaussians, the posterior (Murphy, 2012)

$$p(\mathbf{g}^*|\mathbf{X}^*, \mathbf{X}, \mathbf{y}) = \mathscr{N}(\mu_{\mathbf{g}^*}, \Sigma_{\mathbf{g}^*}) \tag{5.14}$$

where $\mu_{\mathbf{g}^*} = (\mathbf{K}^*)^\top (\mathbf{K}_y)^{-1}\mathbf{y}$, and $\Sigma_{\mathbf{g}^*} = \mathbf{K}^{**} - (\mathbf{K}^*)^\top \mathbf{K}_y{}^{-1}\mathbf{K}^*$.

Similar to Equation (5.3), it is obtained that $y_{i^*}^* = g(\mathbf{x}_{i^*}^*) + \epsilon_{i^*}$. Hence,

$$\mathbf{y}^* = \mathbf{g}^* + \epsilon^*,\ \epsilon^* \sim \mathcal{N}(\mathbf{0}, \sigma_n^2 \mathbf{I}^*) \tag{5.15}$$

where $\epsilon^*$ is the noise, and $\mathbf{I}^* \in \mathbb{R}^{N^* \times N^*}$ is an identity matrix.

Considering $\epsilon^*$ being independent of $\mathbf{g}^*$, their means and covariance matrices can be added respectively to obtain the distribution of $\mathbf{y}^*$,

$$p(\mathbf{y}^* | \mathbf{X}^*, \mathbf{X}, \mathbf{y}) = \mathcal{N}(\mu_{\mathbf{y}^*}, \Sigma_{\mathbf{y}^*}) \tag{5.16}$$

where $\mu_{\mathbf{y}^*} = (\mathbf{K}^*)^\top (\mathbf{K}_y)^{-1} \mathbf{y} \in \mathbb{R}^{N^*}$, $\Sigma_{\mathbf{y}^*} = \mathbf{K}^{**} - (\mathbf{K}^*)^\top {\mathbf{K}_y}^{-1} \mathbf{K}^* + \sigma_n^2 \mathbf{I}^* \in \mathbb{R}^{N^* \times N^*}$.

### 5.3.3 Control chart

Based on the GPR model, the prediction residuals are calculated by subtracting the actual frequencies from the predicted frequencies and plotted in X-bar control charts to detect the damage.

Control charts are an online monitoring technique used for detecting anomalies in a process (Montgomery, 2007). It plots a statistic of the process over time, along with two horizontal lines: lower control limit (LCL) and upper control limit (UCL). These control limits are chosen so that if the process is in control (i.e., the structure is undamaged), nearly all of the sample points will fall between them. However, a point that plots outside of the control limits indicates that the process is out of control (i.e., the structure is damaged), and an alarm will be triggered.

Control charts have various statistics and rigorously derived control limits. In addition, it inherently provides an automatic and online method for structural health monitoring. Due to these reasons, they have been applied in many studies for damage detection of civil infrastructure. For example, Fugate et al. (2001) showed that applying control charts in conjunction with auto-regressive models can detect progressive damage of a concrete bridge. Kullaa (Kullaa, 2003) applied various control charts of modal parameters for the damage detection of the Z24 Bridge in Switzerland. More recently, Chandrasekhar et al. (2021) used an X-bar chart of the residuals between the GPR predictions and actual frequencies for damage detection of wind turbine blades. In this chapter, the commonly used X-bar control chart (Montgomery, 2007) is applied.

In the X-bar control chart, the prediction residuals for an OWT, denoted as $r$, are divided into $m$ subgroups, each of size $n$. Let $r_{pq}$ represent the residual value of the $q$th sample of the $p$th subgroup. The monitored statistics (i.e., points on the chart) are the

mean of the $p$th subgroup

$$\bar{r}_p = \sum_{q=1}^{n} r_{pq}/n \tag{5.17}$$

The estimated mean of $\bar{r}_p$ is $\bar{\bar{r}} = \sum_{p=1}^{m} \bar{r}_p/m$, and the estimated standard deviation of $\bar{r}_p$ is $\bar{s}/(c_4\sqrt{n})$, where $c_4$ is a constant that depends on the subgroup size $n$ and its value can be found in Montgomery (Montgomery, 2007). The UCL and LCL of the corresponding X-bar chart are defined as,

$$\begin{aligned} \text{UCL} &= \bar{\bar{r}} + 3\bar{s}/(c_4\sqrt{n}) \\ \text{LCL} &= \bar{\bar{r}} - 3\bar{s}/(c_4\sqrt{n}) \end{aligned} \tag{5.18}$$

For each OWT, an X-bar control chart is plotted. The corresponding UCL and LCL are calculated when the structure is undamaged. During monitoring, a point plots outside the limits indicates damage. The overall steps of the proposed method are illustrated in Figure 5.2.

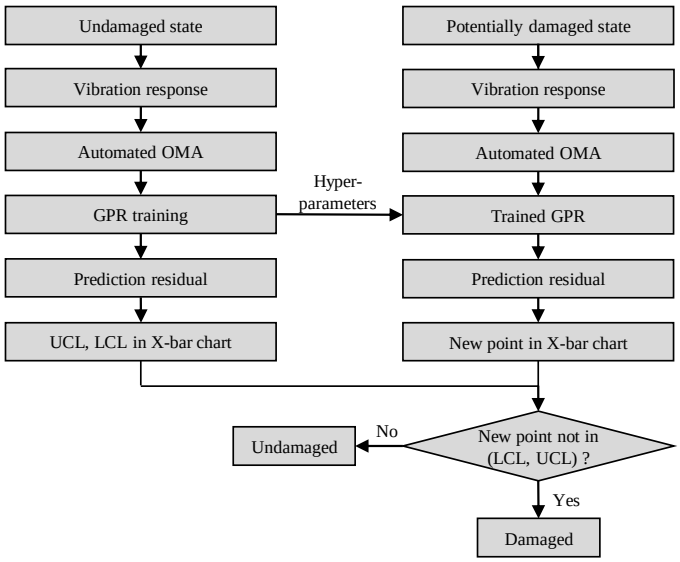


Figure 5.2: Flowchart of the proposed method

## 5.4 Simulation of a three-OWT wind farm

This section presents the simulation of an offshore wind farm consisting of three OWTs, which are denoted as OWT 1, OWT 2, and OWT 3. The offshore wind farm will be used to demonstrate the proposed method in Section 5.5.

A widely used baseline OWT is the National Renewable Energy Laboratory (NREL) 5 MW baseline wind turbine (Jonkman et al., 2009) with a monopile foundation in a water depth of 20 m. The monopile profile and soil properties are available in Jonkman et al. (2008a). Figure 5.3 gives an overview of the OWT, and Table 5.1 summarises the details on the properties of the tower and monopile. As an initial study, some simplifications were made for the OWTs. First, the OWTs were set as parked (the rotor was in a standstill condition). A mild turbulent wind and irregular wave condition was applied to the OWT in the fore-aft direction. The wind has a mean speed of 3 m/s and corresponding turbulence intensities determined according to IEC 61400-1 (2010) under high turbulence. The wave is generated from a Pierson-Moskowitz spectrum with a significant wave height of 1.64 m and peak spectral period of 12.7 s, which have been used in Zhao et al. (2012).

For a wind farm, the seabed has a topography. Hence, the water depth for different OWT may vary. To reflect that, a distinct water depth of 25 m is applied to OWT 3, with OWT 1 and OWT 2 remain in 20 m of water. Table 5.2 shows the mean sea level for each OWT, as well as the tide levels, which will be discussed in Section 5.4.1.

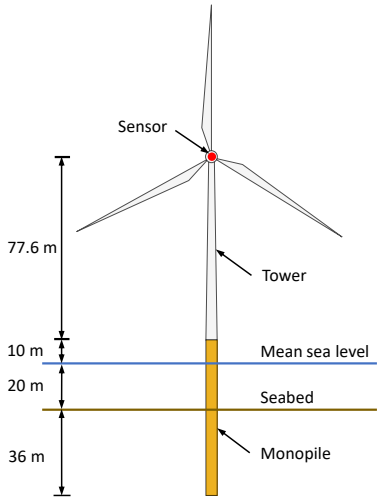


Figure 5.3: Overview of the OWT.

Table 5.1: Main properties of the tower and monopile (Jonkman et al., 2009, 2008a)

| **Property** | **Value** |
|---|---|
| Tower top diameter, wall thickness | 3.87 m, 0.019 m |
| Tower base diameter, wall thickness | 6.00 m, 0.027 m |
| Monopile diameter, wall thickness | 6.00 m, 0.060 m |
| Density | 8500 kg/m$^3$ |
| Young's modulus | 210 GPa |
| Shear modulus | 80.8 GPa |
| Damping ratio (all modes) | 1% |

Table 5.2: Water depths and tide level ranges for OWTs

| Structure | Water depth (m) | Tide level range (m) |
|---|---|---|
| OWT 1 | 20 | $-4.8 \sim 5$ |
| OWT 2 | 20 | $-4.8 \sim 5$ |
| OWT 3 | 25 | $-4.8 \sim 5$ |

### 5.4.1 Environmental variation

For parked OWTs, the operational variations do not exist, and the environmental variations are mainly caused by tide level, wave height, wave period, current velocity, and temperature. Temperature has been reported to significantly affect natural frequencies of civil structures such as bridges (Farrar and Worden, 2012; Sohn, 2007; Sohn et al., 1999) and wind turbine blades (Hu et al., 2015; Chandrasekhar et al., 2021), but this is not the case for OWT foundations, as reported in Weijtjens et al. (2016). This can be explained by the fact that OWT foundations mainly consist of steel, while bridges normally consist of asphalt and concrete and wind turbine blades comprise composite materials. Therefore, the temperature is an insignificant EOV parameter for OWT foundations and is ignored.

In contrast, tide levels and wave heights have a significant effect on the natural frequencies. They were found to be the two factors that most correlated to the frequencies of an OWT in the Belwind wind farm located 46 km outside the Belgian coast (Weijtjens et al., 2016). Hence, tide levels and wave heights should be considered to make the simulation realistic. However, jointly considering tide level and wave height results in a cumbersome simulation workload. In fact, tide levels and wave heights affect the natural frequencies in the same mechanics, i.e., changing added mass. Therefore, only the tide level was considered to represent the effects from both tide levels and wave heights in this chapter for simplicity.

The tide levels used in this chapter are the real-time data at Ilfracombe, UK, which

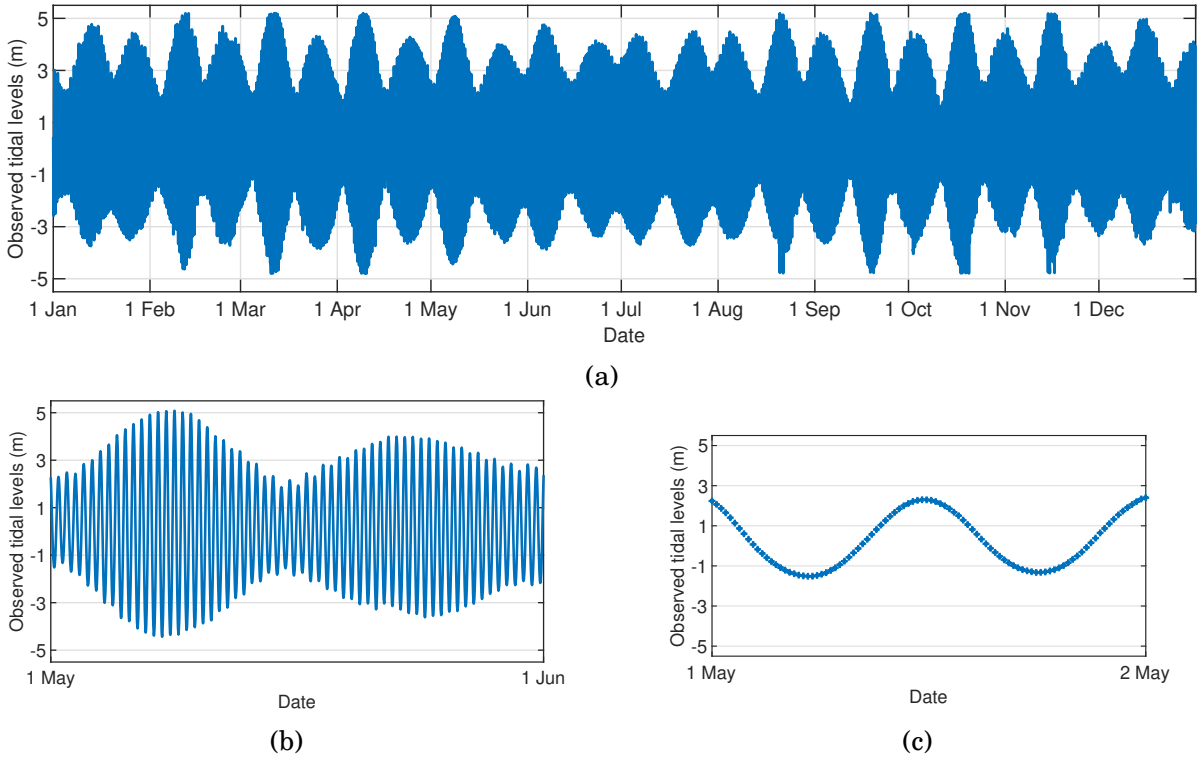


Figure 5.4: Observed tidal levels at Ilfracombe, UK, in 2020 during: (a) one year; (b) one month and (c) one day. Each star in (c) represents a quarter-hourly record.

are available in British Oceanographic Data Centre (British Oceanographic Data Centre, 2021). The tidal levels are given as a height above chart datum at Ilfracombe, which is 4.8 m below Ordnance Datum Newlyn. As Ordnance Datum Newlyn is the mean sea level used at Great Britain (Bradshaw et al., 2016), the tidal levels can be converted to be relative to the mean sea level by subtracting 4.8 m. The data were recorded every 15 minutes. The typical tide levels in one year, one month and one day are shown in Figure 5.4.

The wave loads in Bladed are calculated by the Morison's equation (Morison et al., 1950), where the hydrodynamic force is separated into an inertia force and a drag force. The inertia force per unit length, $F_{\text{inertia}}$, of an oscillating cylinder in flows, is (Journée and Massie, 2001)

$$F_{\text{inertia}} = 1 \cdot M_D \cdot \dot{u}_p(t) + C_a M_D \cdot \dot{u}_p(t) - C_a M_D \cdot \ddot{X}(t) \tag{5.19}$$

where $M_D$ is the displaced water mass per unit length, $C_a$ is the coefficient of added mass, $\dot{u}_p(t)$ is the perpendicular acceleration component from the waves, and $\ddot{X}(t)$ is the cylinder acceleration; hence $C_a M_D$ can be seen as an equivalent mass per unit length

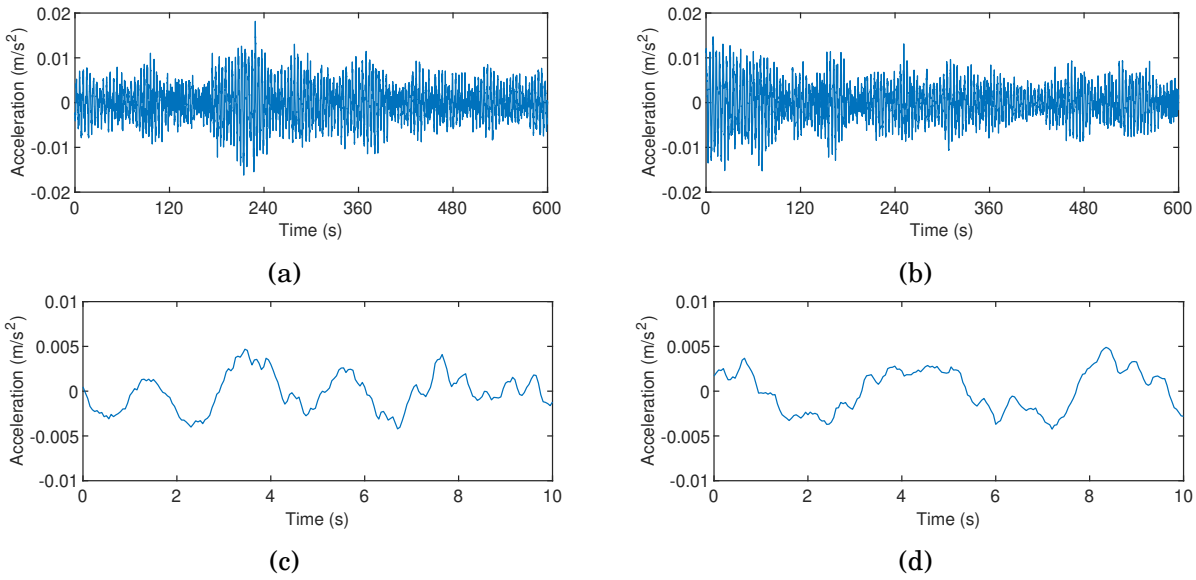


Figure 5.5: Typical acceleration time series in the side-side direction from OWT 1 at the tide level of 0 m in: (a) the undamaged state; (b) the damaged state; (c,d) are zoomed views of the first 10s corresponding to (a,b), respectively.

which is added to the cylinder segment. In the case of this paper, the changing tidal level decides the length of the monopile submerged in water. Hence the added mass of the whole monopile changes, resulting in a changing natural frequency of the OWT. The tidal level (e.g., one point in Figure 5.4 (c)) can be set directly in Bladed, and then a simulation is conducted to obtain dynamic responses from Bladed and eventually the natural frequencies are obtained using the automated OMA method.

### 5.4.2 Offshore wind turbine simulation and signals

The OWTs were simulated in DNV's Bladed software (DNV, 2020). Bladed is an integrated wind turbine design tool for calculating turbine performance and dynamic loading and response. The monopile structure below the seabed is typically modelled with coupled springs (Jonkman et al., 2008b). Specifically, it was idealised as a stiffness matrix positioned at the seabed. The stiffness values were given by (Passon, 2006) as:

$$\mathbf{K}_{\text{seabed}} = \begin{bmatrix} k_{xx} & 0 & 0 & k_{x\beta} \\ & k_{yy} & k_{y\alpha} & 0 \\ & & k_{\alpha\alpha} & 0 \\ \text{Symmetric} & & & k_{\beta\beta} \end{bmatrix} \tag{5.20}$$

where the horizontal stiffness coefficients $k_{xx} = k_{yy} = 2.57 \times 10^9$ N/m, the rotational stiffness coefficients $k_{\alpha\alpha} = k_{\beta\beta} = 2.63 \times 10^{11}$ N·m/rad, and the coupled stiffness coefficients $k_{x\beta} = -k_{y\alpha} = -2.25 \times 10^{10}$ N/rad.

In this chapter, damage caused by scouring was considered. It was simulated by reducing the stiffness at the seabed. Specifically, all entries of $\mathbf{K}_{\text{seabed}}$ were reduced by 10%. This stiffness reduction is reasonable, as the corresponding first natural frequency reduction is only 1.2%, which is much less than the reported possible 5%-10% frequency reduction (Devriendt et al., 2014; Prendergast et al., 2015).

The accelerations were obtained from a virtual sensor located at the tower top (as shown in Figure 5.3), where various sensors are normally installed in practice. Each record has a period of 10 min. Considering the frequency band of interest, the sampling frequency was set to 20 Hz. In real vibration measurements, noise is inevitable. To account for that, Gaussian white noise was added to the simulated accelerations. The magnitude of the noise was set to achieve a signal-to-noise ratio of 30 dB for each record. Typical acceleration time series at the tower top in the side-side (perpendicular to the axis of the nacelle) direction from OWT 1 at the tide level of 0 m are plotted in Figure 5.5. Figure 5.5 (a) shows a typical 600 s acceleration record for the undamaged state; Figure 5.5 (b) presents a similar record for the damaged state; Figure 5.5 (c,d) show zoomed views of typical 10-s records corresponding to Figure 5.5 (a,b), respectively.

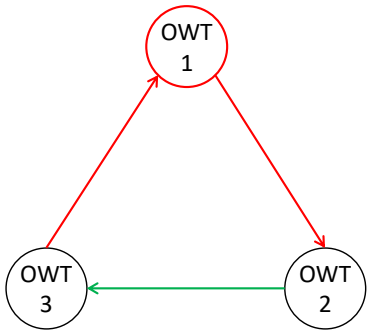


Figure 5.6: The relationships between OWTs in a three-OWT wind farm. Each node represents an OWT and each arrow represents the relationship (modelled by GPR) between features of two OWTs.

Table 5.3: Description of training and testing data

| Data | Date | Structural state | Notation for SS2 |
|---|---|---|---|
| Training | 1 May to 15 May | All undamaged | $f_1, f_2, f_3$ |
| Testing | 16 May to 31 May<br>1 June to 7 June | All undamaged<br>Only OWT 1 damaged | $f_1^*, f_2^*, f_3^*$ |

## 5.5 Application to the three-OWT wind farm

For the purpose of demonstrating the key idea of the proposed method, the simplified wind farm of three OWTs described in Section 5.4 are studied, and the results are shown in this section.

Similar to Figure 5.1, the three-OWT wind farm can be represented by the graph in Figure 5.6, where each node represents an OWT, and each arrow represents the relationship (modelled by GPR) between the features of two OWTs. As an example, the arrow between OWT 3 and OWT 1 indicates a GPR model with inputs from features of OWT 3 and outputs from features of OWT 1. The proposed method detects damage by monitoring the change of the relationship. The arrows are marked in different colours, which will be explained in Section 5.5.3.

For the demonstration, the acceleration time series from 1 May to 7 June were used. They were divided into three periods for training and testing the proposed method. The time series from 1 May to 15 May were used for training, and all OWTs were undamaged; The time series from 16 May to 31 May were used for testing, and all OWTs were undamaged; The time series from 1 June to 7 June were used for testing, and OWT 1 is damaged by scouring as described in Section 5.4.2 while OWT 2 and OWT 3 were undamaged. These training and testing data are further summarised in Table 5.3.

### 5.5.1 Automated operational modal analysis

The first step is extracting the feature, SS2, from each 10-min time series using the automated OMA presented in Section 5.3.1. Figure 5.7 shows an example of the stabilisation diagram using a 10-min time series from OWT 1 at the tide level of 0 m and a maximum model order of 30, along with the power spectral density (shown as the grey line) of the time series. The red circles represent the stable poles, the green circles indicate the unstable poles, and the blue circles on the top indicate the identified physical modes. The analysis focused on the frequency range of 0 ~ 2.5 Hz, where the main vibration

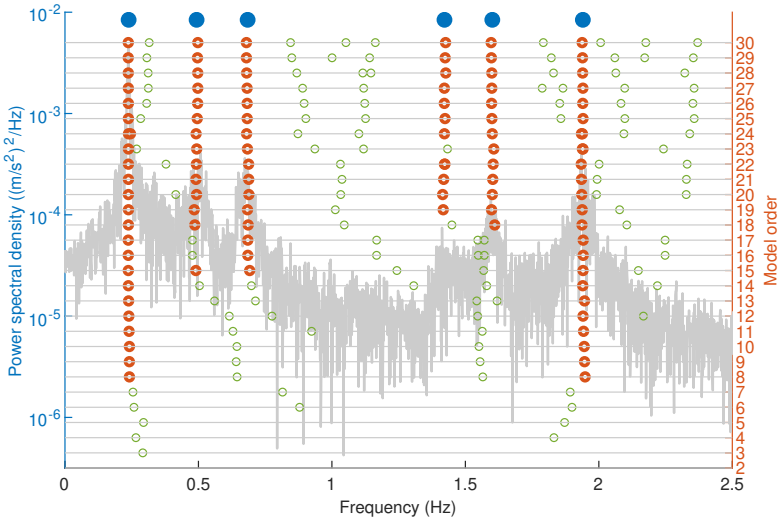


Figure 5.7: Stabilisation chart and power spectral density for 10-min data from OWT 1 at the tide level of 0 m using the p-LSCF estimator. The grey line shows the power spectral density. The red circles represent the stable poles, the green circles indicate the unstable poles, and the blue circles on the top indicate the identified physical modes.

modes of interest are expected (Jonkman et al., 2008a). To plot such a stabilisation chart, first the poles for model orders from 2 to 30 were estimated using the P-LSCF methods. With these poles, the physical poles were identified according to the criteria in Section 5.3.1. After the clustering, the mean of the stable poles in one cluster is used as a natural frequency. In Figure 5.7, the natural frequencies for the identified modes are 0.2385 Hz, 0.4931 Hz, 0.6843 Hz, 1.4217 Hz, 1.6009 Hz, and 1.9401 Hz.

All the natural frequencies except the second one (i.e., 0.4931 Hz) match the results from the built-in modal analysis module in Bladed. The second natural frequency will be discussed subsequently. It is worth noting that the identified modes are coupled modes of the blades, rotor, and tower. The mode shapes of these modes are not available directly in Bladed, but they are described using the contributions of the uncoupled modes of the blades, rotor or tower. For example, the fourth coupled mode (1.4217 Hz) mainly consists of the following uncoupled modes: the tower second side-side mode, the blade 2 first edgewise mode and the blade 3 first edgewise mode (When the OWT is parked, blade 1 is at pointing vertically upward, and blade 2 and blade 3 are the other two blades), and the rotor rigid body mode. These descriptions are summarised in Table 5.4, where only dominant uncoupled modes are shown. As mentioned before, Bladed does not provide the coupled mode shapes directly. However, for illustration purpose, the coupled modes are approximately represented by the superposition of the dominant uncoupled modes.

The sketches of these approximate coupled mode shapes are shown in Figure 5.8. It can be seen that the fourth mode is dominated by the tower second side-side mode. Hence, the SS2 identified from this time series is the fourth natural frequency (i.e., 1.4217 Hz). For a new time series, the obtained natural frequencies are compared to the reference SS2 when the tide level is 0. Since the EOV effects, the SS2 is expected to vary. Hence, if the natural frequency is within a 5% deviation of the expected values, it is identified as a SS2.

Table 5.4: Mode shape descriptions

| Coupled mode | Natural frequencies (Hz) | Dominant uncoupled modes |
|---|---|---|
| 1st | 0.2385 | Tower first side-side mode |
| 2nd | 0.4931 | Drivetrain torsion<br>(High-speed shaft locked by brake) |
| 3rd | 0.6843 | Blade first flapwise modes<br>(blade 2 and 3 out of phase, blade 1 stationary) |
| 4th | 1.4217 | Tower second side-side mode<br>Blade first edgewise modes<br>Rotor rigid body |
| 5th | 1.6009 | Blade second flapwise modes<br>(blade 2 and 3 out of phase, blade 1 stationary) |
| 6th | 1.9401 | Blade second flapwise modes<br>(all blades in phase) |

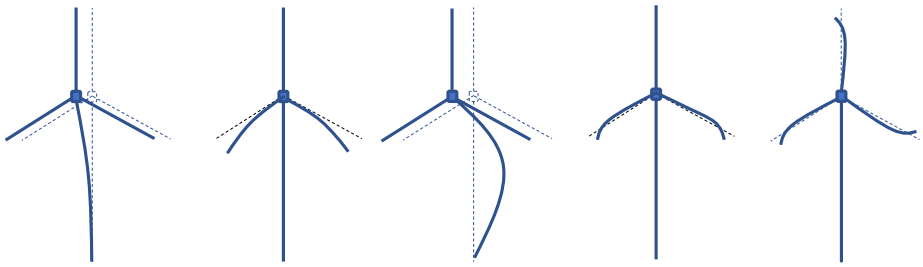

Figure 5.8: Sketches of the approximate coupled mode shapes of the 1st, 3rd, 4th, 5th, and 6th mode (from left to right). Only the dominant uncoupled modes are considered.

The second mode was not found in the modal analysis results in Bladed. However, Jonkman et al. (2008a) has reported a mode (i.e., first drivetrain torsion mode) between the fist mode (the one dominant by tower first side-side mode) and the third mode (the one dominant by blade first flapwise modes). Hence, the second mode in Table 5.4 is suspected to be the first drivetrain torsion mode, as shown in Table 5.4.

Using the automated OMA, the SS2 values from 1 May to 15 May were extracted from the corresponding time series. They will be used as training data to obtain the GPR parameters. The SS2 for OWT 1, OWT 2 and OWT 3 are denoted as $f_1$, $f_2$ and $f_3$, respectively, as shown in the period of 1 May to 15 May in Figure 5.9. It can be seen that the changes of SS2 during the simulated tidal levels are significant. For example, during 1 May to 15 May the SS2 of OWT 1 has a minimum of 1.3698 Hz and a maximum of 1.4516 Hz. That means SS2 can change 5.97% as a result of the varying tide level. The SS2 from 16 May to 31 May and 1 June to 8 Jun will be used as new observations for testing the trained GPR models in Section 5.5.2. They are denoted as $f_1^*$, $f_2^*$ and $f_3^*$ for OWT 1, OWT 2 and OWT 3 respectively and shown as the blue lines in Figure 5.9 correspondingly. These notations for the SS2 are shown in Table 5.3.

### 5.5.2 Gaussian process regression

The SS2, $f_1$, $f_2$ and $f_3$, extracted from the training data using the automated OMA were used to train the GPR model as described in Section 5.3. It is worth noting that the GPR model is trained to represent the relationship between the features of two adjacent OWTs. In the case of the three-OWT wind farm, there were three GPR models to be learned. Echoing Equation (5.3), the three models are:

$$\begin{aligned} f_2 &= g_{12}(f_1) + \epsilon_{12} \\ f_3 &= g_{23}(f_2) + \epsilon_{23} \\ f_1 &= g_{31}(f_3) + \epsilon_{31} \end{aligned} \tag{5.21}$$

where $g_{12}$ is the relationship between $f_1$ and $f_2$, and $\epsilon_{12}$ is the corresponding Gaussian white noise. $g_{23}$, $g_{31}$, $\epsilon_{23}$ and $\epsilon_{31}$ are defined likewise. It is worth noting that the vector $\mathbf{x}$ in Equation (5.3) has reduced to a scalar ($f_1$, $f_2$ or $f_3$) in Equation (5.21) as the feature, SS2, is a scalar. The feature can also be a vector, such as the frequencies of different modes, but this is beyond the scope of this chapter and will not be studied. Each of the GPR models is determined by the hyper-parameters, which are estimated with cross-validation, as shown in Section 5.3.2.2.

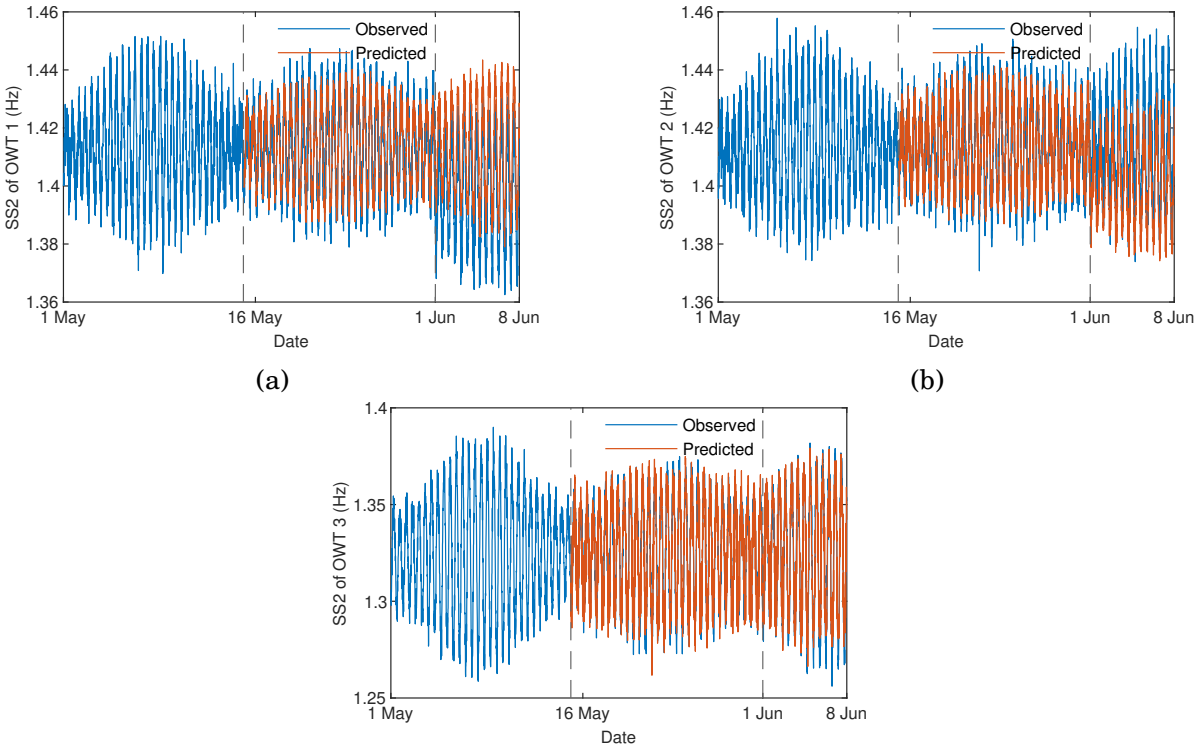


Figure 5.9: Comparisons between the observed SS2 and the predicted SS2 for (a) OWT 1, (b) OWT 2, and (c) OWT 3.

Once the GPR models are obtained, they can be used to predict the SS2 of one OWT based on the observed SS2 of the adjacent OWT. That means,

$$\begin{aligned} \hat{f}_2 &= g_{12}(f_1^*) + \epsilon_{12} \\ \hat{f}_3 &= g_{23}(f_2^*) + \epsilon_{23} \\ \hat{f}_1 &= g_{31}(f_3^*) + \epsilon_{31} \end{aligned} \tag{5.22}$$

where $\hat{f}_2$, $\hat{f}_3$ and $\hat{f}_1$ are the predicted SS2 for OWT 2, OWT 3 and OWT 1 respectively. The predicted SS2 is shown as the red lines in Figure 5.9. During the period of 16 May to 31 May, the predicted SS2 fits very well with the observed SS2, which is expected as all the OWTs are undamaged in this period. In the next period from 1 June to 7 June, the predicted SS2 deviates from the observed SS2 in Figures5.9 (a) and (b), while they are consistent in Figure 5.9 (c). The deviation will be further quantified with residuals subsequently.

The prediction residuals are calculated by subtracting the observed SS2 from the

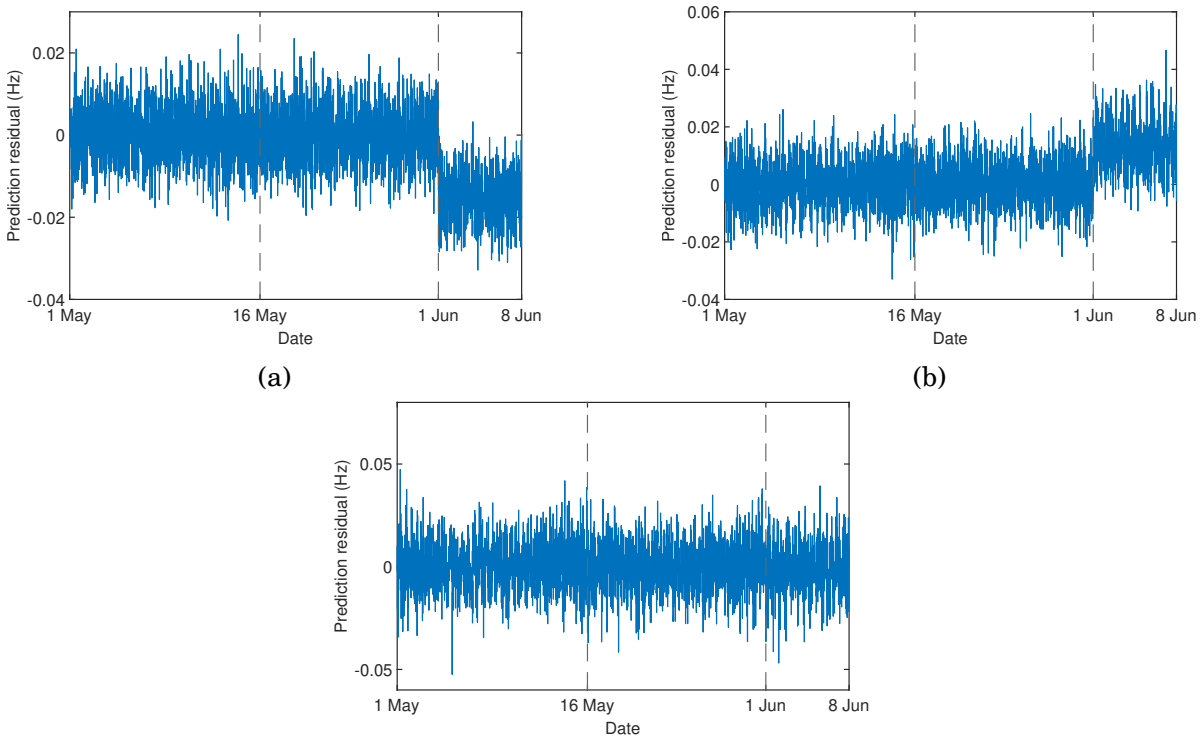


Figure 5.10: Residual errors for (a) OWT 1, (b) OWT 2, and (c) OWT 3

predicted SS2 for each OWT. That is,

$$\begin{aligned} r_2 &= \hat{f}_2 - f_2 \\ r_3 &= \hat{f}_3 - f_3 \\ r_1 &= \hat{f}_1 - f_1 \end{aligned} \tag{5.23}$$

where $r_2$, $r_3$ and $r_1$ are the predicted residuals of OWT 2, OWT 3 and OWT 1 respectively.

Figure 5.10 shows the prediction residuals corresponding to the results shown in Figure 5.9. Compared with Figure 5.9, it is clearer to see the deviation in Figure 5.10. For damage detection, the residuals are further processed with an X-bar control chart, which is presented in the next section.

### 5.5.3 X-bar control chart

Based on the obtained prediction residuals, $r_2$, $r_3$ and $r_1$, X-bar control charts were plotted. Take $r_1$ as an example; During the testing period, which is from 16 May to 7 June, there are 23 days and 2208 samples for the prediction residuals of each OWT. These samples are divided into $m = 23$ subgroups, each of size $n = 96$.

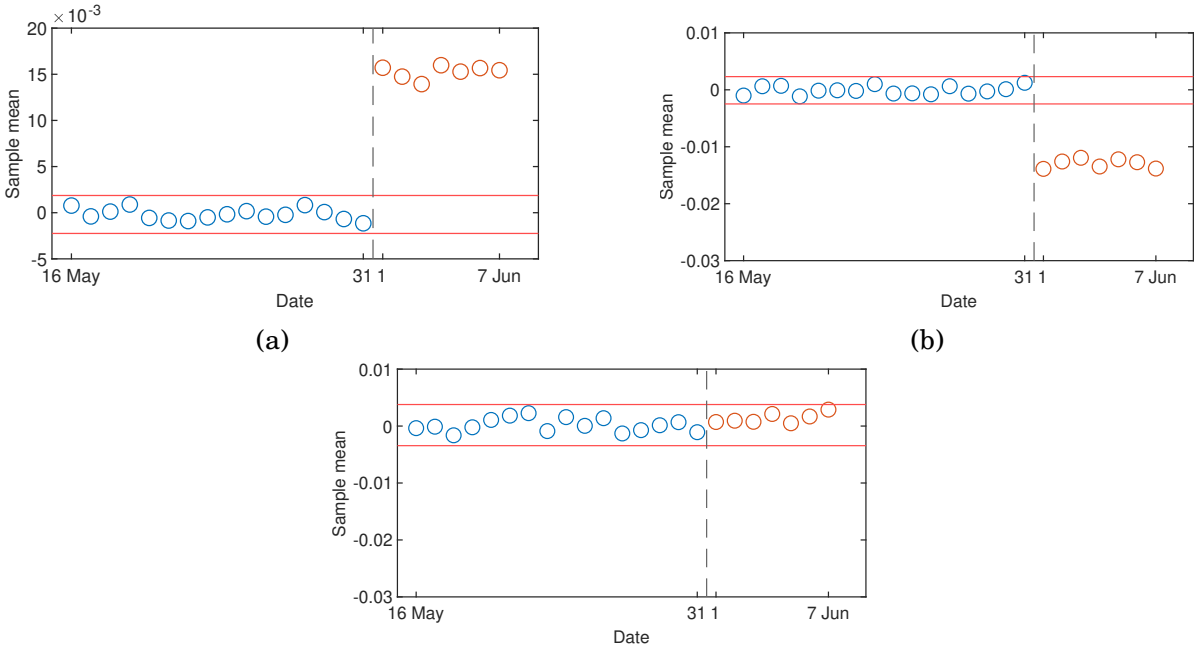


Figure 5.11: X-bar control charts of the residuals for: (a) OWT 1, (b) OWT 2 and (c) OWT 3. The horizontal lines represents the UCLs and LCLs.

The corresponding X-bar control charts for OWTs are shown in Figure 5.11. The horizontal lines indicate UCL and LCL. In Figure 5.11 (a), it can be seen that from 1 June, the residuals are out of control. That indicates the relationship between OWT 3 and OWT 1 has changed. This can be caused by either OWT 3 or OWT 1 is damaged or both OWTs are damaged. This message is expressed by marking the arrow between OWT 3 and OWT 1 Figure 5.6 in red. Similarly, in Figure 5.11 (b), the residuals for OWT 2 are out of control after 1 June, and the corresponding arrow is also marked in red. In Figure 5.11 (c), the residuals are in control. It means the relationship between OWT 2 and OWT 3 does not change, and both OWT 2 and OWT 3 are undamaged. The corresponding arrow is marked in greed. Overall, from the graph in Figure 5.6 and the arrow colours, it is obvious that OWT 1 is likely to be damaged. Therefore, the damage is detected and localised to OWT 1 successfully.

## 5.6 Conclusions

This chapter has provided a new approach to remove EOV effects in SHM problems for OWTs. This approach takes advantage of the fact that OWTs are built in groups

and thus subjected to similar EOVs at the same time. When the monitored features are viewed relative to each other, the complex EOV effects are probably cancelled out. Specifically, automated OMA was used to extract the modal frequencies of the side-side second mode of the support structure as features, and the relationships between the features of adjacent OWTs were modelled using Gaussian process regression. In the application of a three-OWT wind farm, the proposed method successfully detected the damage and localised it to a specific OWT.

In this chapter, the proposed method has been applied to one natural frequency. But the method is readily applicable for multiple natural frequencies. In addition, the three-OWT wind farm was used for demonstration, but the proposed method can be applied for a larger wind farm which consists of dozens of OWTs. In this case, one OWT may have multiple neighbours, and multiple regression models may be developed for the OWT to increase the damage detection performance.

The premise of the method is that the relationship between the natural frequencies of two adjacent OWTs is not affected by EOVs, but only affected by the damage. Although the proposed method has proved to be successful in the numerical case study, it will be valuable to verify the method on real-world data.

CHAPTER 6

# Conclusions and future work

## 6.1 Summary

Structural health monitoring (SHM) is used to automatically detect, identify, and estimate damage in civil infrastructure, allowing cost-effective management of maintenance activities. Applying SHM to offshore wind turbines (OWTs) is crucial for these structures to reduce maintenance and operational costs. Within the SHM research community, vibration-based damage detection (VBDD) has gained widespread interest for several reasons, such as its 'global' coverage, ability to be automated, and mature and reasonably low-cost signal measurement and acquisition technologies. However, it is still difficult to transfer VBDD techniques from the laboratory to the field due to various challenges. This thesis focused on these challenges and demonstrated the proposed methods on OWT foundations. The main work of this thesis is summarised below.

- Chapter 3 presented a new method based on the multivariate probability density function (PDF) of the underlying stochastic process of vibration responses. With the PDF of the undamaged state and that of a potentially damaged state, the Kullback-Leibler (KL) divergence between the two PDFs is used as the damage index. Finally, the proposed method was demonstrated on a linear OWT subjected to scour damage.

  The proposed PDF-based method showed significant damage detection performance improvements over an autocorrelation function (ACF)-based method and an autoregressive (AR)-based method. Compared with the AR-based method, the PDF-based method has better performance, especially for higher noise levels. Meanwhile, the PDF-based method is superior to the ACF-based method in almost all cases, although these two methods are closely related. The superiority of the PDF-based method may be attributed to the application of the multivariate PDF and the KL divergence. Regarding the effect of noise, both the ACF-based method and the PDF-based method are less sensitive to the noise than the AR-based method. In

conclusion, the Gaussian PDF-based method appears promising for the VBDD problem of a linear system under Gaussian white excitation and noise.

- Chapter 4 tackled the damage detection problem for an initially nonlinear system by extending the work in Chapter 3. Similar to Chapter 3, the main principle is characterising vibration responses by a multivariate PDF, and detecting the damage by monitoring the change, measured by the KL divergence, between the PDF of the undamaged state and that of a potentially damaged state. The difference is, due to the nonlinearity of the structure, the PDFs are no longer Gaussian as in Chapter 3 but non-Gaussian and unknown, making the PDF estimation rather difficult. Therefore, the density ratio estimation method, which directly estimates the difference of the PDFs rather than the individual PDFs themselves, is applied. In addition, principal component analysis was used to reduce the dimensionality of the PDFs.

  The proposed method dealt with non-Gaussian PDFs due to the nonlinearity of structures. It successfully detected the damages in two case studies: an experimental nonlinear beam and an offshore wind turbine with scour. Compared with the Gaussian-PDF-based method in Chapter 3, which only considers the second-order statistical information, the proposed method performs consistently better due to involving higher-order statistical information, which is relevant to nonlinear structures.

- Chapter 5 provided a new approach to remove environmental and operational variation (EOV) effects in SHM problems for OWTs. This approach takes advantage of the fact that OWTs are built in groups and thus subjected to similar EOVs at the same time. When the monitored features are viewed relative to each other, the complex EOV effects are probably cancelled out. Specifically, an automated operational modal analysis method was used to extract the resonance frequencies of the support structure as features, and the relationships between the features of adjacent OWTs were modelled using Gaussian process regression. In the application of a three-OWT wind farm, the proposed method successfully detected the damage and localised it to a specific OWT.

## 6.2 Limitations

The limitations of this thesis are presented below.

- The loading of OWTs was significantly simplified for demonstrating the proposed damage detection methods. Specifically, the OWTs were set as parked throughout the thesis. Also, the loading was assumed to be Gaussian white noise and applied as a point load in Chapter 3 and Chapter 4.

- In Chapter 3 and Chapter 4, the EOVs were assumed to be similar for the undamaged state and damaged states. This requires a record of the vibration responses of all possible EOVs, resulting in a heavy data storage burden. The recording can even be impossible for complex systems, such as offshore wind turbines, or extreme EOVs.

- The premise of the method in Chapter 5 is that the relationship between the resonance frequencies of two adjacent OWTs is not affected by EOVs, but only affected by the damage. Although the proposed method has been proved to be successful in the numerical case study of OWTs, its verification on real-world data is needed.

## 6.3 Future work

This thesis addressed different challenges of VBDD and demonstrated the proposed methods on OWTs. It open a variety of topics for future work.

- The proposed methods in this thesis only considered signals from one sensor, which is useful for structures with limited sensors. It is suggested to used multiple sensors in future work as it may improve damage detection performance and allow damage localisation. The methods in Chapter 3 and Chapter 4 can be easily adapted to multiple sensor versions by concatenating the Hankel matrix of each sensor into a larger Hankel matrix. The method in Chapter 5 is readily applicable for multiple sensors.

- The method in Chapter 5 only used the natural frequency of one mode of each OWT. Using multiple modes would give more information and thus improve the method performance. In addition, other features, such as the features reviewed in Chapter 2.1.1, may be explored to improve damage detection performance.

- The three-OWT wind farm in Chapter 5 was used for demonstration, but the proposed method can be applied for a larger wind farm which consists of dozens

of OWTs. In this case, one OWT may have multiple neighbours, and multiple regression models may be developed for the OWT to increase the damage detection performance.

- Following the point above, a probabilistic graphical model (Koller et al., 2009) may be used to represent the joint PDF of the features of all the OWTs in a wind farm. When applied for VBDD, the probabilistic graphical model can inherently utilise the information from other OWTs.

APPENDIX A

# Appendix A

## A.1 Autoregressive-based method

Autoregressive (AR) models assume the current value is a particular linear function of its past values. For the acceleration time series from a single sensor $\{x_i\}_{i=1}^{N}$, the AR model is given by Yao and Pakzad (2012)

$$x_i = \sum_{s=1}^{p} \alpha_s x[i-s] + v_i \tag{A.1}$$

where $\alpha_s$ is the $s$th AR coefficient, $p$ is the AR model order, and $v_i$ is the residual term at time instant $i$.

Before fitting the AR model, the $p$ should be determined. Several criteria have been introduced for this purpose, with two of the most widespread being the Akaike Information Criterion (AIC) Akaike (1974) and the Bayesian Information Criterion Schwarz and Others (1978). In this paper, AIC was used to determine $p$. The AIC consists of two terms, one of which is a log-likelihood function, and the other term penalises the number of parameters in the AR model. It is given as:

$$\mathrm{AIC} = -2\log(L) + 2q \tag{A.2}$$

where $L$ is the log-likelihood. Figure A.1 shows the AIC curve of a noise-free time series from Sensor 1 in the undamaged state. The model order is decided to be 25, where the AR model gives an AIC value that is deemed to be sufficiently small Figueiredo et al. (2011b). This model order is used for all the time series, for both the undamaged and potentially damaged states.

Once $p$ is decided, the coefficients can be estimated by the Burg method Kay (1988). The DI for the AR-based model is the Mahalanobis distance between two sets of AR coefficients, which come from the undamaged state and a potentially damaged state respectively. It is defined as

$$\mathrm{DI}_{\mathrm{AR}} = \sqrt{\left(\alpha_1 - \overline{\alpha}_0\right)^{\mathrm{T}} \mathbf{S}_0^{-1} \left(\alpha_1 - \overline{\alpha}_0\right)} \tag{A.3}$$

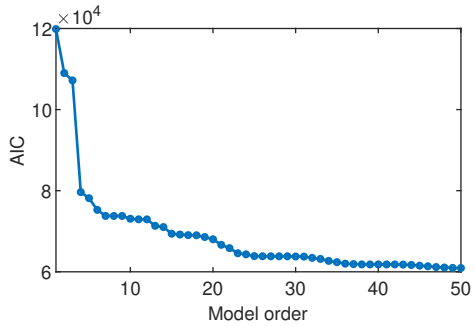


Figure A.1: Variation of AIC with model order.

where $\overline{\alpha}_0$ and $\mathbf{S}_0$ are the mean vector and covariance matrix of the first $k_{\mathrm{AR}}$ AR coefficients in the undamaged state, respectively. $\alpha_1$ is the vector of the first $k_{\mathrm{AR}}$ AR coefficients in an damaged state. $k_{\mathrm{AR}}$ is a free parameter and is tuned in a similar way to selecting $k$ in Section 3.5.1, using the same dataset. By varying $k_{\mathrm{AR}}$ from 1 to 25 with a step of 1, the optimal $k_{\mathrm{AR}}$ was selected as 13, which maximised the ROC-AUC.

## A.2 Autocorrelation function-based method

The change of the ACF of the measured time series can be used to indicate damage Zubaydi et al. (2000); Farrar and Worden (2012). The DI in the ACF-based method is defined as

$$\mathrm{DI}_{\mathrm{ACF}} = \frac{1}{n_r} \sum_{m=1}^{n_r} d(\beta_1, \beta_{0,m}) \tag{A.4}$$

where $\beta_1$ is the vector of the first $k_{\mathrm{ACF}}$ ACF coefficients of the acceleration time series in the potentially damaged state, $\beta_{0,m}$ is the vector of the first $k_{\mathrm{ACF}}$ ACF coefficients of the acceleration in the undamaged state, and $d(\beta_1, \beta_{0,m})$ is the Euclidean distance between $\beta_1$ and $\beta_{0,m}$. $k_{\mathrm{ACF}}$ is a free parameter and, again, is tuned in a similar way to selecting $k$ in Section 3.5.1 based on the same dataset. By varying $k_{\mathrm{ACF}}$ from 1 to 200 with a step of 5, the optimal $k_{\mathrm{ACF}}$ was selected as 90, which maximised the ROC-AUC.

# References


Adeli, H. and Yeh, C. (1989). Perceptron learning in engineering design. *Computer-Aided Civil and Infrastructure Engineering*, 4(4):247–256.

Aied, H., González, A., and Cantero, D. (2016). Identification of sudden stiffness changes in the acceleration response of a bridge to moving loads using ensemble empirical mode decomposition. *Mechanical Systems and Signal Processing*, 66:314–338.

Akaike, H. (1974). A new look at the statistical model identification. *IEEE transactions on automatic control*, 19(6):716–723.

American Petroleum Institute (2000). Recommended practice for planning, designing and constructing fixed offshore platforms - Working stress design. Standard, American Petroleum Institute.

Amezquita-Sanchez, J. P. and Adeli, H. (2015a). A new music-empirical wavelet transform methodology for time–frequency analysis of noisy nonlinear and non-stationary signals. *Digital Signal Processing*, 45:55–68.

Amezquita-Sanchez, J. P. and Adeli, H. (2015b). Synchrosqueezed wavelet transform-fractality model for locating, detecting, and quantifying damage in smart highrise building structures. *Smart Materials and Structures*, 24(6):65034.

Amezquita-Sanchez, J. P., Park, H. S., and Adeli, H. (2017). A novel methodology for modal parameters identification of large smart structures using MUSIC, empirical wavelet transform, and Hilbert transform. *Engineering Structures*, 147:148–159.

Anaissi, A., Khoa, N. L. D., Rakotoarivelo, T., Alamdari, M. M., and Wang, Y. (2019). Smart pothole detection system using vehicle-mounted sensors and machine learning. *Journal of Civil Structural Health Monitoring*, 9(1):91–102.

Andersen, L. V., Vahdatirad, M., Sichani, M. T., and Sørensen, J. D. (2012). Natural frequencies of wind turbines on monopile foundations in clayey soils—a probabilistic approach. *Computers and Geotechnics*, 43:1–11.

Aoyama, Y. and Yagawa, G. (2001). Component mode synthesis for large-scale structural eigenanalysis. *Computers & Structures*, 79(6):605–615.

Arany, L., Bhattacharya, S., Macdonald, J., and Hogan, S. J. (2014). Simplified critical mudline bending moment spectra of offshore wind turbine support structures. *Wind Energy*, 18(12):2171–2197.

Arany, L., Bhattacharya, S., Macdonald, J., and Hogan, S. J. (2015). Design of monopiles for offshore wind turbines in 10 steps. *Soil Dynamics and Earthquake Engineering*, 92:126–152.

Athanasiou, A., Ebrahimkhanlou, A., Zaborac, J., Hrynyk, T., and Salamone, S. (2020). A machine learning approach based on multifractal features for crack assessment of reinforced concrete shells. *Computer-Aided Civil and Infrastructure Engineering*, 35(6):565–578.

Avci, O., Abdeljaber, O., Kiranyaz, S., Hussein, M., Gabbouj, M., and Inman, D. J. (2021). A review of vibration-based damage detection in civil structures: From traditional methods to Machine Learning and Deep Learning applications. *Mechanical Systems and Signal Processing*, 147:107077.

Avendaño-Valencia, L. D., Chatzi, E. N., and Tcherniak, D. (2020). Gaussian process models for mitigation of operational variability in the structural health monitoring of wind turbines. *Mechanical Systems and Signal Processing*, 142:106686.

Avendaño-Valencia, L. D. and Fassois, S. D. (2017a). Damage/fault diagnosis in an operating wind turbine under uncertainty via a vibration response Gaussian mixture random coefficient model based framework. *Mechanical Systems and Signal Processing*, 91:326–353.

Avendaño-Valencia, L. D. and Fassois, S. D. (2017b). Gaussian mixture random coefficient model based framework for SHM in structures with time–dependent dynamics under uncertainty. *Mechanical Systems and Signal Processing*, 97:59–83.

Bandara, R. P., Chan, T. H., and Thambiratnam, D. P. (2014). Frequency response function based damage identification using principal component analysis and pattern recognition technique. *Engineering Structures*, 66:116–128.

Bao, C., Hao, H., and Li, Z.-X. (2013a). Integrated ARMA model method for damage detection of subsea pipeline system. *Engineering Structures*, 48:176–192.

Bao, C., Hao, H., and Li, Z.-X. (2013b). Multi-stage identification scheme for detecting damage in structures under ambient excitations. *Smart materials and structures*, 22(4):045006.

Bao, C., Hao, H., Li, Z.-X., and Zhu, X. (2009). Time-varying system identification using a newly improved HHT algorithm. *Computers & Structures*, 87(23-24):1611–1623.

Beck, J. L. and Au, S.-K. (2002). Bayesian updating of structural models and reliability using Markov chain Monte Carlo simulation. *Journal of engineering mechanics*, 128(4):380–391.

Beck, J. L. and Katafygiotis, L. S. (1998). Updating models and their uncertainties. I: Bayesian statistical framework. *Journal of Engineering Mechanics*, 124(4):455–461.

Beganovic, N. and Söffker, D. (2016). Structural health management utilization for lifetime prognosis and advanced control strategy deployment of wind turbines: An overview and outlook concerning actual methods, tools, and obtained results. *Renewable and Sustainable Energy Reviews*, 64:68–83.

Behmanesh, I. and Moaveni, B. (2015). Probabilistic identification of simulated damage on the Dowling Hall footbridge through Bayesian finite element model updating. *Structural Control and Health Monitoring*, 22(3):463–483.

Behmanesh, I., Moaveni, B., and Papadimitriou, C. (2017). Probabilistic damage identification of a designed 9-story building using modal data in the presence of modeling errors. *Engineering Structures*, 131:542–552.

Bishop, C. M. (2006). *Pattern recognition and machine learning*. Springer, New York, NY.

Bogoevska, S., Spiridonakos, M., Chatzi, E., Dumova-Jovanoska, E., and Höffer, R. (2017). A data-driven diagnostic framework for wind turbine structures: A holistic approach. *Sensors*, 17(4):720.

Bornn, L., Farrar, C. R., and Park, G. (2010). Damage detection in initially nonlinear systems. *International Journal of Engineering Science*, 48(10):909–920.

Bradshaw, E., Woodworth, P. L., Hibbert, A., Bradley, L. J., Pugh, D. T., Fane, C., and Bingley, R. M. (2016). A century of sea level measurements at Newlyn, Southwest England. *Marine Geodesy*, 39(2):115–140.

British Oceanographic Data Centre (2021). National Tidal and Sea Level Facility data series [Data set]. Retrieved from `https://www.bodc.ac.uk/data/hosted_data_systems/sea_level/uk_tide_gauge_network/`.

Brownjohn, J. M. W., De Stefano, A., Xu, Y.-L., Wenzel, H., and Aktan, A. E. (2011). Vibration-based monitoring of civil infrastructure: challenges and successes. *Journal of Civil Structural Health Monitoring*, 1(3-4):79–95.

Burton, T., Jenkins, N., Sharpe, D., and Bossanyi, E. (2011). *Wind energy handbook*. John Wiley & Sons.

Carden, E. P. and Brownjohn, J. M. (2008). Arma modelled time-series classification for structural health monitoring of civil infrastructure. *Mechanical Systems and Signal Processing*, 22(2):295–314.

Carswell, W., Arwade, S. R., DeGroot, D. J., and Lackner, M. A. (2015). Soil–structure reliability of offshore wind turbine monopile foundations. *Wind energy*, 18(3):483–498.

Chandrasekhar, K., Stevanovic, N., Cross, E. J., Dervilis, N., and Worden, K. (2021). Damage detection in operational wind turbine blades using a new approach based on machine learning. *Renewable Energy*, 168:1249–1264.

Chen, H. G., Yan, Y. J., Chen, W. H., Jiang, J. S., Yu, L., and Wu, Z. Y. (2007). Early damage detection in composite wingbox structures using Hilbert-Huang transform and genetic algorithm. *Structural Health Monitoring*, 6(4):281–297.

Ching, J., Muto, M., and Beck, J. L. (2006). Structural model updating and health monitoring with incomplete modal data using Gibbs sampler. *Computer-Aided Civil and Infrastructure Engineering*, 21(4):242–257.

Cornwell, P., Farrar, C. R., Doebling, S. W., and Sohn, H. (1999). Environmental variability of modal properties. *Experimental techniques*, 23(6):45–48.

Courtney, C. R. P., Neild, S. A., Wilcox, P. D., and Drinkwater, B. W. (2010). Application of the bispectrum for detection of small nonlinearities excited sinusoidally. *Journal of Sound and Vibration*, 329(20):4279–4293.

Cross, E. J., Manson, G., Worden, K., and Pierce, S. G. (2012). Features for damage detection with insensitivity to environmental and operational variations. *Proceedings of the Royal Society A: Mathematical, Physical and Engineering Sciences*, 468(2148):4098–4122.

Cross, E. J., Worden, K., and Chen, Q. (2011). Cointegration: a novel approach for the removal of environmental trends in structural health monitoring data. *Proceedings of the Royal Society A: Mathematical, Physical and Engineering Sciences*, 467(2133):2712–2732.

Dackermann, U., Li, J., and Samali, B. (2013). Identification of member connectivity and mass changes on a two-storey framed structure using frequency response functions and artificial neural networks. *Journal of Sound and Vibration*, 332(16):3636–3653.

Deng, J., Lu, Y., and Lee, V. C.-S. (2020). Concrete crack detection with handwriting script interferences using faster region-based convolutional neural network. *Computer-Aided Civil and Infrastructure Engineering*, 35(4):373–388.

Deraemaeker, A., Reynders, E., De Roeck, G., and Kullaa, J. (2008). Vibration-based structural health monitoring using output-only measurements under changing environment. *Mechanical Systems and Signal Processing*, 22(1):34–56.

Devriendt, C., Magalhães, F., Weijtjens, W., De Sitter, G., Cunha, A., and Guillaume, P. (2013). Automatic identification of the modal parameters of an offshore wind turbine using state-of-the-art operational modal analysis techniques. In *5th International Operational Modal Analysis Conference (IOMAC 2013)*.

Devriendt, C., Magalhães, F., Weijtjens, W., De Sitter, G., Cunha, Á., and Guillaume, P. (2014). Structural health monitoring of offshore wind turbines using automated operational modal analysis. *Structural Health Monitoring*, 13(6):644–659.

DNV (2020). *Bladed user manual, Bladed 4.10*.

DNV-GL (2016). Bladed Theory Manual version 4.8. *DNV GL - Energy*.

DNVGL-ST-0126 (2016). Support structures for wind turbines. Standard, DNV.

DNVGL-ST-0437 (2016). Loads and site conditions for wind turbines. Standard, DNV.

Doebling, S. W., Farrar, C. R., and Prime, M. B. (1998). A summary review of vibration-based damage identification methods. *Shock and vibration digest*, 30(2):91–105.

Doebling, S. W., Farrar, C. R., Prime, M. B., and Shevitz, D. W. (1996). Damage identification and health monitoring of structural and mechanical systems from changes in their vibration characteristics: a literature review. Report, Los Alamos National Lab., NM.

Drewry, M. A. and Georgiou, G. (2007). A review of NDT techniques for wind turbines. *Insight - Non-Destructive Testing and Condition Monitoring*, 49(3):137–141.

Du, Y., Zhou, S., Jing, X., Peng, Y., Wu, H., and Kwok, N. (2020). Damage detection techniques for wind turbine blades: A review. *Mechanical Systems and Signal Processing*, 141:106445.

Eltouny, K. A. and Liang, X. (2021). Bayesian-optimized unsupervised learning approach for structural damage detection. *Computer-Aided Civil and Infrastructure Engineering*, 1(21).

Farrar, C. R., Baker, W. E., Bell, T. M., Cone, K. M., Darling, T. W., Duffey, T. A., Eklund, A., and Migliori, A. (1994). Dynamic characterization and damage detection in the I-40 bridge over the Rio Grande. Technical report, Los Alamos National Lab., NM.

Farrar, C. R., Doebling, S. W., and Nix, D. A. (2001). Vibration-based structural damage identification. *Philosophical Transactions of the Royal Society of London. Series A: Mathematical, Physical and Engineering Sciences*, 359(1778):131–149.

Farrar, C. R., Duffey, T. A., Doebling, S. W., and Nix, D. A. (1999). A statistical pattern recognition paradigm for vibration-based structural health monitoring. *Structural Health Monitoring*, 2000:764–773.

Farrar, C. R. and Worden, K. (2012). *Structural health monitoring: a machine learning perspective*. John Wiley & Sons.

Fassois, S. D. and Sakellariou, J. S. (2007). Time-series methods for fault detection and identification in vibrating structures. *Philosophical Transactions of the Royal Society A: Mathematical, Physical and Engineering Sciences*, 365(1851):411–448.

Faulkner, P., Cutter, P., and Owens, A. (2012). Structural health monitoring systems in difficult environments - offshore wind turbines. In *6th European workshop on structural health monitoring*, pages 1–7.

Fawcett, T. (2006). An introduction to ROC analysis. *Pattern Recognition Letters*, 27(8):861–874.

Ferreira, L. (n.d.). Fixed wind foundations: An independent concept screening approach. `https://2hoffshore.com/blog/concept-screening-fixed-wind-foundations/`. Accessed: 2021-07-10.

Figueiredo, E., Figueiras, J., Park, G., Farrar, C. R., and Worden, K. (2011a). Influence of the autoregressive model order on damage detection. *Computer-Aided Civil and Infrastructure Engineering*, 26(3):225–238.

Figueiredo, E., Park, G., Farrar, C. R., Worden, K., and Figueiras, J. (2011b). Machine learning algorithms for damage detection under operational and environmental variability. *Structural Health Monitoring*, 10(6):559–572.

Figueiredo, E., Park, G., Figueiras, J., Farrar, C., and Worden, K. (2009). Structural health monitoring algorithm comparisons using standard data sets. Technical report, Los Alamos National Lab.(LANL), Los Alamos, NM.

Friswell, M. and Mottershead, J. E. (1995). *Finite element model updating in structural dynamics*. The Netherlands: Springer.

Fugate, M. L., Sohn, H., and Farrar, C. R. (2001). Vibration-based damage detection using statistical process control. *Mechanical Systems and Signal Processing*, 15(4):707–721.

Galleguillos, C., Zorrilla, A., Jimenez, A., Diaz, L., Montiano, Á., Barroso, M., Viguria, A., and Lasagni, F. (2015). Thermographic non-destructive inspection of wind turbine blades using unmanned aerial systems. *Plastics, Rubber and Composites*, 44(3):98–103.

Garolera, A. C., Madsen, S. F., Nissim, M., Myers, J. D., and Holboell, J. (2014). Lightning damage to wind turbine blades from wind farms in the us. *IEEE Transactions on Power Delivery*, 31(3):1043–1049.

Ghiasi, R., Torkzadeh, P., and Noori, M. (2016). A machine-learning approach for structural damage detection using least square support vector machine based on a new combinational kernel function. *Structural Health Monitoring*, 15(3):302–316.

Ghoshal, A., Sundaresan, M. J., Schulz, M. J., and Pai, P. F. (2000). Structural health monitoring techniques for wind turbine blades. *Journal of Wind Engineering and Industrial Aerodynamics*, 85(3):309–324.

Global Wind Energy Council (2021). GWEC Global Wind Report 2021. `https://gwec.net/global-wind-report-2021/`.

Gu, J., Gul, M., and Wu, X. (2017). Damage detection under varying temperature using artificial neural networks. *Structural Control and Health Monitoring*, 24(11):e1998.

Guillaume, P., Verboven, P., Vanlanduit, S., Van Der Auweraer, H., and Peeters, B. (2003). A poly-reference implementation of the least-squares complex frequency-domain estimator. In *Proceedings of IMAC*, volume 21, pages 183–192. A Conference & Exposition on Structural Dynamics, Society for Experimental Mechanics.

Gul, M. and Catbas, F. N. (2009). Statistical pattern recognition for structural health monitoring using time series modeling: Theory and experimental verifications. *Mechanical Systems and Signal Processing*, 23(7):2192–2204.

Gul, M. and Catbas, F. N. (2011). Structural health monitoring and damage assessment using a novel time series analysis methodology with sensor clustering. *Journal of Sound and Vibration*, 330(6):1196–1210.

Guo, J., Wang, Q., Li, Y., and Liu, P. (2020). Façade defects classification from imbalanced dataset using meta learning-based convolutional neural network. *Computer-Aided Civil and Infrastructure Engineering*, 35(12):1403–1418.

Hahn, B., Durstewitz, M., and Rohrig, K. (2007). Reliability of wind turbines. In *Wind energy*, pages 329–332. Springer.

Hakim, S., Razak, H. A., and Ravanfar, S. (2015). Fault diagnosis on beam-like structures from modal parameters using artificial neural networks. *Measurement*, 76:45–61.

Hallowell, S., Myers, A. T., and Arwade, S. R. (2016). Variability of breaking wave characteristics and impact loads on offshore wind turbines supported by monopiles. *Wind Energy*, 19(2):301–312.

Härdle, W. K., Müller, M., Sperlich, S., and Werwatz, A. (2004). *Nonparametric and semiparametric models*. Springer, New York, NY.

Hershey, J. R. and Olsen, P. A. (2007). Approximating the Kullback Leibler divergence between Gaussian mixture models. In *2007 IEEE International Conference on Acoustics, Speech and Signal Processing-ICASSP'07*, volume 4, pages IV–317. IEEE.

Hou, R. and Xia, Y. (2021). Review on the new development of vibration-based damage identification for civil engineering structures: 2010–2019. *Journal of Sound and Vibration*, 491:115741.

Hsu, T.-Y. and Loh, C.-H. (2010). Damage detection accommodating nonlinear environmental effects by nonlinear principal component analysis. *Structural Control and Health Monitoring*, 17(3):338–354.

Hu, W.-H., Thöns, S., Rohrmann, R. G., Said, S., and Rücker, W. (2015). Vibration-based structural health monitoring of a wind turbine system Part II: Environmental/operational effects on dynamic properties. *Engineering Structures*, 89:273–290.

Huang, C. S., Le, Q. T., Su, W. C., and Chen, C. H. (2020). Wavelet-based approach of time series model for modal identification of a bridge with incomplete input. *Computer-Aided Civil and Infrastructure Engineering*, 35(9):947–964.

Hui, Y., Law, S. S., and Ku, C. J. (2017). Structural damage detection based on covariance of covariance matrix with general white noise excitation. *Journal of Sound and Vibration*, 389:168–182.

IEC 61400-1 (2010). Wind turbines — Part 1: Design requirements. Standard, International Electrotechnical Commission.

IEC 61400-3 (2009). Wind turbines — Part 3: Design requirements for offshore wind turbines. Standard, International Electrotechnical Commission.

Jin, C., Jang, S., Sun, X., Li, J., and Christenson, R. (2016). Damage detection of a highway bridge under severe temperature changes using extended Kalman filter trained neural network. *Journal of Civil Structural Health Monitoring*, 6(3):545–560.

Jin, S.-S., Cho, S., and Jung, H.-J. (2015). Adaptive reference updating for vibration-based structural health monitoring under varying environmental conditions. *Computers & Structures*, 158:211–224.

Jolliffe, I. T. (2002). *Principal component analysis*. Springer, New York, 2nd edition.

Jolliffe, I. T. and Cadima, J. (2016). Principal component analysis: a review and recent developments. *Philosophical Transactions of the Royal Society A: Mathematical, Physical and Engineering Sciences*, 374(2065):20150202.

Jonkman, J., Butterfield, S., Musial, W., and Scott, G. (2009). Definition of a 5-MW reference wind turbine for offshore system development. Technical report, National Renewable Energy Lab, Golden, CO.

Jonkman, J., Butterfield, S., Passon, P., Larsen, T., Camp, T., Nichols, J., Azcona, J., and Martinez, A. (2008a). Offshore code comparison collaboration within iea wind annex XXIII: phase II results regarding monopile foundation modeling. Technical Report NREL/CP-500-42471, National Renewable Energy Lab.(NREL), Golden, CO.

Jonkman, J., Butterfield, S., Passon, P., Larsen, T., Camp, T., Nichols, J., Azcona, J., and Martinez, A. (2008b). Offshore code comparison collaboration within IEA wind annex XXIII: phase II results regarding monopile foundation modeling. *IEA European Offshore Wind Conference. Berlin, Germany, December4-6*.

Jonkman, J. M. and Buhl Jr, M. L. (2005). FAST User's Guide-Updated August 2005. Report, National Renewable Energy Laboratory (NREL), Golden, CO.

Journée, J. M. and Massie, W. (2001). *Offshore Hydromechanics*. Delft University of Technology, First edition.

Kallehave, D., Byrne, B. W., LeBlanc Thilsted, C., and Mikkelsen, K. K. (2015). Optimization of monopiles for offshore wind turbines. *Philosophical Transactions of the Royal Society A: Mathematical, Physical and Engineering Sciences*, 373(2035):20140100.

Kanamori, T., Hido, S., and Sugiyama, M. (2009). A least-squares approach to direct importance estimation. *The Journal of Machine Learning Research*, 10:1391–1445.

Katnam, K., Comer, A., Roy, D., Da Silva, L., and Young, T. (2015). Composite repair in wind turbine blades: an overview. *The Journal of Adhesion*, 91(1-2):113–139.

Kawahara, Y. and Sugiyama, M. (2012). Sequential change point detection based on direct density ratio estimation. *Statistical Analysis and Data Mining: The ASA Data Science Journal*, 5(2):114–127.

Kay, S. M. (1988). *Modern Spectral Estimation: Theory and Application*. Prentice Hall, Englewood Cliffs, NJ.

Kim, J.-T., Park, J.-H., and Lee, B.-J. (2007). Vibration-based damage monitoring in model plate-girder bridges under uncertain temperature conditions. *Engineering Structures*, 29(7):1354–1365.

Koller, D., Friedman, N., and Bach, F. (2009). *Probabilistic graphical models: principles and techniques*. MIT press.

Kromanis, R. and Kripakaran, P. (2013). Support vector regression for anomaly detection from measurement histories. *Advanced Engineering Informatics*, 27(4):486–495.

Kromanis, R. and Kripakaran, P. (2016). SHM of bridges: characterising thermal response and detecting anomaly events using a temperature-based measurement interpretation approach. *Journal of Civil Structural Health Monitoring*, 6(2):237–254.

Kudva, J., Munir, N., and Tan, P. (1992). Damage detection in smart structures using neural networks and finite-element analyses. *Smart Materials and Structures*, 1(2):108.

Kullaa, J. (2003). Damage detection of the Z24 bridge using control charts. *Mechanical Systems and Signal Processing*, 17(1):163–170.

Kullback, S. (1997). *Information theory and statistics*. Courier Corporation.

Lam, H. F., Hu, Q., and Wong, M. T. (2014). The Bayesian methodology for the detection of railway ballast damage under a concrete sleeper. *Engineering Structures*, 81:289–301.

Larsen, T. J. and Hansen, A. M. (2007). How 2 hawc2, the user's manual. *target*, 2(2).

Lee, J. and Zhao, F. (2021). Global wind report 2021. Technical report, Global Wind Energy Council (GWEC), Brussels, Belgium.

Li, D., Ho, S.-C. M., Song, G., Ren, L., and Li, H. (2015a). A review of damage detection methods for wind turbine blades. *Smart Materials and Structures*, 24(3):033001.

Li, H., Huang, Y., Ou, J., and Bao, Y. (2011a). Fractal dimension-based damage detection method for beams with a uniform cross-section. *Computer-Aided Civil and Infrastructure Engineering*, 26(3):190–206.

Li, H., Li, S., Ou, J., and Li, H. (2010). Modal identification of bridges under varying environmental conditions: temperature and wind effects. *Structural Control and Health Monitoring*, 17(5):495–512.

Li, J. and Chen, J. (2009). *Stochastic dynamics of structures*. John Wiley & Sons.

Li, J., Dackermann, U., Xu, Y.-L., and Samali, B. (2011b). Damage identification in civil engineering structures utilizing pca-compressed residual frequency response functions and neural network ensembles. *Structural Control and Health Monitoring*, 18(2):207–226.

Li, J., Law, S., and Ding, Y. (2012). Substructure damage identification based on response reconstruction in frequency domain and model updating. *Engineering Structures*, 41:270–284.

Li, X., Kurata, M., and Nakashima, M. (2015b). Evaluating damage extent of fractured beams in steel moment-resisting frames using dynamic strain responses. *Earthquake Engineering & Structural Dynamics*, 44(4):563–581.

Liang, X., Mosalam, K., and Muin, S. (2018a). Simulation-based data-driven damage detection for highway bridge systems. In *Proceedings 11th National Conference Earthquake Engineering.(NCEE)*, Los Angeles, California.

Liang, Y., Li, D., Song, G., and Feng, Q. (2018b). Frequency Co-integration-based damage detection for bridges under the influence of environmental temperature variation. *Measurement*, 125:163–175.

Liang, Y. C., Lee, H. P., Lim, S. P., Lin, W. Z., Lee, K. H., and Wu, C. G. (2002). Proper orthogonal decomposition and its applications: Part I: Theory. *Journal of Sound and Vibration*, 252(3):527–544.

Lim, H. J., Kim, M. K., Sohn, H., and Park, C. Y. (2011). Impedance based damage detection under varying temperature and loading conditions. *Ndt & E International*, 44(8):740–750.

Lin, Y.-z., Nie, Z.-h., and Ma, H.-w. (2017). Structural Damage Detection with Automatic Feature-Extraction through Deep Learning. *Computer-Aided Civil and Infrastructure Engineering*, 32(12):1025–1046.

Løken, I. B. and Kaynia, A. M. (2019). Effect of foundation type and modelling on dynamic response and fatigue of offshore wind turbines. *Wind Energy*, 22(12):1667–1683.

Long, J. and Büyüköztürk, O. (2017). Decentralised one-class kernel classification-based damage detection and localisation. *Structural Control and Health Monitoring*, 24(6):e1930.

Lu, Y. and Gao, F. (2005). A novel time-domain auto-regressive model for structural damage diagnosis. *Journal of Sound and Vibration*, 283(3-5):1031–1049.

Luczak, M. M., Telega, J., Zagato, N., and Mucchi, E. (2019). On the damage detection of a laboratory scale model of a tripod supporting structure by vibration-based methods. *Marine Structures*, 64:146–160.

Lutes, L. D. and Sarkani, S. (2004). *Random vibrations: analysis of structural and mechanical systems*. Elsevier Butterworth-Heinemann, Burlington, MA.

Ma, H., Yang, J., and Chen, L. (2017). Numerical analysis of the long-term performance of offshore wind turbines supported by monopiles. *Ocean Engineering*, 136:94–105.

Magalhaes, F., Cunha, A., and Caetano, E. (2009). Online automatic identification of the modal parameters of a long span arch bridge. *Mechanical Systems and Signal Processing*, 23(2):316–329.

Márquez, F. P. G., Tobias, A. M., Pérez, J. M. P., and Papaelias, M. (2012). Condition monitoring of wind turbines: Techniques and methods. *Renewable energy*, 46:169–178.

Mazhelis, O. (2006). One-class classifiers: a review and analysis of suitability in the context of mobile-masquerader detection. *South African Computer Journal*, 2006(36):29–48.

McFadden, P. (1991). A technique for calculating the time domain averages of the vibration of the individual planet gears and the sun gear in an epicyclic gearbox. *Journal of Sound and vibration*, 144(1):163–172.

Meruane, V. and Heylen, W. (2011). An hybrid real genetic algorithm to detect structural damage using modal properties. *Mechanical Systems and Signal Processing*, 25(5):1559–1573.

Michalis, P., Saafi, M., and Judd, M. (2013). Capacitive sensors for offshore scour monitoring. *Proceedings of the Institution of Civil Engineers-Energy*, 166(4):189–197.

Mieloszyk, M. and Ostachowicz, W. (2017). An application of structural health monitoring system based on fbg sensors to offshore wind turbine support structure model. *Marine Structures*, 51:65–86.

Mishnaevsky, L., Branner, K., Petersen, H. N., Beauson, J., McGugan, M., and Sørensen, B. F. (2017). Materials for wind turbine blades: an overview. *Materials*, 10(11):1285.

Moll, J., Arnold, P., Mälzer, M., Krozer, V., Pozdniakov, D., Salman, R., Rediske, S., Scholz, M., Friedmann, H., and Nuber, A. (2018). Radar-based structural health monitoring of wind turbine blades: The case of damage detection. *Structural Health Monitoring*, 17(4):815–822.

Montgomery, D. C. (2007). *Introduction to statistical quality control*. John Wiley & Sons.

Morison, J., Johnson, J., and Schaaf, S. (1950). The force exerted by surface waves on piles. *Journal of Petroleum Technology*, 2(05):149–154.

Moser, P. and Moaveni, B. (2011). Environmental effects on the identified natural frequencies of the Dowling Hall Footbridge. *Mechanical Systems and Signal Processing*, 25(7):2336–2357.

Movsessian, A., Cava, D. G., and Tcherniak, D. (2021). An artificial neural network methodology for damage detection: Demonstration on an operating wind turbine blade. *Mechanical Systems and Signal Processing*, 159:107766.

Mújica, L. E., Rodellar, J., Fernandez, A., and Güemes, A. (2011). Q-statistic and T2-statistic PCA-based measures for damage assessment in structures. *Structural Health Monitoring*, 10(5):539–553.

Mújica, L. E., Ruiz, M., Pozo, F., Rodellar, J., and Güemes, A. (2013). A structural damage detection indicator based on principal component analysis and statistical hypothesis testing. *Smart materials and structures*, 23(2):25014.

Murphy, K. P. (2012). *Machine learning: a probabilistic perspective*. MIT press.

Mustafa, S., Matsumoto, Y., and Yamaguchi, H. (2018). Vibration-based health monitoring of an existing truss bridge using energy-based damping evaluation. *Journal of Bridge Engineering*, 23(1):04017114.

Nair, K. K. and Kiremidjian, A. S. (2007). Time series based structural damage detection algorithm using Gaussian mixtures modeling. *Journal of dynamic systems, measurement, and control*, 129(3):285–293.

Nair, K. K., Kiremidjian, A. S., and Law, K. H. (2006). Time series-based damage detection and localization algorithm with application to the ASCE benchmark structure. *Journal of Sound and Vibration*, 291(1-2):349–368.

Nandi, T. N., Herrig, A., and Brasseur, J. G. (2017). Non-steady wind turbine response to daytime atmospheric turbulence. *Philosophical Transactions of the Royal Society A: Mathematical, Physical and Engineering Sciences*, 375(2091):20160103.

Nguyen, L. H. and Goulet, J.-A. (2019). Real-time anomaly detection with bayesian dynamic linear models. *Structural Control and Health Monitoring*, 26(9):e2404.

Ni, Y. Q., Hua, X. G., Fan, K. Q., and Ko, J. M. (2005). Correlating modal properties with temperature using long-term monitoring data and support vector machine technique. *Engineering Structures*, 27(12):1762–1773.

Ni, Y. Q., Xia, H. W., Wong, K. Y., and Ko, J. M. (2012). In-service condition assessment of bridge deck using long-term monitoring data of strain response. *Journal of Bridge Engineering*, 17(6):876–885.

Nikitas, G., Vimalan, N. J., and Bhattacharya, S. (2016). An innovative cyclic loading device to study long term performance of offshore wind turbines. *Soil Dynamics and Earthquake Engineering*, 82:154–160.

Okazaki, Y., Okazaki, S., Asamoto, S., and Chun, P.-j. (2020). Applicability of machine learning to a crack model in concrete bridges. *Computer-Aided Civil and Infrastructure Engineering*, 35(8):775–792.

Oliveira, G., Magalhães, F., Cunha, Á., and Caetano, E. (2018). Vibration-based damage detection in a wind turbine using 1 year of data. *Structural Control and Health Monitoring*, 25(11).

Omenzetter, P. and Brownjohn, J. M. W. (2006). Application of time series analysis for bridge monitoring. *Smart Materials and Structures*, 15(1):129.

Opoka, S., Soman, R., Mieloszyk, M., and Ostachowicz, W. (2016). Damage detection and localization method based on a frequency spectrum change in a scaled tripod model with strain rosettes. *Marine Structures*, 49:163–179.

Pan, X. and Yang, T. Y. (2020). Postdisaster image-based damage detection and repair cost estimation of reinforced concrete buildings using dual convolutional neural networks. *Computer-Aided Civil and Infrastructure Engineering*, 35(5):495–510.

Papadimitriou, C. and Papadioti, D.-C. (2013). Component mode synthesis techniques for finite element model updating. *Computers & structures*, 126:15–28.

Park, B., An, Y.-K., and Sohn, H. (2014). Visualization of hidden delamination and debonding in composites through noncontact laser ultrasonic scanning. *Composites science and technology*, 100:10–18.

Passon, P. (2006). Derivation and description of the soil-pile interaction models. Memorandum, University of Stuttgart, Germany.

Peeters, B. and De Roeck, G. (2001). One-year monitoring of the Z24-Bridge: environmental effects versus damage events. *Earthquake engineering & structural dynamics*, 30(2):149–171.

Peng, Z. and Chu, F. (2004). Application of the wavelet transform in machine condition monitoring and fault diagnostics: a review with bibliography. *Mechanical Systems and Signal Processing*, 18(2):199–221.

Perez-Ramirez, C. A., Amezquita-Sanchez, J. P., Adeli, H., Valtierra-Rodriguez, M., Camarena-Martinez, D., and Romero-Troncoso, R. J. (2016). New methodology for modal parameters identification of smart civil structures using ambient vibrations and synchrosqueezed wavelet transform. *Engineering Applications of Artificial Intelligence*, 48:1–12.

Pimentel, M. A. F., Clifton, D. A., Clifton, L., and Tarassenko, L. (2014). A review of novelty detection. *Signal Processing*, 99:215–249.

Polinder, H., Van der Pijl, F. F., De Vilder, G.-J., and Tavner, P. J. (2006). Comparison of direct-drive and geared generator concepts for wind turbines. *IEEE Transactions on energy conversion*, 21(3):725–733.

Poulimenos, A. and Fassois, S. (2006). Parametric time-domain methods for non-stationary random vibration modelling and analysis—a critical survey and comparison. *Mechanical Systems and Signal Processing*, 20(4):763–816.

Prendergast, L. J. and Gavin, K. (2014). A review of bridge scour monitoring techniques. *Journal of Rock Mechanics and Geotechnical Engineering*, 6(2):138–149.

Prendergast, L. J., Gavin, K., and Doherty, P. (2015). An investigation into the effect of scour on the natural frequency of an offshore wind turbine. *Ocean Engineering*, 101:1–11.

Qarib, H. and Adeli, H. (2014). Recent advances in health monitoring of civil structures. *Scientia Iranica*, 21(6):1733–1742.

Radzieński, M., Krawczuk, M., and Palacz, M. (2011). Improvement of damage detection methods based on experimental modal parameters. *Mechanical Systems and Signal Processing*, 25(6):2169–2190.

Rainieri, C. and Fabbrocino, G. (2014). Operational modal analysis of civil engineering structures. *Springer, New York*, 142:143.

Rasmussen, C. E. (2003). Gaussian processes in machine learning. In *Summer school on machine learning*, pages 63–71. Springer.

Reynders, E., Teughels, A., and De Roeck, G. (2010). Finite element model updating and structural damage identification using omax data. *Mechanical Systems and Signal Processing*, 24(5):1306–1323.

Rivola, A. and White, P. R. (1998). Bispectral analysis of the bilinear oscillator with application to the detection of fatigue cracks. *Journal of Sound and Vibration*, 216(5):889–910.

Rolfes, R., Zerbst, S., Haake, G., Reetz, J., and Lynch, J. P. (2007). Integral shm-system for offshore wind turbines using smart wireless sensors. In *Proceedings of the 6th International Workshop on Structural Health Monitoring*, volume 200, pages 11–13. Citeseer.

Ross, S. M. (2014). *Introduction to probability models*. Academic press, Oxford, UK, 11th edition.

Roveri, N. and Carcaterra, A. (2012). Damage detection in structures under traveling loads by Hilbert–Huang transform. *Mechanical Systems and Signal Processing*, 28:128–144.

Ruiz, M., Mújica, L., Berjaga, X., and Rodellar, J. (2013). Partial least square/projection to latent structures (PLS) regression to estimate impact localization in structures. *Smart materials and structures*, 22(2):025028.

Rytter, A. (1993). *Vibrational based inspection of civil engineering structures*. PhD thesis, Dept. of Building Technology and Structural Engineering, Aalborg University.

Saari, J., Strömbergsson, D., Lundberg, J., and Thomson, A. (2019). Detection and identification of windmill bearing faults using a one-class support vector machine (SVM). *Measurement*, 137:287–301.

Sajedi, S. O. and Liang, X. (2020). Vibration-based semantic damage segmentation for large-scale structural health monitoring. *Computer-Aided Civil and Infrastructure Engineering*, 35(6):579–596.

Salameh, J. P., Cauet, S., Etien, E., Sakout, A., and Rambault, L. (2018). Gearbox condition monitoring in wind turbines: A review. *Mechanical Systems and Signal Processing*, 111:251–264.

Samuel, P. D. and Pines, D. J. (2005). A review of vibration-based techniques for helicopter transmission diagnostics. *Journal of sound and vibration*, 282(1-2):475–508.

Samusev, M., Ulriksen, M. D., and Damkilde, L. (2019). A numerical study of vibration-based scour detection in offshore monopile foundations. In *The Seventh International*

*Conference on Structural Engineering, Mechanics and Computation*, pages 1976–1981. CRC Press.

Schölkopf, B., Williamson, R. C., Smola, A., Shawe-Taylor, J., and Platt, J. (1999). Support vector method for novelty detection. *Advances in Neural Information Processing Systems*, 12:582–588.

Schröder, K., Gebhardt, C. G., and Rolfes, R. (2018). A two-step approach to damage localization at supporting structures of offshore wind turbines. *Structural Health Monitoring*, 17(5):1313–1330.

Schwarz, G. and Others (1978). Estimating the dimension of a model. *The annals of statistics*, 6(2):461–464.

Shiki, S. B. (2016). *Application of Volterra series in nonlinear mechanical system identification and in structural health monitoring problems*. PhD thesis, Universidade Estadual Paulista.

Shiki, S. B., da Silva, S., and Todd, M. D. (2017). On the application of discrete-time Volterra series for the damage detection problem in initially nonlinear systems. *Structural Health Monitoring*, 16(1):62–78.

Sinha, J. K. (2007). Higher order spectra for crack and misalignment identification in the shaft of a rotating machine. *Structural Health Monitoring*, 6(4):325–334.

Skrimpas, G. A., Kleani, K., Mijatovic, N., Sweeney, C. W., Jensen, B. B., and Holboell, J. (2016). Detection of icing on wind turbine blades by means of vibration and power curve analysis. *Wind Energy*, 19(10):1819–1832.

Slonski, M. and Słoński, M. (2017). Gaussian mixture model for time series-based structural damage detection. *Computer Assisted Methods in Engineering and Science*, 19(4):331–338.

Sohn, H. (2007). Effects of environmental and operational variability on structural health monitoring. *Philosophical Transactions of the Royal Society A: Mathematical, Physical and Engineering Sciences*, 365(1851):539–560.

Sohn, H., Dzwonczyk, M., Straser, E. G., Kiremidjian, A. S., Law, K. H., and Meng, T. (1999). An experimental study of temperature effect on modal parameters of the Alamosa Canyon Bridge. *Earthquake engineering & structural dynamics*, 28(8):879–897.

Sohn, H. and Farrar, C. R. (2001). Damage diagnosis using time series analysis of vibration signals. *Smart materials and structures*, 10(3):446.

Sohn, H. and Law, K. H. (1997). A Bayesian probabilistic approach for structure damage detection. *Earthquake engineering & structural dynamics*, 26(12):1259–1281.

Sohn, H., Worden, K., and Farrar, C. R. (2002). Statistical damage classification under changing environmental and operational conditions. *Journal of intelligent material systems and structures*, 13(9):561–574.

Soman, R., Mieloszyk, M., and Ostachowicz, W. (2018). A two-step damage assessment method based on frequency spectrum change in a scaled wind turbine tripod with strain rosettes. *Marine Structures*, 61:419–433.

Soo Lon Wah, W., Chen, Y.-T., Roberts, G. W., and Elamin, A. (2018). Separating damage from environmental effects affecting civil structures for near real-time damage detection. *Structural Health Monitoring*, 17(4):850–868.

Spanos, N. A., Sakellariou, J. S., and Fassois, S. D. (2020). Vibration-response-only statistical time series structural health monitoring methods: a comprehensive assessment via a scale jacket structure. *Structural Health Monitoring*, 19(3):736–750.

Spiridonakos, M. and Fassois, S. (2014). Non-stationary random vibration modelling and analysis via functional series time-dependent ARMA (FS-TARMA) models–A critical survey. *Mechanical Systems and Signal Processing*, 47(1-2):175–224.

Stetco, A., Dinmohammadi, F., Zhao, X., Robu, V., Flynn, D., Barnes, M., Keane, J., and Nenadic, G. (2019). Machine learning methods for wind turbine condition monitoring: A review. *Renewable energy*, 133:620–635.

Stokkeland, M., Klausen, K., and Johansen, T. A. (2015). Autonomous visual navigation of unmanned aerial vehicle for wind turbine inspection. In *2015 International Conference on Unmanned Aircraft Systems (ICUAS)*, pages 998–1007. IEEE.

Straub, D. (2004). *Generic approaches to risk based inspection planning for steel structures*, volume 284. vdf Hochschulverlag AG at ETH Zurich.

Structural Health Monitoring Lab - São Paulo State University/Ilha Solteira (2021). UNESP-MAGNOLIA [Data set]. Retrieved from `https://github.com/shm-unesp`.

Sugiyama, M., Suzuki, T., and Kanamori, T. (2012). Density Ratio Estimation in Machine Learning. *Cambridge University Press*.

Sugiyama, M., Suzuki, T., Nakajima, S., Kashima, H., von Bünau, P., and Kawanabe, M. (2008). Direct importance estimation for covariate shift adaptation. *Annals of the Institute of Statistical Mathematics*, 60(4):699–746.

Summers, A., Wang, Q., Brady, N., and Holden, R. (2016). Investigating the measurement of offshore wind turbine blades using coherent laser radar. *Robotics and Computer-Integrated Manufacturing*, 41:43–52.

Taha, M. M. R., Noureldin, A., Lucero, J. L., and Baca, T. J. (2006). Wavelet transform for structural health monitoring: a compendium of uses and features. *Structural Health Monitoring*, 5(3):267–295.

Tahara, L. Z. (2019). A study of the influence of nonlinear behavior on experimental modal analysis. Master's thesis, Universidade Estadual Paulista.

Talbot, J., Wang, Q., Brady, N., and Holden, R. (2016). Offshore wind turbine blades measurement using coherent laser radar. *Measurement*, 79:53–65.

Tang, D. and Zhao, M. (2021). Real-time monitoring system for scour around monopile foundation of offshore wind turbine. *Journal of Civil Structural Health Monitoring*, 11(3):645–660.

Tang, J., Soua, S., Mares, C., and Gan, T.-H. (2016). An experimental study of acoustic emission methodology for in service condition monitoring of wind turbine blades. *Renewable Energy*, 99:170–179.

Tax, D. M. and Duin, R. P. (2004). Support vector data description. *Machine learning*, 54(1):45–66.

Tax, D. M. J. (2001). *One-class classification: Concept learning in the absence of counter-examples*. PhD thesis, Delft University of Technology.

Teimouri, H., Milani, A. S., Loeppky, J., and Seethaler, R. (2017). A Gaussian process–based approach to cope with uncertainty in structural health monitoring. *Structural Health Monitoring*, 16(2):174–184.

Teughels, A. and De Roeck, G. (2004). Structural damage identification of the highway bridge z24 by fe model updating. *Journal of Sound and Vibration*, 278(3):589–610.

Tibaduiza, D. A., Mújica, L. E., Rodellar, J., and Güemes, A. (2016). Structural damage detection using principal component analysis and damage indices. *Journal of Intelligent Material Systems and Structures*, 27(2):233–248.

Ulriksen, M. D., Tcherniak, D., Kirkegaard, P. H., and Damkilde, L. (2016). Operational modal analysis and wavelet transformation for damage identification in wind turbine blades. *Structural Health Monitoring*, 15(4):381–388.

van der Vaart, A. W. and van der Vaart, A. W. (1998). *Asymptotic Statistics*. Cambridge Series in Statistical and Probabilistic Mathematics. Cambridge University Press.

Verboven, P., Parloo, E., Guillaume, P., and Van Overmeire, M. (2002). Autonomous structural health monitoringï¿½part I: modal parameter estimation and tracking. *Mechanical Systems and Signal Processing*, 16(4):637–657.

Vieira, M., Viana, M., Henriques, E., and Reis, L. (2020). Soil Interaction and Grout Behavior for the NREL Reference Monopile Offshore Wind Turbine. *Journal of Marine Science and Engineering*, 8(4):298.

Villani, L. G. G., da Silva, S., Cunha, A., and Todd, M. D. (2020). On the detection of a nonlinear damage in an uncertain nonlinear beam using stochastic Volterra series. *Structural Health Monitoring*, 19(4):1137–1150.

Villani, L. G. G., da Silva, S., and Cunha Jr, A. (2019a). Damage detection in uncertain nonlinear systems based on stochastic Volterra series. *Mechanical Systems and Signal Processing*, 125:288–310.

Villani, L. G. G., da Silva, S., Cunha Jr, A., and Todd, M. D. (2019b). Damage detection in an uncertain nonlinear beam based on stochastic Volterra series: an experimental application. *Mechanical Systems and Signal Processing*, 128:463–478.

Wang, T., Han, Q., Chu, F., and Feng, Z. (2019). Vibration based condition monitoring and fault diagnosis of wind turbine planetary gearbox: A review. *Mechanical Systems and Signal Processing*, 126:662–685.

Wang, Y., Liang, M., and Xiang, J. (2014). Damage detection method for wind turbine blades based on dynamics analysis and mode shape difference curvature information. *Mechanical Systems and Signal Processing*, 48(1-2):351–367.

Wasserman, L. (2013). *All of statistics: a concise course in statistical inference*. Springer Science & Business Media.

Wei, K., Arwade, S. R., Myers, A. T., Valamanesh, V., and Pang, W. (2017). Effect of wind and wave directionality on the structural performance of non-operational offshore wind turbines supported by jackets during hurricanes. *Wind Energy*, 20(2):289–303.

Wei, X.-K., Huang, G.-B., and Li, Y.-H. (2007). Mahalanobis ellipsoidal learning machine for one class classification. In *2007 International Conference on Machine Learning and Cybernetics*, volume 6, pages 3528–3533. IEEE.

Weijtjens, W., Stang, A., Devriendt, C., and Schaumann, P. (2021). Bolted ring flanges in offshore-wind support structures-in-situ validation of load-transfer behaviour. *Journal of Constructional Steel Research*, 176:106361.

Weijtjens, W., Verbelen, T., De Sitter, G., and Devriendt, C. (2016). Foundation structural health monitoring of an offshore wind turbines: a full-scale case study. *Structural Health Monitoring*, 15(4):389–402.

White, P. (2009). Higher Order Statistical Signal Processing. *Encyclopedia of Structural Health Monitoring*.

Williams, W. and Zalubas, E. (2000). Helicopter transmission fault detection via time-frequency, scale and spectral methods. *Mechanical Systems and Signal Processing*, 14(4):545–559.

Wondra, B., Malek, S., Botz, M., Glaser, S. D., and Grosse, C. U. (2019). Wireless high-resolution acceleration measurements for structural health monitoring of wind turbine towers. *Data-Enabled Discovery and Applications*, 3(1):4.

Worden, K., Farrar, C. R., Haywood, J., and Todd, M. (2008). A review of nonlinear dynamics applications to structural health monitoring. *Structural Control and Health Monitoring*, 15(4):540–567.

Worden, K., Manson, G., and Allman, D. (2003). Experimental validation of a structural health monitoring methodology: Part I. Novelty detection on a laboratory structure. *Journal of Sound Vibration*, 259(2):323–343.

Worden, K., Manson, G., and Fieller, N. R. J. (2000). Damage detection using outlier analysis. *Journal of Sound and Vibration*, 229(3):647–667.

Wu, W.-H., Chen, C.-C., Jhou, J.-W., and Lai, G. (2018). A rapidly convergent empirical mode decomposition method for analyzing the environmental temperature effects on stay cable force. *Computer-Aided Civil and Infrastructure Engineering*, 33(8):672–690.

Wu, X., Ghaboussi, J., and Garrett Jr, J. (1992). Use of neural networks in detection of structural damage. *Computers & structures*, 42(4):649–659.

Wu, X., Hu, Y., Li, Y., Yang, J., Duan, L., Wang, T., Adcock, T., Jiang, Z., Gao, Z., Lin, Z., and Others (2019). Foundations of offshore wind turbines: A review. *Renewable and Sustainable Energy Reviews*, 104:379–393.

Xia, Q., Cheng, Y., Zhang, J., and Zhu, F. (2017). In-service condition assessment of a long-span suspension bridge using temperature-induced strain data. *Journal of Bridge Engineering*, 22(3):4016124.

Xia, Y., Xu, Y.-L., Wei, Z.-L., Zhu, H.-P., and Zhou, X.-Q. (2011). Variation of structural vibration characteristics versus non-uniform temperature distribution. *Engineering Structures*, 33(1):146–153.

Xu, B., Song, G., and Masri, S. F. (2012). Damage detection for a frame structure model using vibration displacement measurement. *Structural Health Monitoring*, 11(3):281–292.

Xu, X., Ren, Y., Huang, Q., Zhao, D.-Y., Tong, Z.-J., and Chang, W.-J. (2020). Thermal response separation for bridge long-term monitoring systems using multi-resolution wavelet-based methodologies. *Journal of Civil Structural Health Monitoring*, 10(3):527–541.

Yan, A.-M., Kerschen, G., De Boe, P., and Golinval, J.-C. (2005a). Structural damage diagnosis under varying environmental conditions - part I: a linear analysis. *Mechanical Systems and Signal Processing*, 19(4):847–864.

Yan, A.-M., Kerschen, G., De Boe, P., and Golinval, J.-C. (2005b). Structural damage diagnosis under varying environmental conditions - part II: local PCA for non-linear cases. *Mechanical Systems and Signal Processing*, 19(4):865–880.

Yan, Y. J., Cheng, L., Wu, Z. Y., and Yam, L. H. (2007). Development in vibration-based structural damage detection technique. *Mechanical Systems and Signal Processing*, 21(5):2198–2211.

Yang, B. and Sun, D. (2013). Testing, inspecting and monitoring technologies for wind turbine blades: A survey. *Renewable and Sustainable Energy Reviews*, 22:515–526.

Yang, R., He, Y., and Zhang, H. (2016). Progress and trends in nondestructive testing and evaluation for wind turbine composite blade. *Renewable and Sustainable Energy Reviews*, 60:1225–1250.

Yang, Y. and Nagarajaiah, S. (2014). Blind identification of damage in time-varying systems using independent component analysis with wavelet transform. *Mechanical Systems and Signal Processing*, 47(1-2):3–20.

Yang, Z., Yu, Z., and Sun, H. (2007). On the cross correlation function amplitude vector and its application to structural damage detection. *Mechanical Systems and Signal Processing*, 21(7):2918–2932.

Yao, R. and Pakzad, S. N. (2012). Autoregressive statistical pattern recognition algorithms for damage detection in civil structures. *Mechanical Systems and Signal Processing*, 31:355–368.

Ye, X., Wu, Y., Zhang, L., Mei, L., and Zhou, Y. (2020). Ambient effect filtering using NLPCA-SVR in high-rise buildings. *Sensors*, 20(4):1143.

Yoon, M. K., Heider, D., Gillespie, J. W., Ratcliffe, C. P., and Crane, R. M. (2010). Local damage detection with the global fitting method using operating deflection shape data. *Journal of Nondestructive Evaluation*, 29(1):25–37.

Yu, J. (2011). Bearing performance degradation assessment using locality preserving projections and gaussian mixture models. *Mechanical Systems and Signal Processing*, 25(7):2573–2588.

Yu, J.-x., Xia, Y., Lin, W., and Zhou, X.-q. (2016). Element-by-element model updating of large-scale structures based on component mode synthesis method. *Journal of Sound and Vibration*, 362:72–84.

Yu, Y., Wang, C., Gu, X., and Li, J. (2019). A novel deep learning-based method for damage identification of smart building structures. *Structural Health Monitoring*, 18(1):143–163.

Yuen, K.-V. and Lam, H.-F. (2006). On the complexity of artificial neural networks for smart structures monitoring. *Engineering Structures*, 28(7):977–984.

Zeng, M., Yang, Y., Luo, S., and Cheng, J. (2016). One-class classification based on the convex hull for bearing fault detection. *Mechanical Systems and Signal Processing*, 81:274–293.

Zhang, H., Gül, M., and Kostić, B. (2019). Eliminating temperature effects in damage detection for civil infrastructure using time series analysis and autoassociative neural networks. *Journal of Aerospace Engineering*, 32(2):4019001.

Zhang, Y., Lie, S. T., and Xiang, Z. (2013). Damage detection method based on operating deflection shape curvature extracted from dynamic response of a passing vehicle. *Mechanical Systems and Signal Processing*, 35(1-2):238–254.

Zhang, Y., Macdonald, J., Harper, P., and Liu, S. (2020). VIBRATION-BASED DAMAGE LOCALIZATION WITH DENSITY RATIO ESTIMATION METHOD. In *XI International Conference on Structural Dynamics, EURODYN 2020, 23-26 November 2020,*, volume I, pages 823–832, Athens, Greece.

Zhao, H.-W., Ding, Y.-L., Nagarajaiah, S., and Li, A.-Q. (2019). Behavior analysis and early warning of girder deflections of a steel-truss arch railway bridge under the effects of temperature and trains: case study. *Journal of Bridge Engineering*, 24(1):5018013.

Zhao, Y., Yang, J., and He, Y. (2012). Concept design of a multi-column tlp for a 5mw offshore wind turbine. In *International Conference on Offshore Mechanics and Arctic Engineering*, volume 44946, pages 225–232. American Society of Mechanical Engineers.

Zhou, H. F., Ni, Y. Q., and Ko, J. M. (2010). Constructing input to neural networks for modeling temperature-caused modal variability: mean temperatures, effective temperatures, and principal components of temperatures. *Engineering Structures*, 32(6):1747–1759.

Zhou, H. F., Ni, Y. Q., and Ko, J. M. (2011). Eliminating temperature effect in vibration-based structural damage detection. *Journal of Engineering Mechanics*, 137(12):785–796.

Zhu, Y., Ni, Y.-Q., Jesus, A., Liu, J., and Laory, I. (2018). Thermal strain extraction methodologies for bridge structural condition assessment. *Smart Materials and Structures*, 27(10):105051.

Zimroz, R. and Bartelmus, W. (2009). Gearbox condition estimation using cyclo-stationary properties of vibration signal. In *Key Engineering Materials*, volume 413, pages 471–478.

Zubaydi, A., Haddara, M. R., and Swamidas, A. S. J. (2000). On the use of the autocorrelation function to identify the damage in the side shell of a ship's hull. *Marine Structures*, 13(6):537–551.